Explanation of AEROSTABIL Limit-Cycle Oscillations via High-Fidelity Aeroelastic Simulations

Bei der Fakultät für Maschinenbau
der Technischen Universität Carolo-Wilhelmina zu Braunschweig

zur Erlangung der Würde

eines Doktor-Ingenieurs (Dr.-Ing.)

genehmigte Dissertation

von: Bernd Stickan
aus: Lübbecke

eingrereicht am: 01.06.2017
mündliche Prfung am: 06.02.2018

Gutachter:
Prof. Dr.-Ing. Lorenz Tichy (TU Braunschweig)
Prof. Dr.-Ing. Rolf Radespiel (TU Braunschweig)

2018

Abstract

This thesis deals with the physical understanding of the limit-cycle oscillations (LCO) of the AEROSTABIL wing model by means of computational simulations. The LCOs have been measured by Dietz et al. (2003) in the Transonic Windtunnel Göttingen in 2002/2003. Aeroelastic high-fidelity CFD-CSM methods have been developed and applied to simulate these transonic, clean wing LCOs.

The aeroelastic methods include a versatile CFD-CSM coupling method, CFD mesh deformation with radial basis functions, steady and unsteady fluid-structure interaction as well as unsteady forced motion methods for frequency domain analysis.

To find a convincing AEROSTABIL LCO statement the available experimental pressure and acceleration data have been used to validate the computations. Static aeroelastic investigations are the starting point: Here the AEROSTABIL model revealed strong profile cambering. Only a detailed structural model allowed the accurate prediction of these deformations and the measured static pressures. An additional experiment including the AEROSTABIL wing verified the profile deformations. The accuracy of the resulting static pressures is very important to allow the simulation of the unsteady LCO phenomena. Furthermore, the profile cambering must be incorporated into the unsteady investigations as well.

Flow features at LCO conditions are very challenging for the applied aerodynamic method. The double-shock system plus flow separation could only be predicted with sufficient accuracy by certain turbulence models.

The aerodynamically driven LCO could be explained by strong shock movement in the outer wing area. It is revealed that this effect leads to a nonlinearly reducing wing excitation with increasing motion amplitude.

Overall, an important scientific contribution of the studies is to show the potential accuracy of state of the art aeroelastic methods.

Zusammenfassung

Im Rahmen dieser Dissertation werden die Grenzzyklus-Oszillationen (Limit-Cycle Oscillation=LCO) des AEROSTABIL Flügel mittels Computersimulationen erklärt. Die LCOs wurden in den Jahren 2002/2003 im Transsonischen Windkanal Göttingen gemessen. Für die Erklärung des Phänomens wurden hochgenaue Simulationsmethoden für die Interaktion von numerischer Strömungs- und Strukturmechanik entwickelt und angewendet.

Zu den aeroelastischen Methoden gehört eine vielseitige Kopplungsmethode, eine Methode zur Deformation der aerodynamischen Rechennetze mittels radialer Basisfunktionen, Methoden zur stationären und instationären Interaktion von Aerodynamik- und Strukturlöser sowie Methoden zur Berechnung der aerodynamischen Antwort von erzwungenen Schwingungen für Frequenzbereichsanalysen.

Um zu einer überzeugenden Erklärung der LCOs zu gelangen werden die verfügbaren Druck- und Beschleunigungsdaten genutzt um die Rechnungen zu validieren. Anfangspunkt sind die stationären Analysen: Hierbei zeigt der AEROSTABIL-Flügel starke Profildeformationen. Diese Verformungen und die zugehörigen Drücke können nur mit einem detaillierten Strukturmodell vorhergesagt werden. Ein weiteres Experiment mit dem gleichen Flügel bestätigt die Profilverformungen. Die Genauigkeit der resultierenden Drücke ist entscheidend für die Simulation der Grenzzyklus-Schwingungen. Außerdem sind die Profildeformationen auch für die instationären Analysen sehr wichtig.

Die Strömungseigenschaften bei LCO Bedingungen sind sehr herausfordernd für das aerodynamische Modell. Das Doppelstoß-System mit starker Strömungsablösung kann nur von bestimmten Turbulenzmodellen mit hinreichender Genauigkeit vorhergesagt werden.

Der aerodynamisch getriebene LCO wird erklärt durch starke Stoßbewegung am Außenflügel. Es wird gezeigt, dass dieser Effekt mit wachsender Amplitude zur Verringerung der Anregung des

Flügels führt.

Insgesamt liefern die Studien einen wissenschaftlichen Beitrag indem sie die erreichbare Genauigkeit von 'state-of-the-art' aeroelastischen Methoden zeigen.

Acknowledgements

The foundation of this research subject has been built during my time as 'Patenschafts' research associate at the DLR institute of aeroelasticity. This 'Patenschaft' with the department of aeroelasticity at Airbus Bremen brought me a relatively free and unbound research period, either at the DLR or at Airbus. Accordingly, my first thanks go to Professor Tichy to give me the freedom to work on this topic much longer than planned in the first place, even after leaving the DLR. Otherwise my relatively short time at the DLR would not have allowed to bring the topic to the here documented point.

From my colleagues at the DLR my biggest thanks goes to Johannes Dillinger. The generation of the AEROSTABIL FEM has led to the biggest breakthrough in accurately simulating the experiments. I think, starting at the DLR with a mainly aerodynamic background, at this early point in my aeroelastic life I would not have started such a complex task on my own. Also special thanks goes to Reik Thormann for introducing me into software like TAU and Solar, but also for fruitful discussions about unsteady aerodynamics and CFD in general. Further thanks goes to my research group leader Ralph Voss and his successor Jens Nitzsche. They motived me to push the AEROSTABIL topic to this status. Nevertheless, I am grateful for the help by many other DLR colleagues, listing here some which come to my mind: Günther Schewe, Yves Govers, Holger Mai and Jens Neumann. To all others which I might have forgotten at least special thanks for the great time at the DLR with its TSO-Room meetings and many other events.

At Airbus my largest gratitude goes to Bernd Schulze for many technical discussions in the past 7 years and also for the most detailed correction of this document. But also my former group leader Hans Bleecke inspired me with his non-compliant way of working.

Further thanks for corrections goes to Patrick Schneider, Frank Schröder, Sebastian Helm and Michael Wrightson.

Last but not least I would like to give special thanks to my family and friends. They might not have accelerated finishing this thesis, but gave me the base for my work, but also the regular relief from it. The largest thanks goes to my wife Ulrike to respect my extravagant aeroelastic hobby and my sons Fiete and Jakob, whose expected arrivals lead to writing motivation bursts.

Bernd Stickan

Contents

List of Figures

List of Tables

Nomenclature

Abbreviations

FEM	Finite element method
CFD	Computational fluid dynamics
CSM	Computational structural dynamics
DLM	Doublet lattice method
DNW-TWG	German-Dutch windtunnels: Transonic windtunnel Göttingen
DOF	Degree of freedom
exp	Experiment
GAF	Generalized air force
GVT	Ground vibration test
LCO	Limit-cycle oscillations
LFD	Linear frequency domain (solver)
MAC	Modal assurance criterion
RBF	Radial basis function
RFW	Radius full weight, RBF interpolation
RSM	Reynolds stress turbulence model
RZW	Radius zero weight, RBF interpolation
SAE	Spalart-Allmaras turbulence model with Edward's Modification
SAO	Spalart-Allmaras turbulence model, original formulation

sim	Simulation
SST	Menter SST turbulence model

Greek Symbols

α	Angle of attack
α_i	RBF coefficient
$\boldsymbol{\alpha}$	RBF coefficient vector
$\beta_{Newmark}$	Newmark algorithm parameter
$\boldsymbol{\Delta} x$	CFD mesh deformation input displacements
$\Delta\widetilde{\boldsymbol{x}_i}$	Interpolated displacements of base point $\boldsymbol{x}_i$
$\Delta\widetilde{X}$	Set of interpolated displacements
$\delta_{Newmark}$	Newmark algorithm parameter
ϵ	Small value
λ	Thermal conductivity
μ	Dynamic viscosity
μ_d	Coefficient of pressure viscosity
μ_t	Turbulent eddy viscosity
ω_i	Structural eigenvalue
ϕ	Radial basis function
ϕ_a	Structural eigenmode defined on aerodynamic surface
Φ_s	Structural eigenmode matrix
ϕ_s	Structural eigenmode
ρ	Local fluid density
τ_{ij}	Entry i, j of local fluid stress tensor
τ_{tur}	Turbulent stress tensor

Θ Rotational degree of freedom, 1 DOF example

Latin Symbols

$\boldsymbol{A}$ RBF coefficient matrix (matrix to compute coefficients)

$\widehat{\mathbf{A}}$ Unsteady aerodynamic matrix

a_1,a_2 Parameter of simple aerodynamic model, 1 DOF example

$\boldsymbol{b}$ RBF interpolation displacement input

C Sutherland constant

c Chord length

$\widehat{C_{\text{lift}}}$ Unsteady lift transfer function, first harmonic

$\widehat{cp}$ Unsteady pressure transfer function, first harmonic

C_{lift} Lift coefficient

c_p Specific heat capacity (isobaric)

c_{ref} Reference length

cf_x Skin friction in x direction (flow direction)

cp Pressure coefficient

D Damping ratio of aeroelastic system

$\boldsymbol{d}x_v$ CFD mesh volume displacements

$\boldsymbol{D^*}$ Structural damping matrix in physical coordinates

$\boldsymbol{dx_a}$ Aerodynamic surface displacements, translational

$\boldsymbol{dx_s}$ Structural displacements in physical coordinates, translational and rotational

$\boldsymbol{D}$ Structural damping matrix in generalized coordinates

δ Real part of complex flutter parameter p

d_i Distance to surface of point i

$d_{i,j}$ Distance of points i and j

d_i Modal structural damping value

D_s Structural damping 1 DOF example

dz_{Camber} Camber value, measure for airfoil deformation

$\boldsymbol{e}$ Interpolation error of input base points

ϵ_{FP} Free-play parameter, 1 DOF example

f Frequency

$\boldsymbol{f_a}$ Aerodynamic surface forces

$\boldsymbol{f_s}$ Forces acting on structure

f, s General functions

f_i Local fluid force

f_i Structural eigenfrequency

F_a Aerodynamic force 1 DOF example

h Local enthalpy

$\mathbf{H_{a,s}}$ Interpolation matrix from structural to aerodynamic surface

h_g Local total enthalpy

$\boldsymbol{K^*}$ Structural stiffness matrix in physical coordinates

$\boldsymbol{K}$ Structural stiffness matrix in generalized coordinates

$\overline{k}$ Turbulent energy

K_s Structural stiffness 1 DOF example

$\boldsymbol{M^*}$ Structural mass matrix in physical coordinates

$\boldsymbol{M}$ Structural mass matrix in generalized coordinates

$\mathbf{M}_{Blend\_i,j}$ Blending matrix of coupling group i and domain level j

$\mathbf{M}_{Blend\_i}$ Blending matrix of coupling group i

$\mathbf{M}_{Blend}$ Blending matrix contained in $\mathbf{H}_{\mathbf{a},\mathbf{s}}$

$\mathbf{M}_{Relax}$ Relaxation matrix contained in $\mathbf{H}_{\mathbf{a},\mathbf{s}}$

$\mathbf{M}_{Sp\_i}$ Spline matrix of coupling domain i

$\mathbf{M}_{Splines}$ Splines matrix contained in $\mathbf{H}_{\mathbf{a},\mathbf{s}}$

M_s Structural mass 1 DOF example

Ma Mach number

n Length of certain set / vector

p Complex flutter parameter

p Local fluid pressure

p Reduced frequency

$\boldsymbol{q}$ Generalized coordinate vector

q_i Entry of generalized coordinate vector

q_∞ Dynamic pressure

$q_{c,i}$ Local heat conduction

R Ideal gas constant

Re Reynolds number

r_{DK} Lever arm for structural damping D_s and stiffness K_s, 1 DOF example

r_F Lever arm aerodynamic force F_a, 1 DOF example

r_M Lever arm mass M_s, 1 DOF example

s Wing span

Su0 Sutherland number

T Set of interpolation results t_i

t Time

T_{total} Isentropic stagnation temperature

u_i Local fluid velocity in cartesian dimension i

v_∞ Approach flow velocity

W Set of distance weights w_i

W_A Aerodynamic work per cycle performed on structure

W_D Structural damping work per cycle

$\boldsymbol{x}$ Position vector

$\boldsymbol{x}_i$ Entries of base point set X

$x/c, x/c_{loc}$ Relative position on local chord in flow direction

x_i Cartesian coordinate in dimension i

z/d_{loc} Relative profile coordinate

X Set of base points (input displacements for CFD mesh deformation defined at these points)

Mathematical operations or indices

$(\,)_{\text{imag}}$ imaginary part of complex variable

$(\,)_{\text{mag}}$ Magnitude of complex variable

$(\,)_{\text{phase}}$ Phase angle of complex variable

$(\,)_{\text{real}}$ real part of complex variable

$\boldsymbol{a}^T$ Transposed of vector $\boldsymbol{a}$

$\ddot{(\,)}$ Time derivative $\frac{\delta^2}{\delta t^2}$

$\dot{(\,)}$ Time derivative $\frac{\delta}{\delta t}$

$\mathcal{F}(a)$ Fourier transformation of a

$\overline{(\,)}$ 'mean'-operator

$\max(\boldsymbol{a})$ Maximum of $\boldsymbol{a}$

$\min(\boldsymbol{a})$ Minimum of $\boldsymbol{a}$

$\text{Var}(\boldsymbol{a})$ Variance of $\boldsymbol{a}$

1. Introduction

Aeroelasticity describes the interaction of aerodynamic, elastic and inertia forces of flexible structures, surrounded by a flow field. Related disciplines are static aeroelasticity, structural dynamics and flight mechanics. Static aeroelasticity is limited to the interaction of aerodynamics and elastic forces, structural dynamics describe the interaction of elastic and inertia forces and flight mechanics identifies the rigid-body dynamics of aerodynamic and inertia forces. These definitions are summarized in the famous 'Collar triangle' by Collar (1946) in Figure 1.1.

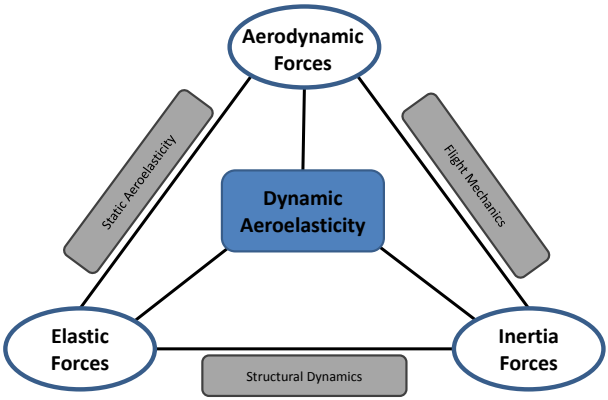

Figure 1.1.: Collar Triangle

Flutter investigations are a very important area of dynamic aeroelasticity. Flutter analysis deals with the dynamic instability of an aeroelastic system. The resulting flutter boundaries are a limiting factor in the development process of commercial transport aircraft. To minimize the operational costs the weight of airplanes is minimized as far as possible. This goal can be achieved by introducing high strength-to-weight ratio materials like carbon fibre reinforced

plastics and by reducing the material quantity, which leads to a reduction of stiffness. A higher flexibility might have positive effects on passive load alleviation of a swept wing due to the direct coupling of bending and twist. However, it might also have a strong negative influence on the flutter boundaries.

The challenge of the estimation of the stability boundaries is determined by the challenge of accurate physical modelling of the three involved disciplines. The precise modelling of structural flexibility and mass during the different development phases is a very demanding task. Usually a ground vibration test is used to validate and update the structural model, see for example Göge (2003), Govers et al. (2015).

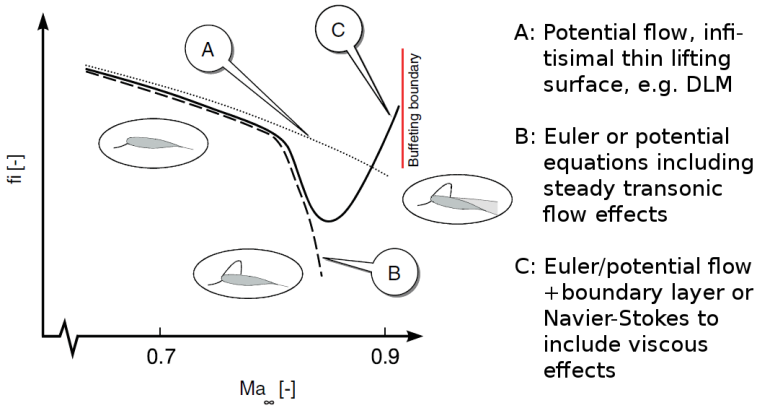

Figure 1.2.: Transonic dip sketch (from Dietz et al. (2006)), flutter index fi represents normalized flutter speed

This document focuses on the unsteady aerodynamic modelling. The most difficult challenge is the computation of transonic aerodynamics combined with flow separation effects: The former tends to decrease the aeroelastic damping while the latter often has a stabilizing effect. This leads to the so called 'transonic dip', see Figure 1.2. Since neither classical methods like the doublet lattice method (DLM) (Albano and Rodden (1969)) nor computational fluid dynamics (CFD) methods neglecting viscous effects like the Euler-method are capable of predicting the transonic dip, the focus of this thesis is the modelling of unsteady aerodynamics in the transonic dip

region by means of the Reynolds-Averaged Navier-Stokes equations. This includes linear stability investigations as well as aerodynamically nonlinear limit-cycle oscillation (LCO) simulations.

Limit-cycles oscillations are defined as self-sustained oscillations with limited amplitudes. An example for limit-cycle oscillations, which many people might have experienced, is snoring. It includes the vibration of parts of the respiratory system, induced by the breathing airstream. In many cases an undamped aeroelastic system will reach an aerodynamically driven LCO state, if no catastrophic failure of the underlying structure occurs before. Therefore, the term limit-cycle flutter is sometimes used. In many cases nonlinearities can be the saving limiter avoiding catastrophic flutter.

There are two classes of LCOs, subcritical and supercritical ones. Figure 1.3 shows graphically the two types of LCOs. In this plot the flow speed U is used as critical system parameter. In principle many different system parameters can make the difference between a damped and an undamped aeroelastic system, e.g. the aerodynamic lift or structural free-play-length parameter.

Supercritical LCOs include a hardening non-linearity. Starting from the flutter point with zero amplitude, the limit-cycle amplitude grows with increasing speed.

Subcritical systems can jump from a linearly damped state (amplitude approximately zero) into an undamped state due to a system disturbance, e.g. a gust encounter. Hence, the dynamic system has two stable states: depending on the start amplitude a bifurcation effect takes place. Bendiksen (2004) also uses the term 'bad flutter' for this condition, since classical flutter prediction does not include such nonlinear effects and its consideration is difficult.

Nevertheless, accurate prediction of LCO amplitudes is, e.g. for failure cases, of great importance for the prediction of high cycle fatigue loads or to assure maneuverability of an aircraft.

Stanford and Beran (2013) showed the appearance of subcritical LCOs for high aspect ratio, highly flexible wings due to structural non-linearities. Nevertheless, the following investigations are limited to supercritical LCOs/flutter. The AEROSTABIL wing did not show indication of subcritical behaviour.

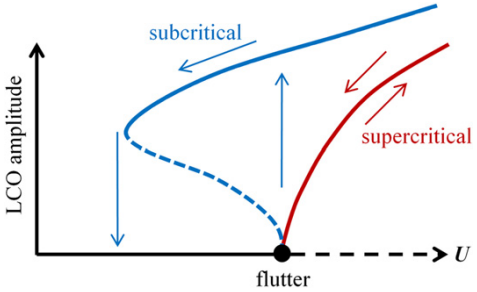

Figure 1.3.: Subcritical / supercritical LCOs, amplitudes versus flow speed U (from Stanford and Beran (2013))

1.1. State of the Art

Aeroelastic stability prediction, or flutter boundary investigation, respectively, have continually developed in the past decades with the increasing computational potential. A milestone for the aerodynamic modelling was the introduction of the doublet lattice method (DLM) by Albano and Rodden (1969). The method is still in industrial use today. Often shortcomings in the transonic region are overcome by usage of windtunnel experiments or higher fidelity aerodynamic methods like CFD for the correction of DLM results, see Baker (1997), Palacios et al. (2001) and Voss and Thormann (2012).

With increasing computer power more sophisticated computational fluid dynamics (CFD) methods have been used for the creation of an aerodynamic model for aeroelastic investigation. The methods increased the prediction accuracy of shock positions and accordingly the shock movement for small perturbations. Furthermore the computing power allowed performing aeroelastic investigation even without correcting DLM. A pulse excitation method with CFD codes has been performed by Cunningham et al. (1988) in combination with a transonic small disturbance method and by Lee and Batina (1993) with Euler and Reynolds-Averaged Navier Stokes methods. While all of above mentioned examples use only linear structural and aerodynamic models for the flutter investigations, the complexity can be further increased through consideration of nonlinearities.

Stickan et al. (2014): "For LCOs to occur, nonlinearities have to

be present in the system, stemming either from nonlinearities in the structure, in the aerodynamics, in the flight control system or as a result of a combination of those. Previous publications divide LCOs into types triggered by structural or aerodynamics effects. Examples for structural LCOs are induced by free-play, as shown by Lee and Kim (1995), geometric nonlinearity, see Tang and Dowell (2004) or additional material nonlinearities as presented by Peng and Han (2011). An industrial example is given by Banavara and Newsom (2010), discussing nonlinear actuators plus free-play in a complete aircraft model. Nonlinear aerodynamic effects, which are also subject of the present work, are the other focus. Several experiments, for example by Dietz et al. (2003, 2004); Schewe et al. (2003) and mainly computational or combined investigations were performed, e.g. for three-dimensional cases by Bendiksen (2008), Edwards et al. (2001), Gordnier and Melville (2001); for two-dimensional case: by Poirel et al. (2011), Raveh and Dowell (2011) or B.Wang and Zha (2011). The aerodynamic LCO-limiter in these publications is either connected with flow separation or transonic shock-(buffet) influences."

The motivation of this thesis is to understand and to theoretically reproduce a series of measurements, which were performed on the so-called AEROSTABIL wing (model B) from the DLR AEROSTABIL project. The experiment aimed at developing a thorough understanding of the static and especially the dynamic behaviour of an elastic wing under aerodynamic loading close to the flutter speed, see Dietz et al. (2003). It enabled the measurements of LCOs for a certain parameter range. The results have also motivated O.O. Bendiksen, who has done detailed LCO research on a similar, theoretical model, called "G-wing". In Bendiksen (2008, 2009) several investigations of this AEROSTABIL-similar wing with identical planform but different airfoil shape and an inviscid Euler CFD-solver are presented. The amplitude limitation is explained with the "structural washout" effect, which is shown to be especially important at transonic flow conditions. The term "structural washout" is used for the local bending-torsion coupling of the first structural bending mode of a backward-swept wing, which results in a reduced local angle of attack on the wing for increased wing bending. It was shown that the load-decreasing pitch motion supports the transition from continuous to intermittent shock motion (Tijdeman type A $\rightarrow$ B,

see Tijdeman (1977)), which decreases the aerodynamic work performed on the structure.

Schewe (2013) uses the Landau equation to model LCOs. The AEROSTABIL experiment is one of the three cases that are discussed in this paper. The similarity of the AEROSTABIL LCOs to another 2D LCO experiment in the same windtunnel is mentioned. Nevertheless, this publication does not discuss the physical mechanism of the AEROSTABIL LCO.

1.2. Objectives

The main objective of this thesis is to gain a physical understanding of the measured limit-cycle oscillations of the AEROSTABIL wing. First numerical studies in Stickan et al. (2014) showed already that the LCO is driven by the aerodynamics. This means that an aerodynamic nonlinearity is responsible for the amplitude limitation. In nowadays aircraft certification process, unsteady aerodynamic nonlinearities are not taken into account in the aerodynamic models for flutter or gust certification. To allow a more accurate physical modelling for future aircraft developments, this experiment offers the opportunity to increase the understanding of unsteady nonlinearities in the aeroelastic context.

The second objective is directly derived from the first one: Since the aircraft design and certification is strongly driven by computational simulations, the available data can be used to validate state-of-the-art aeroelastic simulation methods. The experiment provides a unique data base for this purpose since 3D LCOs, but also stable conditions, are measured with unsteady pressures and acceleration measurement devices. Simultaneously, the validated aeroelastic model can help to analyse the physical effects at locations without measurement devices.

The third objective is to present aeroelastic methods which can not only be applied to the examined AEROSTABIL clean-wing test case, but also to full aircraft configurations of arbitrary level of detail. The contributions to fluid-structure interaction methods mainly involve the CFD-CSM coupling and the deformation of the CFD mesh. An Airbus A340-300 flight test case serves as application and validation example.

1.3. Thesis Outline

This thesis starts with a gentle introduction into the theoretical concepts of aeroelastic stability and limit-cycle oscillations in Chapter 2.

The applied methods are presented in Chapter 3. Included are the aerodynamic and structural solvers, but also the aeroelastic methods to couple the two disciplines. The case of the A340 is used as application example in this chapter.

Two-dimensional unsteady CFD computations with two different profiles are used in Chapter 4 to give a broad introduction into the different effects of unsteady aerodynamics in the context of flutter investigations.

After these introductory parts the focus is moved to the AEROSTABIL windtunnel experiment. The experiment is described in Chapter 5 and the used simulation models are specified in Chapter 6.

The computational AEROSTABIL investigations start with static fluid structure interaction analyses in Chapter 7. Here another special feature of the AEROSTABIL model is presented: The deformation of wing profiles.

In Chapter 8 and 9 the investigation proceeds with dynamic studies. In this context the first chapter considers only one single dynamic degree of freedom (DOF). The analysis of the LCO measurements indicate the possible occurrence of this rare flutter phenomena.

In the subsequent chapter the limitation to one DOF is eliminated. This chapter shows several different investigations of the AEROSTABIL wing to maximise the physical understanding of different effects.

Afterwards a reference case is introduced in Chapter 10. It includes better portable boundary conditions for the overall model. Additionally the chapter offers a mesh convergence study with an aerodynamic model which has been updated with the experience of the previous studies.

Finally, Chapter 11 summarizes the work, gives a conclusion about the overall results and proposes next steps.

2. Concepts and Principles

This chapter provides a very rudimentary introduction into the field of aeroelasticity and especially limit-cycle oscillations. Therefore a simple profile with one rotational degree of freedom is used as example.

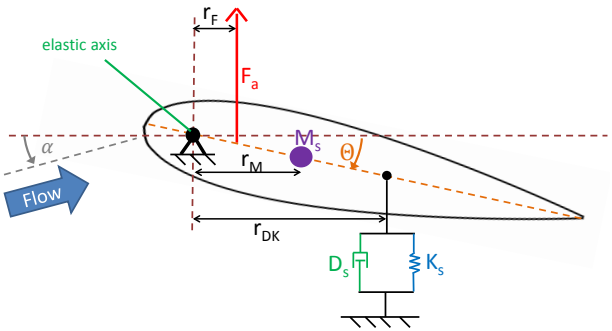

Figure 2.1.: Profile with rotational degree of freedom Θ

The equation of motion can be formulated by setting the sum of moments equal to zero. The lumped mass M_s is used to formulate the moment of inertia $I = M_s r_M^2$, the damping force is computed by $F_D = D_s \dot{\Theta} r_{\mathrm{DK}}$ and the spring force by $F_K = K_s \Theta r_{\mathrm{DK}}$. The aerodynamic moment is defined by $r_F F_a$. Neglecting the static mass force, the overall equation of motion can be written as

$$M_s r_M^2 \ddot{\Theta} + D_s r_{\mathrm{DK}}^2 \dot{\Theta} + K_s r_{\mathrm{DK}}^2 \Theta = r_F F_a \quad . \tag{2.1}$$

2.1. Static Aeroelasticity

For the case of static aeroelasticity the time dependent terms in equation (2.1) vanish. The aerodynamic force F_a is defined as a function of the sum of angle of attack α and the torsion angle Θ : $F_a = F_a(\alpha + \Theta)$. The resulting equation is

$$K_s r_{\mathrm{DK}}^2 \Theta = r_F F_a(\alpha + \Theta) \ . \tag{2.2}$$

For a nonlinear function F_a, the resulting angle Θ can be found with fixed-point iterations.

2.2. Dynamic Aeroelasticity

The dynamic system is based on equation (2.1). By neglecting structural damping and substituting for Θ the homogeneous solution approach

$$\Theta(t) = \widehat{\Theta} e^{\lambda t}, \tag{2.3}$$

this leads to the characteristic equation

$$M_s r_M^2 \cdot \lambda^2 + K_s r_{\mathrm{DK}}^2 = 0. \tag{2.4}$$

The absolute value of the complex roots of this equation, $\lambda_{1,2} = \pm i \sqrt{\frac{K_s r_{\mathrm{DK}}^2}{M_s r_M^2}}$, is the structural eigenvalue ω_0 of the system. Hence, the structural eigenfrequency is

$$f_0 = 2\pi\omega_0 = 2\pi \sqrt{\frac{K_s r_{\mathrm{DK}}^2}{M_s r_M^2}}. \tag{2.5}$$

The structural eigenfrequencies are the harmonic oscillation frequencies of an undamped system without external forces. They are major characteristic attributes of a structure.

To expand the structural system to an aeroelastic system, a simple linear aerodynamic model depending on coefficients a_1 and a_2 is assumed:

$$F_a(\alpha, \dot{\alpha}) = a_1 \alpha + a_2 \dot{\alpha}. \tag{2.6}$$

With $\alpha = \Theta$ equation (2.1) results in the equations of motion

$$M_s r_M^2 \ddot{\Theta} + D_s r_{\mathrm{DK}}^2 \dot{\Theta} + K_s r_{\mathrm{DK}}^2 \Theta = r_F \left(a_1 \Theta + a_2 \dot{\Theta} \right) \ . \tag{2.7}$$

This equation of motion can be integrated in time to monitor the system behaviour. Analysing the system response allows to compute a damping ratio D, e.g. via curve fitting to the magnitude of Θ with

$$\Theta_{mag}(t) = \Theta_0 e^{-\omega_n \cdot D \cdot t} \tag{2.8}$$

as seen in Figure 2.2. The constant ω_n is the angular frequency of the undamped oscillating system.

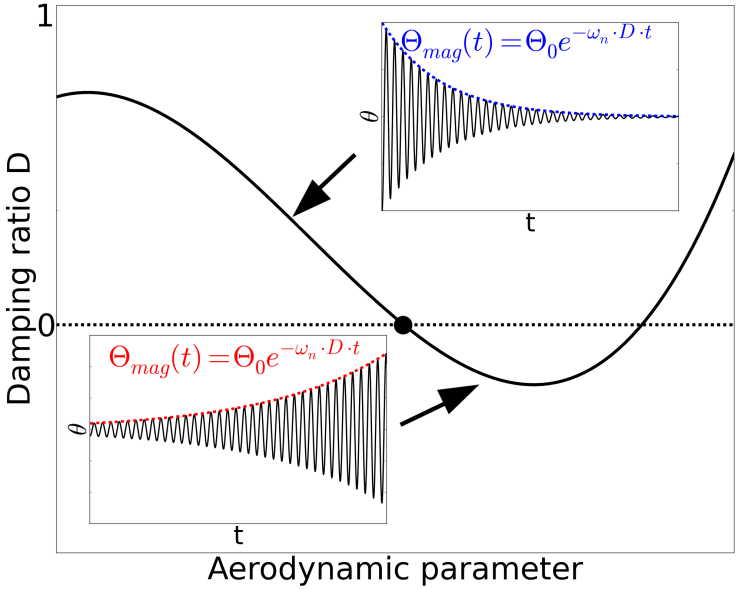

Figure 2.2.: Damping result depending on arbitrary aerodynamic parameter, additionally the system behaviour for 2 different aerodynamic parameter value is visualized by time-domain histories

But this solution can be computed more efficiently by directly solving the equation of motion. To simplify the equation, some

variables are defined:

$$m = M_s r_M^2, \quad d = D_s r_{\mathrm{DK}}^2 - a_2, \quad k = K_s r_{\mathrm{DK}}^2 - a_1 \tag{2.9}$$

Substituting again the approach of equation (2.3) into equation (2.7) leads to the two roots

$$\lambda_{1,2} = -\frac{d}{2m} \pm i\sqrt{\frac{k}{m} - \left(\frac{d}{2m}\right)^2} = -D\omega_n \pm i\omega_n\sqrt{1-D^2} \tag{2.10}$$

with damping ratio $D = \frac{d}{2m\omega_n}$ and undamped angular frequency $\omega_n = \sqrt{\frac{k}{m}}$.

The general solution of the system is accordingly

$$\Theta(t) = \widehat{\Theta}_1 \cdot e^{\lambda_1 t} + \widehat{\Theta}_2 \cdot e^{\lambda_2 t}. \tag{2.11}$$

Inserting λ from (2.10) and rearranging the equation leads to

$$\Theta(t) = \left(\widehat{\Theta}_1 \cdot e^{-i\omega_n\sqrt{1-D^2}t} + \widehat{\Theta}_2 \cdot e^{i\omega_0\sqrt{1-D^2}t}\right) e^{-\omega_n D t}. \tag{2.12}$$

The left bracket of this equation describes a harmonic oscillation, while the out-factored expression $e^{-\omega_n D t}$ describes directly the bounding curve which should be identified for the time-domain analysis in equation (2.8).

Figure 2.2 shows the time domain behaviour for positive and negative damping ratios. Positive damping ($D > 0$) defines damped system behaviour with decreasing amplitudes, negative damping undamped system behaviour with increasing amplitudes. The condition with zero damping marks the flutter point.

2.3. Limit-Cycle-Oscillations

Aeroelastic systems can reach limit-cycle oscillation states if a nonlinearity is present. This section shows two different nonlinearities and the influence on the time histories.

2.3.1. Damper Nonlinearity

An often investigated limit-cycle oscillations depend on nonlinear characteristic curves of dampers in the structure. Let's assume a damper which is modelled very simply via

$$D_s(\Theta) = \begin{cases} 0 & \forall\ \Theta : |\Theta| < \epsilon_{FP} \\ D_{\mathrm{s,lin}} & \forall\ \Theta : |\Theta| \geq \epsilon_{FP} \end{cases} \tag{2.13}$$

This means the damping force is deactivated in the defined Θ range. Since equation (2.7) is not linear anymore with this definition of D, no analytic solution can be found. Therefore a time domain analysis is presented here. With F_a defined as in equation (2.6) for two different start amplitudes Θ_0 the system may behave as plotted in Figure 2.3. It can be observed that the amplitude of Θ decreases or increases until an approximately constant amplitude is reached. At this point in time t the system has reached the limit-cycle state.

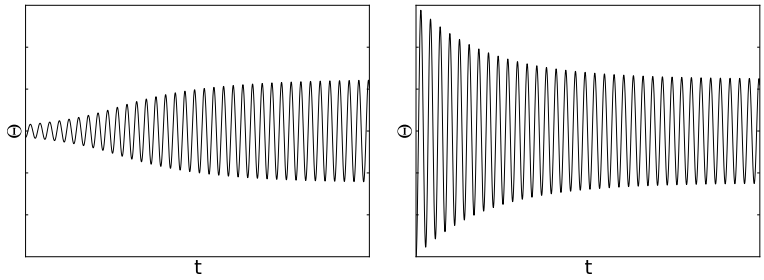

Figure 2.3.: Limit-cycle oscillations with small and large start amplitude

2.3.2. Aerodynamic Amplitude Dependency

A simple aerodynamic nonlinearity may be modelled like:

$$F_a = a_1 \left(1 - b|\Theta^2|\right) \alpha + a_2 \dot{\alpha}\ . \tag{2.14}$$

In this case the aerodynamic forces depend on the deflection of the overall system, similar to a nonlinear stiffness. The aerodynamic

force decreases with increasing values of Θ. Such a nonlinearity can lead to the system response visible in Figure 2.3 as well, depending on the start value of Θ.

One should note: Different nonlinearities can result in similar system responses. Therefore, it should be noted that the source of nonlinearity is difficult to identify for an unknown system.

Furthermore, more complex nonlinearities can lead, depending on the start amplitude Θ_0, to different LCO amplitudes.

3. Methods and Tools

3.1. Computational Fluid Dynamics: TAU

The aerodynamic models used in this document are based on the Reynolds Averaged Navier Stokes equations (RANS) and accordingly for the unsteady case on the URANS equations, respectively. The DLR TAU code is used to solve the equations, see Gerhold and Galle (1997). The focus of this chapter is the physical modelling via the flow equations while solving them is only described very shortly.

3.1.1. Governing Equations

This chapter should give an idea about the governing equations which the TAU code is solving. To get a much deeper insight than the rough sketch presented here, it is referred to Rotta (1972) and Wilcox (1993).

Since the flow conditions, which are investigated in this document, are turbulent and transonic, the starting point must be the compressible conservation equations of mass, momentum and energy. Derived from a small control volume, the conservation equations are given in Cartesian coordinates, in the differential formulation of Rotta (1972) (i, j indices are used for the different spatial coordinate axes, equal indices indicating a sum over all axes: $u_i u_i = u_1 u_1 + u_2 u_2 + u_3 u_3$):

- Mass conservation

$$\frac{\delta \rho}{\delta t} + u_i \frac{\delta \rho}{\delta x_i} + \rho \frac{\delta u_i}{\delta x_i} = 0 \tag{3.1}$$

  where ρ denotes the mass density and u_i the flow velocities;

- Momentum conservation

$$\rho\frac{\delta u_i}{\delta t} + \rho u_j \frac{\delta u_i}{\delta x_j} = -\frac{\delta p}{\delta x_i} + \frac{\delta \tau_{ij}}{\delta x_j} + \rho f_i \quad \forall i \in \{1,2,3\} \tag{3.2}$$

  where τ_{ij} is the shear stress and f_i contains the body forces;

- Energy conservation

$$\rho\frac{\delta h_g}{\delta t} + \rho u_i \frac{\delta h_g}{\delta x_i} = \frac{\delta p}{\delta t} + \frac{\delta\left(u_i \tau_{ij}\right)}{\delta x_j} + \rho u_i f_i - \frac{\delta q_{c,i}}{\delta x_i} \tag{3.3}$$

where the total energy h_g is defined by $h_g = h + \rho u_i^2/2$ with enthalpy h and flow speed u_i.

So altogether for 3-dimensional problems 5 equations are given.

Introducing Stokes' law

$$\tau_{ij} = \mu\left(\frac{\delta u_i}{\delta x_j} + \frac{\delta u_j}{\delta x_i}\right) + \left(\mu_d - \frac{2}{3}\mu\right)\left(\frac{\delta u_k}{\delta x_k}\right)\rho_{ij} \quad , \tag{3.4}$$

containing additionally μ as dynamic viscosity and μ_d as coefficient of pressure viscosity, leads to the Navier-Stokes equations (which in principle means only the momentum equations, but usually implies also the other two). To close the equations Fourier's law of heat conduction

$$q_{c,i} = -\lambda\frac{\delta T}{\delta x_i} \quad , \tag{3.5}$$

the perfect gas law

$$p = R\rho T \tag{3.6}$$

and the relation between specific heat c_p and enthalpy

$$h = c_p T \tag{3.7}$$

is needed. Here the thermal conductivity λ and the ideal gas constant R are used in addition.

Reynolds Averaged Navier Stokes

In principle the above equations can be used in discretized form to compute correct aerodynamic solutions (DNS-Direct Numerical

Simulation). But to compute a correct result for turbulent flows including relatively large Reynolds numbers, which include very small flow features/scales, a very fine discretization is necessary. This leads to too large computational problems for the here investigated flow settings.

Hence, the Navier Stokes equations must be further developed to allow the modelling of these turbulent scales. Therefore the quantities like the velocities are split up by

$$u_i = \overline{u_i} + u_i' \tag{3.8}$$

where $\overline{u_i}$ is the mean (ensemble averaged) velocity field and u_i' the fluctuation part. Hence, $\overline{u_i'} = 0$ but $\overline{u_i' u_j'} \neq 0$. For simplicity constant density ρ is assumed here and the body forces f_i are neglected. Introducing the definition (3.8) in the Navier Stokes equations and applying the mean-operation leads to the incompressible Reynolds equations, or rather the incompressible Reynolds Averaged Navier Stokes (RANS) equations. These contain a similar equation for mass as seen in (3.1) while the momentum equations (3.2) get an additional turbulent term due to the fluctuating velocities:

$$\rho \frac{\overline{u_i}}{\delta t} + \rho\, \overline{u_j} \frac{\overline{u_i}}{\delta x_j} = -\frac{\delta p}{\delta x_i} + \frac{\delta}{\delta x_j} \left(\tau_{ij} - \rho \overline{u_i' u_j'} \right). \tag{3.9}$$

The new term is defined as turbulent stress tensor

$$\left(\tau_{ij}\right)_{tur} = -\rho \overline{u_i' u_j'} \tag{3.10}$$

It represents the momentum transport due to turbulent fluctuations. To regain a closed equation set, turbulence models for $\left(\tau_{ij}\right)_{tur}$ are used. The energy equation (3.3) as well gets an additional term, the turbulent heat transfer term, but further details should be left out here. The derivation of the compressible RANS equations is similar, but for some variables the Favre-averaging must be used additionally. See Wilcox (1993) for more details.

Since simple turbulence models like the mixing length model lead to unsatisfactory results, further transport equations have been developed. For several models the first transfer equation deals with

the turbulent energy

$$\overline{k} = \frac{1}{2}\overline{u_i' u_i'} \quad , \tag{3.11}$$

which is derived from the above equations by subtracting the Reynolds momentum equation 3.9 from the regular momentum equation 3.2 plus some additional algebraic reformulations, dimensional analysis, further assumption etc. For so called 'one equation models' this equation for $\overline{k}$ is the basis for a turbulence model. For 'two equation models' another transport equation is derived, usually either for the turbulent dissipation ϵ (leading to $k-\epsilon$ models) or the specific turbulent dissipation (might be interpreted as turbulent frequency or length, respectively) ω (leading to $k-\omega$ models). But all turbulent models have in common that they are at least half-empiric, containing several constants from experimental studies. Important for the derivations are the assumptions by Kolmogorov:

- Energy transport from large to small scales
- Energy transport to the next smaller scale
- Energy fluctuations can be neglected

Another major approximation has been taken from an idea by Boussinesq (1896). This approximation relates the turbulent stress to the turbulent eddy viscosity μ_t and the speed gradient like

$$\left(\tau_{ij}\right)_{tur} = -\rho\overline{v_i' v_j'} = \mu_t \overline{\left(\frac{\delta u_i}{\delta x_j} + \frac{\delta u_j}{\delta x_i}\right)} - \frac{2}{3}\rho\overline{k}\delta_{ij}. \tag{3.12}$$

δ_{ij} is the Kronecker delta:

$$\delta_{ij} = \begin{cases} 0 & if\ i \neq j \\ 1 & if\ i = j \end{cases} \tag{3.13}$$

However, the turbulent eddy viscosity μ_t is not a constant like the dynamic viscosity μ. It depends on the local flow conditions and flow history effects.

Eventually, since many assumptions, approximations, 2D-considerations and empiric values are used; an overall perfect turbulence model is

unlikely to be found. But it should be mentioned that the time-scales of the turbulent equations do not interfere with the aeroelastic time-scales in the upcoming studies, which are much larger.

In the following sub-paragraphs the two turbulence models used in this document are described shortly. Is must be noted, that not only a satisfying physical representation is important for a turbulence model, but also the numerical properties must allow satisfying convergence.

Spalart-Allmaras (with Edward's Modification) The original model by Spalart and Allmaras (1992) uses one transport equation for the turbulent eddy viscosity only. Several physical assumptions and approximations are used to close the equation system without a further transport equation. The model is probably the most popular model for aeronautical applications. Here the formulation by Edwards and Chandra (1996) is used for the AEROSTABIL investigations, since it offers better numerical characteristics. Furthermore positive experience has been collected using this model, see Brüderlin et al. (2016) and Ritter et al. (2015).

Menter SST The main idea of Menter's BSL (baseline) and SST (Shear-Stress-Transport) model is to combine a $k-\epsilon$ model as formulated by Jones and Launder (1973) and a $k-\omega$ model as formulated by (Wilcox, 1988) to obtain a two-equation model which combines the positive aspects of both. A blending function activates the $k-\omega$ model part in the inner part of the boundary layer, while (with a smooth transition) the model changes over to a $k-\epsilon$-like model in the outer boundary layer. The SST model uses an assumption by Bradshaw et al. (1967) in addition which relates the shear stress to the turbulent kinetic energy. This should overcome the weak point of $k-\omega$ to 'under-predict the amount of separation for severe adverse pressure gradient flows'(Menter (1993)). For more details it is referred to Menter (1993). Several application examples of this model can be found in Menter et al. (2003).

3.1.2. Solution Method

The equations sketched in 3.1.1 are solved within the DLR TAU code, see Gerhold and Galle (1997), Kroll et al. (2005). The equa-

tions are discretized in space using unstructured grids. The TAU code uses the finite volume method, in this case in the cell-vertex formulation. As numerical spatial discretization scheme a central scheme is used; upwind schemes are only used to generate a start solution for the iterations with central scheme. To solve the equation system local pseudo time-stepping is used for the steady computations with a semi-implicit LUSGS scheme, see (Dwight, 2005). For unsteady applications the 2^{nd} order dual time-stepping scheme as proposed by Jameson (1991) is employed. Multigrid techniques are applied to increase the convergence speed, see Jameson (1983). To learn more about computational fluid dynamics it is referred to Blazek (2001).

3.2. CFD Mesh Generation

Nowadays industrial usage of CFD is mainly based on the usage of unstructured, mixed element CFD meshes, since these meshes can be created with reduced manual effort. In the context of this document mainly the mesh generator SOLAR (see Leatham et al. (2000)), but also CENTAUR (see CentaurSoft (www)), have been used.

The starting point for the mesh generation is the CAD (Computer Aided Design) geometry of the domain of interest. The first step is to create a surface mesh, consisting of triangles and quads. In the second step the volumetric mesh is generated by using tetrahedron, prismatic, pyramid and hexahedral elements. This discretization of the target domain must allow discretizing the flow with sufficient accuracy. This implies an increased cell density in regions of enlarged flow variable gradients.

To minimize the number of overall cells, it is very important to create stretched cells in areas where large spatial changes of flow variables in only one or two coordinate directions are expected. The following studies are mainly performed for a classical clean wing configuration at transonic speeds. For this setting large gradients can be expected especially in the boundary layer. Therefore the boundary layer mesh should be build up by prismatic and hexahedral elements, which can easily be made very thin without degrading their numerical properties. This allows gaining an accurate bound-

ary layer discretization. Additionally, the strong curvature at the leading edge and the thin trailing edge of a typical wing leads to the fact that hexahedral elements, which can be stretched very well, should be used as much as possible to minimize the number of cells.

Outside the boundary layer tetrahedron elements are used to discretize the remaining flow domain. Pyramids are used for the transition from hexahedral to tetrahedron elements. See Figure 3.1 to get an impression of the volumetric cell structure.

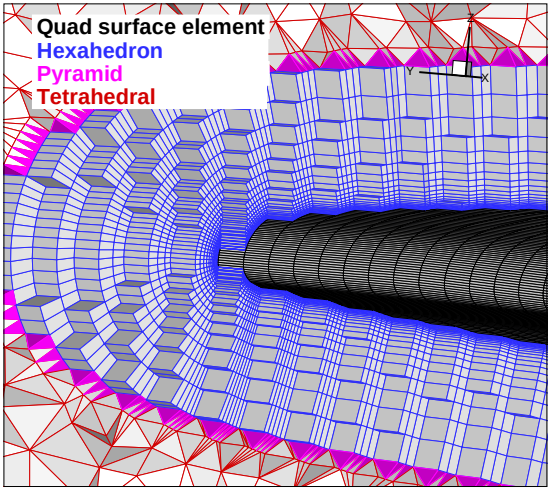

Figure 3.1.: CFD mesh example

For more information on CFD mesh generation it is referred again to Blazek (2001).

3.3. Computational Structural Dynamics: MSC NASTRAN

The commercial solver NASTRAN is used for the structural modelling, see MSC-Nastran (www). The linear static and nonlinear implicit static solution sequences are used. Furthermore the linear real eigenvalue analysis is applied. For a more detailed view on finite element analysis for structural modelling it is referred to Weaver

et al. (1990) and Hughes (2000). For convenience it is switched to the in structural dynamics commonly used matrix notation.

3.3.1. Linear Governing Equations

Similar to the aerodynamic problem the structural domain can be discretized into elements. These elements, which are connecting the nodes, get physical properties fitting to the material. If this model is handled in a linear manner, the elements have only linear properties, which leads for the computation of static equilibrium to an equation system like

$$\boldsymbol{K^*}\ \boldsymbol{dx_s} = \boldsymbol{f_s}\ \ , \tag{3.14}$$

whereas $\boldsymbol{dx_s}$ are the structural displacement caused by the structural forces $\boldsymbol{f}_s$. $\boldsymbol{K^*}$ denotes the stiffness matrix, build up by the linear element properties ('*' here used to identify physical space matrices). While the flow equations contain only elements with equal properties since only single phase flows are considered, the structural elements can have different structural properties. To reduce the computational effort for solid structures, shell and beam elements can be used. For relatively flat or stretched structures these elements use an analytic approximation.

Furthermore a mass matrix $\boldsymbol{M}^*$ is created by the structural solver. It is formed from element densities and concentrated masses in the structural model. These masses can be used for gravitational forces, but are especially important for dynamic effects.

Altogether this leads to the discrete dynamic equations of motion:

$$\boldsymbol{M^*}\ddot{\boldsymbol{dx}}_{\boldsymbol{s}} + \boldsymbol{D^*}\dot{\boldsymbol{dx}}_{\boldsymbol{s}} + \boldsymbol{K^*dx_s} = \boldsymbol{f_s}\ . \tag{3.15}$$

Here the damping matrix $\boldsymbol{D}^*$ is introduced additionally.

3.3.2. Modal Analysis

The natural eigenfrequencies and eigenmodes for an undamped and unstressed system ($\boldsymbol{D^* = 0, f_s = 0}$) equation (3.15) can be transferred to the eigenvalue problem

$$\left(\boldsymbol{K}^* - \omega^2 \boldsymbol{M}^*\right) \boldsymbol{\phi}_s = 0\ . \tag{3.16}$$

Since $\boldsymbol{M}^*$ is symmetric and positive-definite and $\boldsymbol{K}^*$ is symmetric and positive-semidefinite, the eigenvalues ω_i^2 and the orthogonal eigenvectors $\boldsymbol{\phi}_{s,i}$ fulfil

$$\omega_i \in \mathbb{R}, \quad \omega_i^2 \geq 0 \; \forall i \in \{1, n_{Modes}\} \tag{3.17}$$

and, by defining $\boldsymbol{K} = diag\left(\omega_1, ..., \omega_{n_{Modes}}\right)$ and $\boldsymbol{\Phi}_s = \left[\phi_{s,1}, ..., \phi_{s,n_{Modes}}\right]$,

$$\boldsymbol{\Phi}_{\boldsymbol{s}}^{\boldsymbol{T}} \boldsymbol{M}^* \boldsymbol{\Phi}_{\boldsymbol{s}} = \boldsymbol{M} \tag{3.18}$$

$$\boldsymbol{\Phi}_{\boldsymbol{s}}^{\boldsymbol{T}} \boldsymbol{K}^* \boldsymbol{\Phi}_{\boldsymbol{s}} = \boldsymbol{K} \ . \tag{3.19}$$

The diagonal matrices $\boldsymbol{M}$ and $\boldsymbol{K}$ are the generalised mass and stiffness matrix.

In the same manner the generalised damping matrix

$$\boldsymbol{\Phi}_{\boldsymbol{s}}^{\boldsymbol{T}} \boldsymbol{D}^* \boldsymbol{\Phi}_{\boldsymbol{s}} = \boldsymbol{D} \tag{3.20}$$

can be computed, but this matrix is not necessarily diagonal.

The physical eigenfrequencies f_i are defined by

$$\omega_i = 2\pi f_i \ . \tag{3.21}$$

The first n eigenvalues of the eigenvalue problem (3.16) are computed with the Lanczos (1950)-method in NASTRAN.

3.3.3. Generalised Equations of Motion

Introducing the transformation from discrete coordinates $\boldsymbol{dx_s}$ to modal coordinates $\boldsymbol{q}$

$$\boldsymbol{dx_s} = \boldsymbol{\Phi_s q} \ , \tag{3.22}$$

multiplying equation (3.15) with $\boldsymbol{\Phi}_s^T$ and additionally considering equations (3.18) and (3.19), leads to the generalised equations of motion:

$$\mathbf{M\ddot{q} + D\dot{q} + Kq} = \mathbf{\Phi_s^T f_s}, \tag{3.23}$$

This formulation has several advantages. Very important is that dynamic problems can be analysed more comprehensively using the modal coordinates $\boldsymbol{q}$ than by using the discrete coordinates $\boldsymbol{dx_s}$, because the modal coordinates allow to gain a physical interpretation much easier. Furthermore measured eigenfrequencies and

eigenmodes can be used to validate the structural model. Another important aspect is that the entries of the damping matrix $\boldsymbol{D}^*$ or $\boldsymbol{D}$ are in general difficult to obtain. Therefore often a diagonal damping matrix $\boldsymbol{D}$ is used with measured values from a ground vibration test. Last but not least, the computational cost of the model are strongly reduced since all matrices except $\boldsymbol{\Phi}_s$ are diagonal matrices (assuming a diagonal $\boldsymbol{D}$).

To further reduce the number of physical dimension and accordingly the computational effort, especially for dynamic investigations, the number of used eigenmodes / eigenfrequencies n_{Modes} can be further reduced by only selecting a certain number of modes, usually a range of modes starting at the smallest frequency f_{min}. Since in this case the discrete equations of motion are approximated, special care must be taken to select a sufficient number of modes.

3.3.4. Nonlinear Solution Method

The linear, static structural equation (3.14) is only valid for small deformations of linear elastic materials, since the complete deformation is performed in one step with a constant stiffness matrix $\boldsymbol{K}^*$. In general different sources of nonlinearities can get active:

- Geometrical nonlinearities: Large geometric deformations are nonlinear and can therefore not be represented by a linear equation

- Setup change due to load/deformation: Due to deformations or loads the structural setup can change. One example is contact of components due to deformation, or the change of structural properties due to loading (differential stiffness).

- Material nonlinearities: Hook's law is only valid up to yield strength of a material, above nonlinear effects must be considered. Furthermore strain rate dependencies can occur.

NASTRAN's solution 400 is used for nonlinear investigations, see MSC-Nastran-Nonlinear (2013). The solution sequence updates the stiffness matrix $\boldsymbol{K}^*$ within several deformation steps to cover nonlinear effects.

3.4. CFD Mesh Deformation: FSDeformation

The module FSDeformation is used to deform the CFD volume mesh, which is necessary in the aeroelastic processes presented in Sections 3.6.1, 3.6.2 and 3.6.3.

For this purpose radial basis function interpolation is used to interpolate the aerodynamic surface deflection $\boldsymbol{dx_a}$ into the CFD-volume grid. Due to performance issues not all surface input deflections can be used for the RBF-interpolation. Therefore in Section 3.4.3 different methods for the purpose of input data selection are presented and compared. The resulting interpolation error of the surface nodes is eliminated in a correction step. This method is described in Section 3.4.4.

The results presented in this section are the highlights from the publication Barnewitz and Stickan (2013) and the FSDeformation update reporting in Stickan et al. (2013). Further information can also be found in Stickan (2009).

3.4.1. Radial Basis Function Interpolation

"The radial basis functions approach is a well-established interpolation method for gridded and scattered data, whereas the most natural context for function approximation is given for scattered data (Buhmann, 2003, p. 99), (Beckert and Wendland, 2001, p. 4). In the field of computational fluid dynamics (CFD) it is, for example, often used for coupling of CFD-grids to finite element structure grids.

to group g

The input data in d dimensions consist of data sites $\boldsymbol{x}_i$, merged into the dataset

$$X = \{\boldsymbol{x}_1, \boldsymbol{x}_2, ..., \boldsymbol{x}_n\} \in \mathbb{R}^d, \tag{3.24}$$

and the corresponding function values

$$f_i = f(\boldsymbol{x}_i) \in \mathbb{R}, \quad i = 1, ..., n. \tag{3.25}$$

The data sites $\boldsymbol{x}_i$ are called centres or base points.

The goal is to interpolate the function values between the base points by an approximant $s : \mathbb{R}^d \to \mathbb{R}$ to satisfy the condition

$$s|_X = f|_X \,. \tag{3.26}$$

In this specific case s is a linear combination of shifted radially symmetric basis functions ϕ. Radially symmetric means that the value of $\phi(\cdot)$ depends only on the distance of the argument to the origin, hence it is often written $\phi\left(\|\cdot\|\right)$. The distance norm is usually the Euclidean norm

$$\|\boldsymbol{x}\|_2 = \sqrt{\sum_{i=1}^{d} x_i^2}. \tag{3.27}$$

$s(\boldsymbol{x})$ has the general form

$$s(\boldsymbol{x}) = \sum_{i=1}^{n} \alpha_i \phi\left(\|\boldsymbol{x} - \boldsymbol{x}_i\|\right). \tag{3.28}$$

Setting $s(\boldsymbol{x}_i)$ equal to f_i for all $i \in \{1, .., n\}$ leads to the linear system

$$\boldsymbol{A}\boldsymbol{\alpha} = \boldsymbol{b} \tag{3.29}$$

with

$$\boldsymbol{A} = \left(\phi\left(\|\boldsymbol{x}_j - \boldsymbol{x}_k\|\right)\right)_{(j,k)=1,..,n}, \quad \boldsymbol{\alpha} = (\alpha_i)_{i=1,..,n}, \quad \boldsymbol{b} = (f_i)_{i=1,..,n}. \tag{3.30}$$

A unique interpolant is usually (for most ϕ) guaranteed, if the base points are all distinct and there are at least two of them (Baxter, 1992, p.6). An example for a radial basis function could be $\phi\left(\|\boldsymbol{x}\|\right) = \|\boldsymbol{x}\|^2 \log \|\boldsymbol{x}\|$, which is called *'thin plate spline'*. " Barnewitz and Stickan (2013)

In the following section the matrix $\boldsymbol{A}$ is called RBF coefficient matrix. To compute the coefficients in $\boldsymbol{\alpha}$, $\boldsymbol{A}$ must be inverted which has a large influence on the computational costs.

The used implementation uses additionally a linear polynomial to the RBF approach above. This term improves the interpolation quality especially for rigid body movements.

3.4.2. Basic Algorithm Mesh Deformation

The basic algorithm used in FSDeformation is introduced by Heinrich et al. (2008). It is based on a *group-weighting* and a *deformation-blending* approach.

A group-weighting approach is used to allow the independent movement of different model parts/boundaries in the grid and to improve the performance of the deformation algorithm.

The first point is important since the scattered data RBF interpolation of one independently moving component may influence the deformation of another body unintentionally. Separating the interpolation by each group protects the shape of the different components. Therefore, the RBF-coefficient matrix $\boldsymbol{A}^g$ of each group g has to be computed and applied to the grid nodes separately. Finally, the deformation result for each grid point is calculated by a weighted average of each group-deformation result.

In addition this enables a computational more efficient usage of the RBF interpolation: Instead of using all base points in one RBF-coefficient matrix, several smaller matrices can be used. This is very useful since the inversion of $\boldsymbol{A}_g$ is related to the third power of the number of base points for a simple Gauss elimination. This means the group approach allows to use more input data sites without an explosion of the computational costs.

The deformation-blending approach supports the usage of radial basis functions $\phi(\|\boldsymbol{x}\|)$ with limits $\phi(\|\boldsymbol{x}\|) \to \infty$ for $\|\boldsymbol{x}\| \to \infty$. These radial basis functions, which increase with increasing distance to the base point of a deforming body, need to be restricted farther away from the surface of this body. Otherwise local deformations might influence the whole mesh. Additionally, the added polynomial of the interpolation approach would deform the whole volume mesh as well. Thus also this approach that is implemented to recover linear deformations exactly cannot be used without the blending of deformation values.

Consequently the notations are expanded by an elevated group index g for n_g groups. As input data there are n_a^g base points $\boldsymbol{x}_{a,i}^g \in \mathbb{R}^3$ for each group g merged into the datasets

$$X_a^g = \left\{ \boldsymbol{x}_{a,1}^g, \boldsymbol{x}_{a,2}^g, ..., \boldsymbol{x}_{a,n_a^g}^g \right\} \quad \textit{for } g = 1, .., n_g. \tag{3.31}$$

The function values that are going to be interpolated are the deformation vectors

$$\boldsymbol{dx}^g_{a,i} = \boldsymbol{dx}\left(\boldsymbol{x}^g_{a,i}\right) = \begin{pmatrix} dx^{g,x}_{a,i} \\ dx^{g,y}_{a,i} \\ dx^{g,z}_{a,i} \end{pmatrix} \in \mathbb{R}^3 \;\; for\, i = 1, ..., n^g_a, \;\; g = 1, .., n_g, \tag{3.32}$$

which could be used to compute the displaced coordinates $\boldsymbol{x}^g_{\mathrm{new,i}}$ of the base points:

$$\boldsymbol{x}^g_{\mathrm{new,i}} = \boldsymbol{x}^g_{a,i} + \boldsymbol{dx}^g_{a,i} \quad for \;\; i = 1, ..., n^g_a, \;\; g = 1, .., n_g. \tag{3.33}$$

But keep in mind that the aim of the deformation module is to update the mesh nodes and not the base points.

The RBF coefficient matrices $\boldsymbol{A}^g$ for each group can be stated as:

$$\boldsymbol{A}^g = \boldsymbol{A}\left(X^g_a, \phi\right). \tag{3.34}$$

The interpolation algorithm calculates the deformations

$$\boldsymbol{dx}_{\mathrm{v,i}} = \begin{pmatrix} dx^x_{\mathrm{v,i}} & dx^y_{\mathrm{v,i}} & dx^z_{\mathrm{v,i}} \end{pmatrix}^T \tag{3.35}$$

of the volume mesh grid nodes $\boldsymbol{x}_{\mathrm{v,i}}$ by using the distance d^g_i to the nearest surface of group g. With neglected polynomial expansion for every coordinate $k \in \{x, y, z\}$ the governing equations are:

$$dx^{g,k}_{\mathrm{v,i}} = \sum_{j=1}^{n^g_a} \alpha^{g,k}_j \phi\left(\|\boldsymbol{x}_{\mathrm{v,i}} - \boldsymbol{x}_{a,j}\|\right), \;\; g = 1, .., n_g \tag{3.36}$$

$$\mathrm{blend}(\mathrm{d^g_i}, \mathrm{g}) = \begin{cases} 0 & : \;\; d^g_i > \mathrm{RZW^g} \\ 1 & : \;\; d^g_i < \mathrm{RFW^g} \\ \frac{\mathrm{RZW^g} - \mathrm{d^g_i}}{\mathrm{RZW^g} - \mathrm{RFW^g}} & : \;\; \text{else} \end{cases} \tag{3.37}$$

$$\mathrm{weight}(\mathrm{d^g_i}) = \frac{1}{\sqrt{\max\{d^g_i, \epsilon\}}} \tag{3.38}$$

$$dx^k_{\mathrm{v,i}} = \frac{\sum_{g=1}^{n_g} \mathrm{blend}(\mathrm{d^g_i}, \mathrm{g}) \cdot \mathrm{weight}(\mathrm{d^g_i}) \cdot \mathrm{dx^{g,k}_{v,i}}}{\sum_{g=1}^{n_g} \mathrm{weight}(\mathrm{d^g_i})} \tag{3.39}$$

"Two new functions have been introduced: the blending function

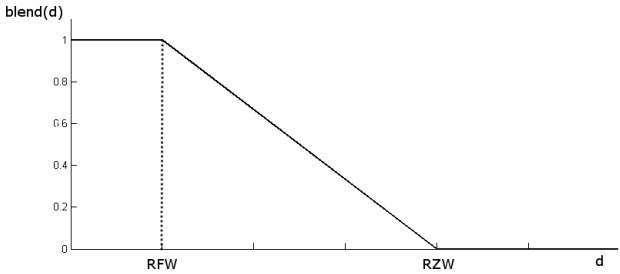

Figure 3.2.: Blending function for grid node deformation computation, including the parameter radius full weight (RFW) and radius zero weight (RZW)

blend(·) and the weighting function weight(·). The weighting function averages the individual group deformations. Because its limit for $d_i \to 0$ is infinity, it needs a cut-off value $1/\sqrt{\epsilon}$ for numerical reasons.

The blending function is sketched in Figure 3.2. With its group-parameters $\mathrm{RZW}^{\mathrm{g}}$ (Radius Zero Weight) and $\mathrm{RFW}^{\mathrm{g}}$ (Radius Full Weight) it is controlling the deformation of the grid nodes. If a grid node is close to a boundary of group g with a distance less than $\mathrm{RFW}^{\mathrm{g}}$, it will move approximately like the boundary. This functionality can be used to conserve the sensitive boundary layer part of a grid. Farther away from the boundary with a distance $d_i^g > \mathrm{RZW}^{\mathrm{g}}$ the deformation is zero.

An example for independently deforming groups can be seen in Figure 3.3. It shows that the surface mesh of the rigid main wing body is not affected by the deformation of the nearby moving flap. The radius zero weight can be recognized in the left plot of Figure 3.3, too. " Barnewitz and Stickan (2013)

The paper by Heinrich et al. (2008) provides test cases showing the usefulness of the presented group weighting approach and the quality conserving capability of the methodology.

A usual application example shows here for an A340-300 case the used deformation groups in Figure 3.4. It can be noted that each lifting surface and the fuselage are in different deformation groups. Additionally a deformation group for the engine, pylons and flap-track fairings is used.

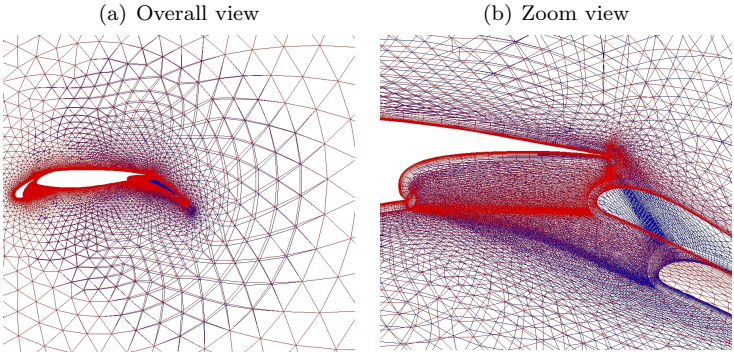

Figure 3.3.: 2d test case, wing including flap and slat. Each of the 3 parts is an independent deformation group and only the flap has input values unequal to zero (undeformed: red, deformed: blue)

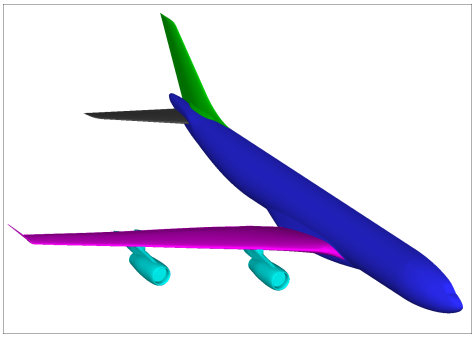

Figure 3.4.: A340-300 example: deformation groups for FSDeformation identified by color

3.4.3. Base Point Selection

The amount of n_a data sites in the CFD surface deformation input, which is related to the length of deformation vector $\boldsymbol{dx}_a$, has a major influence on the performance of the radial basis function interpolation algorithm. As already mentioned the matrix inversion effort depends on the third power of n_a and the interpolation of the grid points depends linearly on the base point number. Since usually the number of base points is very large, a reduction to n'_a base points is indispensable for the mesh deformation module. This point reduction is performed for every deformation group, but the group index is neglected in this section. Different publications have shown methods for this purpose, for example: Allen and Rendall (2008), Michler (2013), and Wang et al. (2015).

"The reduction of base points is not the only way to increase the efficiency of radial basis function interpolation methods. Other possibilities are, for example, multilevel approaches combined with base point reduction Ohtake et al. (2003) or partition of unity approaches like in Wendland (2002). The multilevel approach uses a base point set hierarchy to start the interpolation at a coarse level and then refining it progressively. The partition of unity approach breaks the large problem down to several small ones by partitioning the base points into neighbour sets.

A useful attribute of the radial basis function interpolation approach is that no connectivity information of the input base points is needed. To conserve this characteristic the reduction algorithms do not use connectivity information as well. " Barnewitz and Stickan (2013)

Only the algorithms from Stickan (2009), which showed the best results in approximately five years of industrial application, are presented here.

3.4.3.1. Equidistant Reduction Method

The most simple method tries to select the base points X'_a spatial-evenly distributed from the point set X_a. This is managed by iteratively finding the right minimal distance $d_{\min}$ to possible neighbouring base points, to get as close as possible to the number of desired base points $n_{a,\max}$. Neighbours with a distance less than $d_{\min}$ are

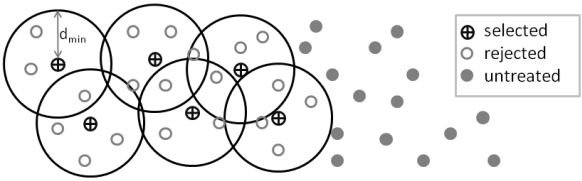

Figure 3.5.: Equidistant reduction snapshot during iteration step, already published in Barnewitz and Stickan (2013)

rejected during this process. Figure 3.5 sketches one iteration step of the algorithm.

The result contains evenly distributed base points. But choosing the base points like this does not take into account the deformation vectors $\boldsymbol{dx}_{a,i}$ or the interpolation error

$$\boldsymbol{e}_a = \left(\| \widetilde{\boldsymbol{dx}}_{a,i} - \boldsymbol{dx}_{a,i} \|_2 \right)_{i=1..n_a} \quad , \tag{3.40}$$

whereas $\widetilde{\boldsymbol{dx}_a}$ is the interpolation result at the input data sites for a base point set X'_a.

3.4.3.2. Error Correction

The error correction algorithm was originally presented by Allen and Rendall (2008). The algorithm tries to correct the $\boldsymbol{\alpha}$-interpolation coefficient vector locally instead by inverting the interpolation matrix $\boldsymbol{A}$ for each single point selection. In each step the interpolation error $e_{a,i}, i = 1, .., n_a$ of all deformation vectors is recomputed and a local update of the α_i in the vicinity of the base point with the largest error is performed.

The paper Allen and Rendall (2008) recommends not to use the updated coefficients $\boldsymbol{\alpha}$ for the interpolation purpose. Instead the selected base points in X'_a should be used for a regular application of the RBF interpolation. The algorithm implemented into the deformation module presented in this document uses this recommendation.

Because the results were not completely satisfactory, this approach has been combined with an initial equidistant reduction step to choose $\mathrm{frac}_{\mathrm{equi}} \cdot \mathrm{n}_{\mathrm{a,max}}$ base points by the algorithm presented in

Section 3.4.3.1.

A big disadvantage of the algorithm is that it only works with radial basis functions $\phi(r)$ with the maximal value for $r = 0$ and locally limited influence range.

3.4.3.3. Distances Weighting by Interpolation Error

This approach is similar to the equidistant reduction approach of section 3.4.3.1. The idea is to weight the distances between two input sites $\boldsymbol{x}_{a,i}$ and $\boldsymbol{x}_{a,j}$ by a weighting factor $w_{i,j}$. Running the point selection with this modification like for the equidistant reduction, the consequence would be an increased point density in areas of higher weights.

The distance $d_{i,j}$ between two points x_i and x_j with associated weights w_i and w_j is calculated by

$$d_{i,j} = \frac{w_i + w_j}{2} \|x_i - x_j\|_2. \tag{3.41}$$

The interpolation error $\mathbf{e_a}$ of the input base points can be used for this purpose. The distance weights

$$W = \{w_1, w_2, ..., w_{n_a}\} \tag{3.42}$$

are in this case equal to the error of interpolated deformation vectors $\Delta\widetilde{X}_a : w_i = e_{a,i}$.

The basic scheme of the algorithm looks like:

- Select start base point set X'_a with corresponding deformation vectors $\Delta X'_a$ by equidistant reduction
- Do n_{EWSteps} times:
  - Interpolate deformations at input points X_a, by using the sets X'_a and $\Delta X'_a$, to get the deformation vectors $\Delta\widetilde{X}_a$
  - Calculate weights w_i by computing the difference of ΔX_a and $\Delta\widetilde{X}_a$
  - Add further base points and deformation vectors by weighted distance reduction to X'_a and $\Delta X'_a$, respectively.

To interpolate the input points X_a in each step, a new interpolation matrix $\boldsymbol{A}_k$ has to be created from the already chosen base points X'_{a} and inverted in every iteration step. Then the error can be calculated by interpolating the deformation vectors $\Delta X'_a$ of these base points to the input set X_a to get the interpolated data set

$$\Delta\widetilde{X}_a = \left\{\widetilde{\boldsymbol{dx}}_{a,1}, \widetilde{\boldsymbol{dx}}_{a,2}, ..., \widetilde{\boldsymbol{dx}}_{a,n_a}\right\} \tag{3.43}$$

and taking the pairwise difference to the input deformation vector set ΔX_a to compute the weights

$$w_i = \|\widetilde{\boldsymbol{dx}}_{a,i} - \boldsymbol{dx}_{a,i}\|_2, \quad i = 1, 2, ..., n_a. \tag{3.44}$$

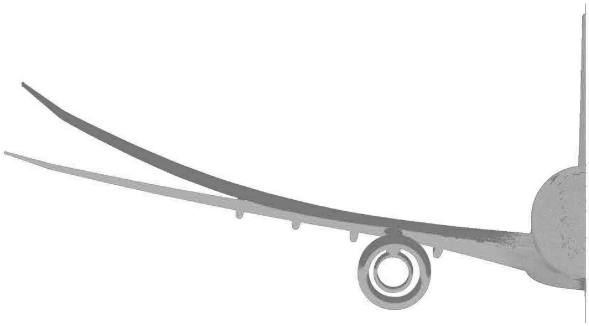

Figure 3.6.: Base point reduction test case, already published in Barnewitz and Stickan (2013)

3.4.3.4. Interpolation Quality Comparison

The different reduction algorithms in section 3.4.3.1 to 3.4.3.3 select different base point sets X'_a from the input data site set X_a. This section is comparing the resulting interpolation errors in a test case.

Therefore the extremely deformed half model airplane, as seen in figure 3.6 is used. The input base points X_a and their deformation vectors ΔX_a were calculated with a structural loads program. The tool generates for each surface grid node a deformation vector, so the cardinality of X_a and ΔX_a is quite large with a value of $n_a \approx 137,000$ for the wing without engine only.

Figure 3.7 shows the interpolation error $e_{a,i}$ for the bottom surface of the wing, because it used to show higher interpolation errors. The settings for the interpolation and base point reduction can be seen in table 3.1.

Reduction method	Parameter ϕ
Equidistant reduction	-
Error correction	$\text{frac}_{\text{equi}} = 0.5$
Error weighting	$\text{frac}_{\text{equi}} = 0.5$, $n_{\text{EWSteps}} = 3$

Table 3.1.: Test settings, Wendland's C^0 with impact radius $r = 20.0$ used as RBF ϕ

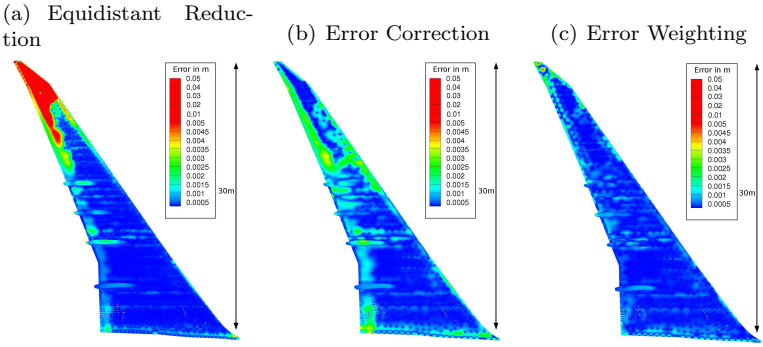

Figure 3.7.: Interpolation error of wing, lower surface view, 2000 base points, color table: absolute interpolation error

The left plot in Figure 3.7 clearly shows that the base points, chosen by the equidistant reduction method, are not satisfactory in the outer wing part. The wing tip area shows strongly increased error values. This result has motivated to improve the base point selection process. The other reduction algorithms show all a strongly improved interpolation error in this part of the wing. The mean absolute error $\overline{\boldsymbol{e_a}}$ of each test case for the 2000 base point setting is given in table 3.2. Furthermore, this table contains the variance $\text{Var}(\boldsymbol{e_a})$ and the maximal error $\max_i(e_{a,i})$.

The table confirms the impression of the given plots: All the new

Reduction method	$\overline{\boldsymbol{e_a}}$ $[m]$	Var $(\boldsymbol{e_a})$ $[m^2]$	max$(\boldsymbol{e_a})$ $[m]$
Equidistant reduction	$2.33 \cdot 10^{-3}$	$2.52 \cdot 10^{-5}$	$4.99 \cdot 10^{-2}$
Error correction	$7.38 \cdot 10^{-4}$	$4.55 \cdot 10^{-7}$	$3.83 \cdot 10^{-3}$
Error weighting	$6.86 \cdot 10^{-4}$	$6.20 \cdot 10^{-7}$	$7.92 \cdot 10^{-3}$

Table 3.2.: Test results interpolation error $\boldsymbol{e_a}$, 2000 base points

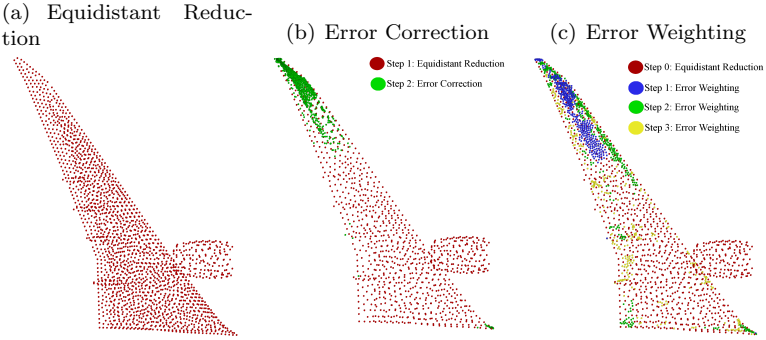

Figure 3.8.: 2000 base points selected by different reduction algorithms

methods choose base points, which result in a significantly lower interpolation error. Furthermore, the variance Var$(\cdot)$ indicates that less fluctuations in the error can be expected. The maximum error is lowered by up to 92 percent.

Figure 3.8 shows how the base points are chosen by the different algorithms. The equidistant reduction algorithm distributes the base points nicely over the whole domain. Taking a closer look, a decreased density of points in the thin parts of the wing, like the trailing edge and the tip, can be recognized.

The new methods have all used the equidistant reduction algorithm in the first step for half of their base points. The remaining half has been selected by the different selection algorithms.

Overall the two approaches based on the interpolation error are choosing their base points similarly. A difference between the error based greedy algorithms is that the error weighting algorithm is distributing the points more numerous in areas far away from the

outer wing. The error correction algorithm has selected most points in the tip area.

Altogether it is shown that the advanced base point selection methods reduce the surface interpolation error strongly. While the error correction method is computationally less expensive, the error weighting algorithm has no restrictions for the used radial basis function. The reduction of surface interpolation error is very important for the correction method in Section 3.4.4.

3.4.4. Nearest Neighbour Correction

The section above has shown efforts to reduce the CFD surface mesh error $\boldsymbol{e}_a$. " This error can be used in a correction step. But it is not possible to correct the surface-points directly, because the thin boundary layer cells of a RANS CFD-mesh would be destructed. Instead a nearest-neighbour correction (NNC) method, which takes all volume nodes into account, is proposed.

For the correction step the nearest surface point $\mathbf{x}_{v,\mathrm{NN}}$ of each volume point $\mathbf{x}_v$ is computed. For each of these surface points the interpolation error $\boldsymbol{e}_a$ is already defined. To get the volume-point errors $\mathbf{e}_v$, the interpolation error of the surface is mapped to the corresponding volume points. But since the correction step should not influence the good mesh quality from the RBF-interpolation, a blending function depending on the surface-boundary distance $\mathbf{d} = (d_1, ..., d_n) = \mathbf{x}_{v,NN} - \mathbf{x}_v$ limits it to an area close to the surface to get the final volume mesh deformation $\boldsymbol{dx}_v$. The blending radii $\mathrm{RZW_{NNC}}$ and $\mathrm{RFW_{NNC}}$ are controlling this blending function

$$blend(d_i) = \begin{cases} 0 & : \quad d_i > \mathrm{RZW_{NNC}} \\ 1 & : \quad d_i < \mathrm{RFW_{NNC}} \\ \frac{\mathrm{RZW_{NNC}} - \mathrm{d_i}}{\mathrm{RZW_{NNC}} - \mathrm{RFW_{NNC}}} & : \quad \text{else} \end{cases} \tag{3.45}$$

to compute the final deformation

$$dx_{v,i} = dx_{v,RBF,i} - blend(d_i) \cdot e_{v,i}, i = 1, ..., n \tag{3.46}$$

The correction value of the volume grid points decays linearly in the region where $\mathrm{RFW_{NNC}} < \mathrm{d_i} < \mathrm{RZW_{NNC}}$. Volume points with boundary distance d_i larger than $\mathrm{RZW_{NNC}}$ are not affected

by the correction step. The RBF-interpolation method uses the same blending function to limit the RBF-volume-mesh deformation to a certain area. But these radii should be selected an order of magnitude larger than the NNC-radii.

Since FSDeformation is already computing the closest surface points during the computation of the wall distances, "..." the additional computation time for the correction step is relatively small. Therefore the good performance and mesh-quality conservation of the deformation module is preserved, but the deficit that a complete surface mesh deformation input cannot be represented in the CFD-mesh is removed. Since the coupling method presented in Section 3.5 computes the deformations for all surface points, this is a very important feature in the context of high-fidelity fluid-structure coupling. " Stickan et al. (2013)

3.5. CFD-CSM Coupling: FSAdvancedSplining

The module FSAdvancedSplining is used to couple the aerodynamic surface nodes to the structural surface nodes. The following section is partly contained in Stickan et al. (2013).

The coupling tool may combine different interpolation methods for different model components. For the case of complex structural models with differently resolved components, this is a very important feature for fluid-structure coupling. Therefore the structural and aerodynamic domain is split into several domains. These domains can be different structural components, or even further divided components to increase the numerical performance of certain interpolation methods.

The general usage of the interpolation matrix $\mathbf{H}_{a,s}$ is the interpolation of the 6 degree-of-freedom (DOF) structural translational and rotational displacements

$$\begin{aligned} \boldsymbol{dx}_s \quad = \quad & \Big[\left(dx_{s,t1}, dx_{s,t2}, dx_{s,t3}, dx_{s,r1}, dx_{s,r2}, dx_{s,r3}\right)_1, \ldots, \\ & \left(dx_{s,t1}, dx_{s,t2}, dx_{s,t3}, dx_{s,r1}, dx_{s,r2}, dx_{s,r3}\right)_{n_s} \Big]^T \end{aligned} \tag{3.47}$$

to the 3 DOF translational aerodynamic displacements

$$\boldsymbol{dx}_a = \left[\left(dx_{a,1}, dx_{a,2}, dx_{a,3} \right)_1, ..., \left(dx_{a,1}, dx_{a,2}, dx_{a,3} \right)_{n_a} \right]^T \quad (3.48)$$

by

$$\boldsymbol{dx}_a = \mathbf{H}_{a,s} \cdot \boldsymbol{dx}_s. \quad (3.49)$$

3.5.1. Coupling Concept

FSAdvancedSplining allows partitioning the structural and aerodynamic surfaces into groups and domains. The first level of partitioning is the group-level. One group can be further split into domains with an arbitrary number of levels. The overall interpolation matrix $\mathbf{H}_{a,s}$ can be written as a product of the relaxation and blending matrices $\mathbf{M}_{Relax}$ and $\mathbf{M}_{Blend}$ and an interpolation methods matrix $\mathbf{M}_{Splines}$:

$$\mathbf{H}_{a,s} = \mathbf{M}_{Relax} \cdot \mathbf{M}_{Blend} \cdot \mathbf{M}_{Splines}. \quad (3.50)$$

The matrix $\mathbf{M}_{Relax}$ joins the different groups and the matrix $\mathbf{M}_{Blend}$ regulates the combination of $n_{domains}$ different spline domains.

The matrix $\mathbf{M}_{Splines}$ contains the different interpolation method matrices:

$$\mathbf{M}_{Splines} = \begin{bmatrix} \mathbf{M}_{Sp\_1} & & & \\ & \mathbf{M}_{Sp\_2} & & \\ & & \ddots & \\ & & & \mathbf{M}_{Sp\_n_{domains}} \end{bmatrix}. \quad (3.51)$$

Each interpolation matrix $\mathbf{M}_{Sp\_i}$ may represent a different interpolation method, see Section 3.5.3. The matrix $\mathbf{M}_{Splines}$ is not block-diagonal, because certain CFD-nodes are influenced by different spline domains due to overlap regions of size $n_{a,Overlap}$. Therefore the matrix has the dimension $3\left(n_a + n_{a,Overlap}\right) \times 6n_s$.

A similar coupling methodology is also contained in MSC-Nastran (www).

3.5.2. Relaxation and Blending

As already mentioned in the previous section, the coupling domains may have an overlap for the structural and aerodynamic nodes. To unite the overlapping aerodynamic domains, the blending matrix $\mathbf{M}_{Blend}$ is used. The overlapping and blending is necessary since usually domain overlaps in the aerodynamic surface are conducted to generate a smooth transition between different domains. Since the blending matrix is only used to join the domains up to the group-level, it looks for n_{groups} groups like:

$$\mathbf{M}_{Blend} = \begin{bmatrix} \mathbf{M}_{Blend\_1} & & & \\ & \mathbf{M}_{Blend\_2} & & \\ & & \ddots & \\ & & & \mathbf{M}_{Blend\_n_{groups}} \end{bmatrix}. \quad (3.52)$$

Each matrix $\mathbf{M}_{Blend\_g}$ represents the blending matrix for the group g. Because a group can consist of several domain levels, each matrix is composed with regard to the $n_{g,domains}$ domain levels as

$$\mathbf{M}_{Blend\_g} = \prod_{d=1}^{n_{g,domains}} \mathbf{M}_{Blend\_g,d} \quad (3.53)$$

A domain-level matrix $\mathbf{M}_{Blend\_g,d}$ contains the information to join the domains of the level d of group g. The blending matrices will only influence nodes which are shared by multiple domains.

Two possibilities exist in FSAdvancedSplining to join domains; here the 'cut-plane-splitting' is shown as example. For this purpose the user defines a cut-plane and a blending-length d_{Blend}. Considering the joining of two domains a and b with shared nodes $X = \{x_1, ..., x_n\}$ (points with distance coordinate $|d_i|/2 < d_{Blend}$ to cut plane) but different interpolation result $T_a = \{t_{a,1}, ..., t_{a,n}\}$ and $T_b = \{t_{b,1}, ..., t_{b,n}\}$, the blended interpolation result $T = \{t_1, ..., t_n\}$ is defined in the following manner:

$$t_i = t_{a,i} \cdot \left(1 - f_B\left(\frac{d_i}{d_{Blend}} + \frac{1}{2}\right)\right) + t_{b,i} \cdot f_B\left(\frac{d_i}{d_{Blend}} + \frac{1}{2}\right) \quad (3.54)$$

at which $f_B(\cdot)$ is a blending function. Possible blending functions are:

- Linear blending: $f_B(x) = x$
- Cubic blending: $f_B(x) = 3x^2 - 2x^3$

Alternatively the 'normal-split' option can be used to split surfaces by a user-defined surface normal.

The relaxation of different coupling groups in $\mathbf{M}_{Relax}$ is applied to guarantee a watertight CFD surface mesh. Therefore a relaxation function, which is in principle a one-sided blending function, is applied. The user must define a relaxation group X_{Relax} and an adjacent group $X_{Adjacent}$. The relaxation is applied to the displacements of the nodes in X_{Relax} while the displacements of $X_{Adjacent}$ will not be changed. In this case the geometric relaxation definition is controlled by the distance to the intersection point set $X_{Intersection}$ of X_{Relax} and $X_{Adjacent}$. The relaxation group displacements $T_{Relax} = \{t_{R,i}\}_{i=1,..,n_R}$ are updated by using the adjacent group displacement of the closest point in $X_{Intersection}$: $t_{Inters,i}$. The distance of a point $x_{R,i} \in X_{Relax}$ to the curve defined by $X_{Intersection}$ is defined by $d_{RS,i}$. A relaxation length d_{Relax} is defined by the user. The displacement update $t'_{R,i}$ is defined by:

$$t'_{R,i} = \begin{cases} t_{R,i} \text{ for } d_{RS,i} > d_{Relax} \\ t_{R,i} \cdot f_B\left(\frac{d_{RS,i}}{d_{Relax}}\right) + t_{Inters,i} \cdot \left(1 - f_B\left(\frac{d_{RS,i}}{d_{Relax}}\right)\right) \\ \qquad \text{for } d_{RS,i} \leq d_{Relax} \end{cases} \tag{3.55}$$

3.5.3. Interpolation Methods

The main types of interpolation methods, which are used for the spline domains, are:

- Radial basis function interpolation: as surface interpolation method with different core functions, as already seen in Section 3.4.1 it uses only translational DOF, example for CFD-CSM coupling also shown by Beckert and Wendland (2001)

- Beam spline: the structural component is represented by a line of nodes, translational and rotational DOF are used to compute the aerodynamic deflections
- Rigid body spline: the structural component is only represented by one node, translational and rotational DOF are used to compute the aerodynamic deflections, can be used to fix aerodynamic components, which are not part of the structural model

Depending on the structural modelling fidelity the best suited interpolation method can be selected. Furthermore it should be noted that the interpolation matrix $\mathbf{M}_{Sp\_i}$ is for certain methods not created explicitly due to memory considerations.

3.5.4. Load Transfer

To guarantee virtual work conservation, the transposed spline matrix is used for the investigations in this document to transfer the aerodynamic forces $\mathbf{f}_a$ to the structural surface nodes to get the structural forces and moments $\mathbf{f}_s$:

$$\mathbf{f}_s = \mathbf{H}_{a,s}^T \cdot \mathbf{f}_a. \tag{3.56}$$

Alternatively a nearest-neighbour force mapping can be used. This feature turned out to be very useful for direct CFD solver calls since the transposed RBF interpolation matrix can have bad properties for CSM meshes with strongly varying node density. In this case each aerodynamic force in $\mathbf{f}_a$ is mapped to the closest structural surface point. Additionally a correction moment is added, depending on the distance of the two force locations.

3.5.5. Coupling Example

Figure 3.9 shows a coupling setup for the A340-300 aircraft. The different groups of the setup are: Wing, horizontal tail plane (left and right), vertical tail plane (VTP), fuselage, inner and outer engine, inner and outer pylon. In the left plot the relaxation areas between the different groups are marked. Overall the two plots show a high number of different domains, identified by the different colours. A

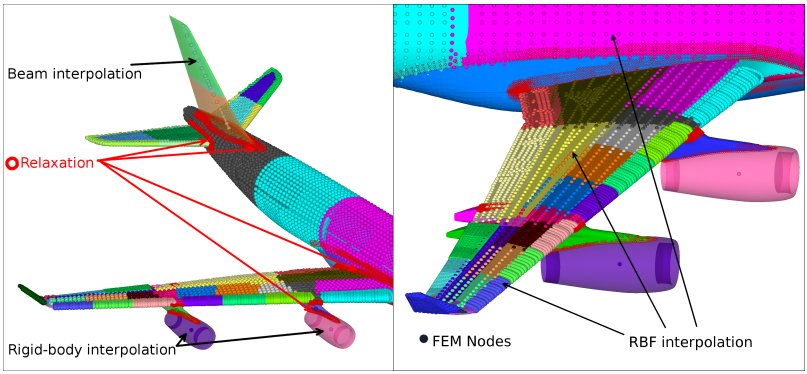

Figure 3.9.: A340-300 Example: CFD-CSM Coupling

large number of scattered FEM nodes in one domain identify a RBF interpolation domain. This is the case for most domains. Only the VTP and fairings are coupled with a beam spline and the engines with a rigid body spline. It can be observed that the domain splitting is used to separate the control surfaces to perform component based interpolation and load transfer. Furthermore it can be noticed that the FEM nodes of a domain are overlapping into the neighbour domain, e.g. on wing box and fuselage. This shows the structural overlap which enables a good interpolation quality in the blending areas between the domains.

An even more complex and rich in detail coupling example using the same coupling tools can be found in Helm et al. (2015).

3.6. CFD-CSM Interaction

3.6.1. Steady: FSNastranInTheLoop

This module is used for static fluid structure interaction. Figure 3.10 depicts how the different modules above are combined for the interaction loop. The structural solver can be either a direct call of the structural solver like NASTRAN, using an exported stiffness matrix $\boldsymbol{K}^*$ or using a generalized structural model. Furthermore the module has several options useful for aeroelastic computations like definition of control surfaces and their rotation for target value

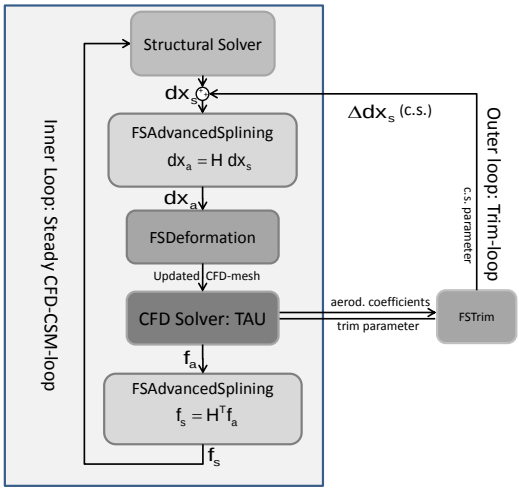

Figure 3.10.: Process sketch FSNastranInTheLoop

trimming.

For trimming, the DLR module FSTrim is used, see Michler (2013). This outer control loop steers the CFD-CSM loop to perform iterations of Newton's method to trim the aeroelastic model to the desired state.

As validation of the static tool chain, data from the Airbus A340-300 Awiator flight test campaign should be employed. The data has already been used by Keye (2011) as CFD-CSM validation case. For the flight test point with $Mach = 0.82$ and altitude=41,000 feet the model has been trimmed to $C_{lift} = 0.59$ and pitching moment C_{my} =0.0. For the structural model the direct Nastran call with inertia relief option has been used to simulate the free-free aircraft. As aerodynamic turbulence model the original Spalart-Allmaras model has been used. Figures 3.11 and 3.12 compare results of FSNastranInTheLoop to the flight test data. The used coupling has already been presented in Figure 3.9 and the FSDeformation groups in 3.4. It can be observed that the agreement to the flight test data is very good. Shock positions are captured well and also bending and twist agree satisfyingly.

Further application examples can be found in Bleecke and Stickan

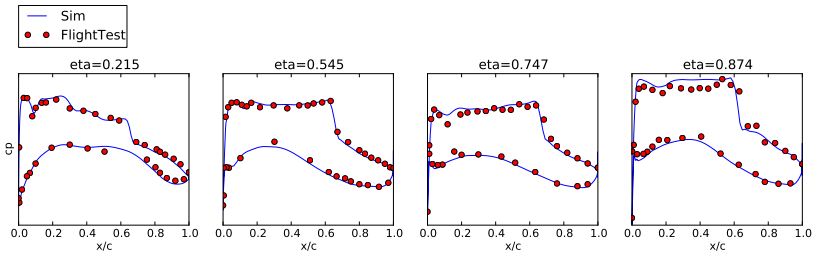

Figure 3.11.: A340 Example: Static pressures wing, $Mach = 0.82$ and altitude=41,000 feet

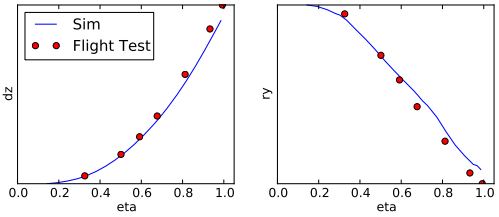

Figure 3.12.: A340 Example: Bending and twist wing, $Mach = 0.82$ and altitude=41,000 feet

(2013) and with MSC-ADAMS as structural multi-body solver in Helm et al. (2015).

3.6.2. Unsteady Time-Domain: FSSwing

For dynamic CFD-CSM computations in the time domain FSSwing is used. The module uses the generalised equations of motion (3.23) in combination with the same modules as FSNastranInTheLoop, see Figure 3.13. In the context of this document the time integration is done with a Newmark predictor-corrector scheme as stated by Bathe and Wilson (1976, p. 322). For unconditional stability reasons the two coefficients of the method are chosen $\delta_{Newmark} = 1/2$ and $\beta_{Newmark} = 1/4$. The resulting static deflections $\boldsymbol{dx_{a,steady}}$ from FSNastranInTheLoop can be used as input for this module.

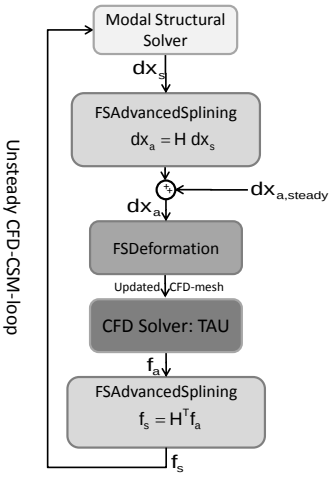

Figure 3.13.: Process sketch FSSwing

3.6.3. Unsteady Aerodynamics: FSForcedMotion

To compute unsteady aerodynamics, especially for frequency domain flutter computations, FSForcedMotion is used. The module is used to compute the unsteady aerodynamics of a prescribed motion. For the purpose of aeroelastic computations this motion is usually defined by the structural eigenmodes $\boldsymbol{\phi}_s$, which are interpolated to the CFD surface mesh by using the interpolation matrix seen in Section 3.5 to get the mode shape $\boldsymbol{\phi}_a$ on the aerodynamic surface. As already seen for FSSwing, static deformation results from FSNastranInTheLoop can be reused as input for this module as well.

The module allows to compute unsteady aerodynamics by several different methods, combining the CFD solver TAU (Section 3.1) and the mesh deformation module FSDeformation (Section 3.4). For the mainly used methods based on time-domain CFD solver calls, the process is sketched in Figure 3.14. The excitation function $f_{Excite}(t)$ depends on the solution method.

In the context of this document mainly the pulse excitation is used, see for example Silva and Raveh (2001) . This method can

be used to compute several different unsteady frequencies by one time domain computation by exciting the aerodynamics with a short pulse. Fourier transformation is used to transfer the aerodynamic answer to the frequency domain. The method can only cover very small amplitude levels. Hence the identified aerodynamics are called linear unsteady aerodynamics. An example time history plot can be observed in Appendix A.2.

Furthermore harmonic excitation is used, in which the aerodynamics are excited by a harmonic, sinusoidal motion. The advantage of this method is that also larger motion amplitudes can be covered, but it is also the most expensive method.

For some general investigations the Linearized Frequency Domain (LFD) solver method is used, see Thormann and Widhalm (2013). It allows to compute small amplitude, linear unsteady aerodynamics with very low computational costs, but is restricted to certain turbulence models in TAU.

A more elaborate introduction and also a comparison of the different methods can be found in Kaiser et al. (2015). The results presented in this paper are based on the same FlowSimulator module.

3.6.4. Unsteady Frequency Domain: p-k-Method

The frequency domain stability boundaries are computed by applying the classical p-k-method to the frequency-domain flutter equation, see Hassig (1971), which is the Laplace-transformation of the generalized equation of motion (3.23). The flutter equation can be written as

$$\left[\left(p\frac{v_\infty}{c_{ref}}\right)^2\mathbf{M}+p\frac{v_\infty}{c_{ref}}\mathbf{D}+\mathbf{K}-q_\infty\mathbf{A}\left(\mathrm{Ma},k\right)\right]\cdot\mathbf{q}=0\ . \quad (3.57)$$

q_∞ denotes the dynamic reference pressure.

The generalized aerodynamic force (GAF) matrix function $\mathbf{A}\left(\mathrm{Ma},k\right)$ for a defined Mach number $Ma = const$ is defined through a GAF matrix $\widehat{\mathbf{A}}$ which contains GAF values for several different reduced frequencies k. The function values of $\mathbf{A}\left(\mathrm{Ma},k\right)$ for different frequencies are interpolated from these sampling points.

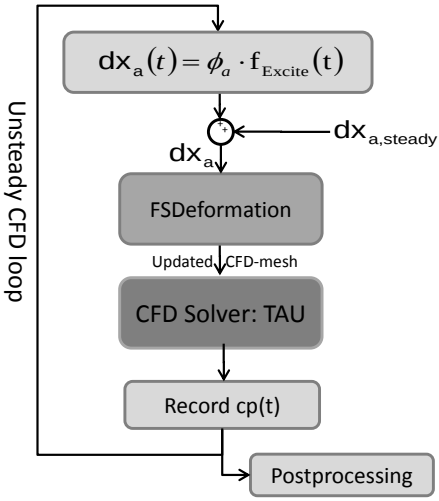

Figure 3.14.: Process sketch FSForcedMotion time domain computation

An entry (m, n) of the GAF matrix $\widehat{\mathbf{A}}$ for a harmonically oscillating eigenmode m, exciting the generalized forces of eigenmode n, is defined by the first harmonic of the transfer function

$$\widehat{\mathbf{A}}_{m,n} = \frac{1}{q_\infty} \frac{\mathcal{F}(\mathbf{\Phi}_{s,n}^T f_s\left(q_m(t)\right)}{\mathcal{F}(q_m(t))} \tag{3.58}$$

$\mathcal{F}(\cdot)$ identifies the Fourier transformation. The reduced frequency k is defined as:

$$k = \frac{2\pi f c_{\text{ref}}}{v_\infty} \tag{3.59}$$

This means the frequency f is normalized with a reference length c_{ref} and v_∞, the reference air-speed.

The entries in $\widehat{\mathbf{A}}$ are computed with FSForcedMotion as seen in Section 3.6.3.

The aeroelastic damping ratio D can then be computed via the non-dimensional, complex flutter parameter p in 3.57,

$$p = \delta + ki \tag{3.60}$$

resulting from the eigenvalue-problem solved with the p-k-method, by

$$D = \frac{-\delta}{\sqrt{k^2 + \delta^2}}. \tag{3.61}$$

3.7. FlowSimulator

The modules including CFD are coupled within the FlowSimulator software environment, see Meinel and Einarsson (2010). This environment provides numerous functions for computational parallel data handling and data exchange between the different modules without file input/output. Therefore it is the backbone of the here presented multidisciplinary simulation tools. While the computational intensive methods are based on the programming language C++, a control layer based on Python allows the fast development of tools. Hence, also the other here presented modules include a python and a C++ layer.

4. Aspects of Unsteady Aerodynamic Effects for Flutter

This chapter should give an introduction to the unsteady aerodynamic effects that should be considered in aeroelasticity. This implies motion induced unsteady airloads, as needed for time-domain and frequency domain flutter computations. But no interaction of structure and aerodynamics is considered, only harmonically forced motion. The chapter neglects other sources of unsteadiness in flows like shock buffet or unstable large scale eddies as in a Kármán vortex street. To learn more about unsteady aerodynamics it is also referred to Tijdeman (1977).

FSForcedMotion has been used with the LFD solver or the harmonic excitation, see 3.6.3, to compute the aerodynamic answer to a pitching motion of two different 2D profiles. If not described differently the results have been computed with the original Spalart-Allmaras turbulence model and the LFD solver. The linearisation for the LFD solver implies always a very small physical motion amplitude. The following considerations are restricted to computational results. Especially the results for strongly separated flows or very high Mach numbers should be interpreted very carefully.

The unsteady lift transfer function due to pitch motion can be extracted from the GAF matrix $\widehat{\mathbf{A}}$, as introduced in Section 3.6.4, for a two-dynamic- degree-of-freedom system with a pitch and a heave mode. This non-diagonal entry of $\widehat{\mathbf{A}}$ is represented by $\widehat{C_{\text{lift}}}$. The pitch mode is defined as a rotation around the leading edge with one degree amplitude. But it should be kept in mind that the mode amplitude is not the computation amplitude (which is usually much smaller).

Two different profiles have been used. The relatively thick NACA 64A-010 and the much thinner NACA 0003, see Abbott and Von Doen-

hoff (1959). Both profiles are symmetric and not necessarily designed for the here shown flow conditions. The aerodynamic chord of the profiles is $c = c_{\text{ref}} = 1$ meter.

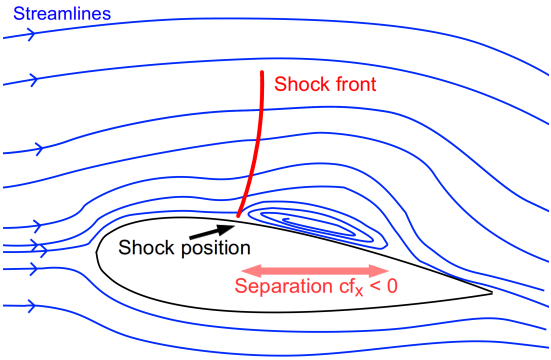

Figure 4.1.: Sketch of steady 2D flow features

The steady flow regime for the investigations below includes transonic shocks and flow separation. A principle drawing of such flow features can be seen in Figure 4.1. It includes the shock position which is the root point of the transonic shock front and also a separation bubble. For separated flows the skin friction cf_x is smaller than zero and it is therefore used in the following sections to determine the separation bubble size.

4.1. Influence of Reduced Frequency

The most important parameter for unsteady aerodynamics is the reduced frequency $k = 2\pi f c_{\text{ref}}/v_\infty$. A reference speed v_∞ and a reference length c_{ref} are used to eliminate the dimensions of the physical frequency f. Figure 4.2 reveals the strong influence of the reduced frequency on the unsteady lift transfer function $\widehat{C_{\text{lift}}}$. It can be noted that with increasing frequency the amplitude is decreasing in this case, while the aerodynamic phase lag is first decreasing up to $k \approx 0.2$ and afterwards starting to increase again. This strong dependency of the reduced frequency is also reflected in the work by Theodorsen (1935), who derived analytic equations to describe

the unsteady aerodynamics of airfoils. The work shows that the reduced frequency is a fundamental parameter for the description of unsteady aerodynamics.

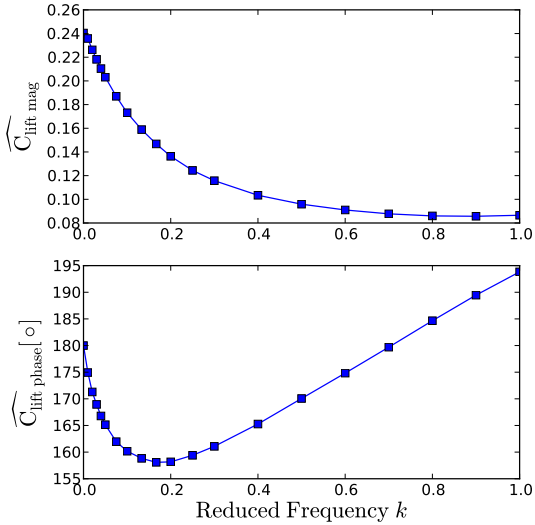

Figure 4.2.: Influence of reduced frequency k on $\widehat{C_{\text{lift}}}$, NACA0003, Ma=0.8 for standard atmosphere sea level, pitch mode

4.2. Influence of Steady Aerodynamics and Inverse Shock Motion

For transonic and separated flows the unsteady aerodynamics depend strongly on the steady flow state. In the case depicted in Figure 4.3 the influence of the angle of attack α is illustrated. This complex figure shows the relation between the shock position, flow separation and the resulting unsteady pressures. In other words, it illustrates the shock-boundary layer interaction for unsteady aerodynamics. The right column shows the connection of steady local pressures and skin friction and the local unsteady pressures for three angles of attack. The left column presents for an α-polar the global

behaviour of steady and unsteady lift coefficient, shock position and separation area.

The upper plot on the left side shows the steady polar C_{lift} vs. α. The plot below shows the shock position and the separation area on the upper profile surface. It should be noticed that C_{lift} is relatively linear until the flow starts to separate. The two upper plots on the right show the local steady pressure coefficient cp_{steady} and the skin friction in x-direction, cf_x. The shock position of the plot on the left has been identified by the largest gradient of $\delta cp_{steady}/\delta x$. The flow separation area has been identified with $cf_x < 0$.

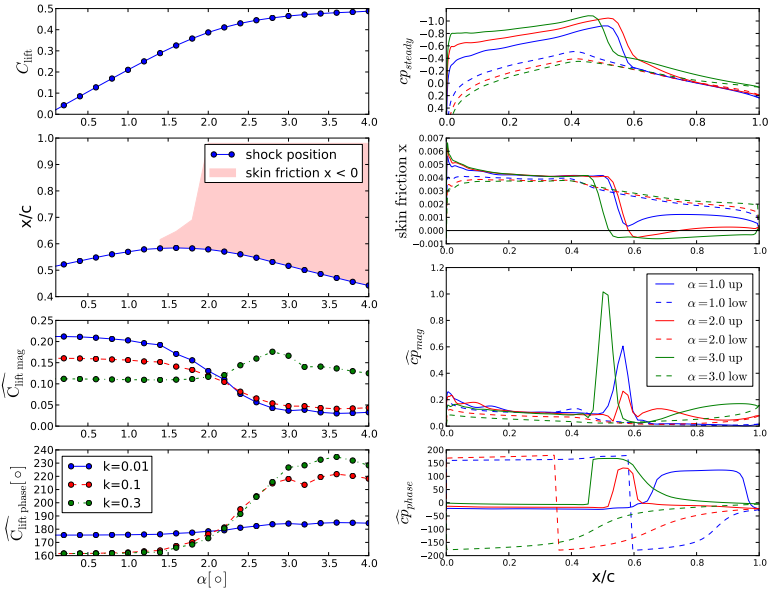

Figure 4.3.: Influence of steady aerodynamics for NACA 64A-010, Ma=0.8, standard atmosphere altitude = 0 feet: left - steady and unsteady lift and flow features vs. angle of attack α, right - steady and unsteady pressures (k=0.1) and surface skin friction for 3 different α of this polar

The two lower plots on the left side show the unsteady results for three reduced frequencies k. The lift transfer function $\widehat{C_{\text{lift}}}$ is

relatively constant as long as the flow is not separated. When the steady linear range without separation is left, the unsteady result also changes strongly. The lower the frequency, the more the amplitude decreases. The phase of $\widehat{C_{\text{lift}}}$ shows naturally for the very low reduced frequency of k =0.01 only small changes. The higher reduced frequencies show a large change when the separation occurs.

The unsteady pressure transfer functions $\widehat{cp}$ are presented in the two bottom plots on the right side for three different angles α. It can be identified that the amplitude of the upper wing surface shows a peak at the shock position. This is the case because of the strong sensitivity of the shock position to profile motion and the large pressure gradient at the shock location. The phase of $\widehat{cp}$ shows also a large shift at the shock position. This phase shift can be explained by the gas kinetic shock conditions. For a pressure increase upstream of a shock a pressure decrease is expected downstream, which leads to a phase shift.

The steady pressures on the right and also the shock-position plot on the left show that the shock position moves downstream approximately as long as no larger flow separation is visible. Afterwards the steady shock position moves upstream. In the unsteady context the expression to describe this behaviour is **'inverse shock motion'**. This phenomena leads also to the strongly changing phase of the unsteady pressures for different angles of attack. Important to note here is that the transonic phase jump in $\widehat{cp}_{\text{phase}}$ is for $\alpha = 1.0$ degree directly downstream of the shock magnitude peak in $\widehat{cp}_{\text{mag}}$. For the other two cases $\alpha \in \{2.0, 3.0\}$, for which the shock moves already upstream with increasing α, there is a first phase jump at the beginning of the shock magnitude peak and a second further downstream. This shows the inverse shock motion in the unsteady pressures.

Figure 4.4 shows similar effects for the NACA 0003 profile for two different Mach numbers. The left plot for Ma=0.8 shows that the unsteady aerodynamics can still behave relatively constant with mild flow separation. Again in the area of inverse shock motion the unsteady phase of $\widehat{C_{\text{lift}}}$ starts to change strongly. For the smaller frequencies the separation is also reducing the magnitude of $\widehat{C_{\text{lift}}}$.

The larger Mach number Ma=0.85 shows a similar behaviour, although in this case the magnitude is already changing stronger for unseparated flows. The strong movement of shock position (and

(a) Ma=0.8 (b) Ma=0.85

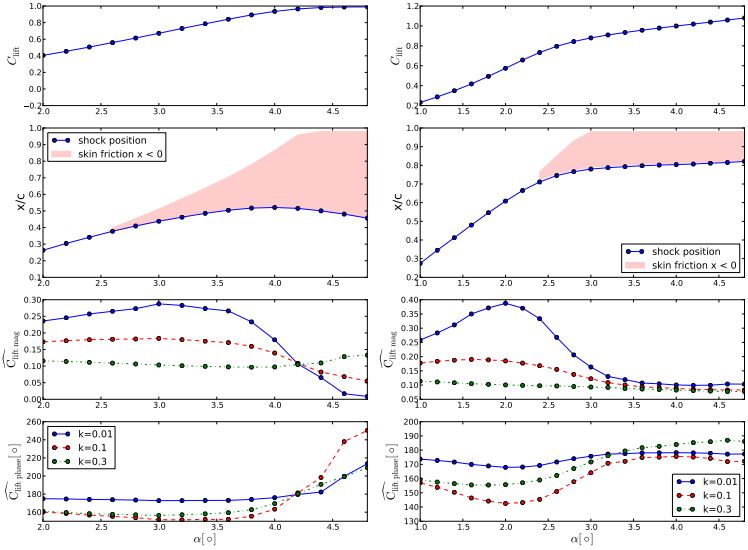

Figure 4.4.: Influence of angle of attack α for NACA 0003, standard atmosphere altitude = 0 feet

therefore changing intensity) can explain this behaviour. This effect is reduced with increasing frequency. Furthermore the plot shows, that also without inverse shock motion the unsteady phase of $\widehat{C_{\text{lift}}}$ can change strongly for different α.

This section already indicates the difficulties in the forecast of unsteady air loads.

4.3. Comparison of CFD and DLM

The standard method for the computation of unsteady aerodynamics is the Doublet-Lattice Method (DLM). As already mentioned in Chapter 1 the method is not well suited for transonic Mach numbers. This section compares the unsteady lift transfer functions $\widehat{C_{\text{lift}}}$ for three Mach numbers $Ma \in \{0.5, 0.8, 0.85\}$ to show this difference of

DLM and CFD. For the NACA 0003 and the NACA 64A-010 profile the lift coefficient is C_{lift}=0.2.

In Figure 4.4 it is presented that the NACA 0003 does not show flow separation at the here investigated lift C_{lift}=0.2 for $Ma = 0.85$. This is also indicated for $Ma = 0.8$, since no separation is visbile for C_{lift}=0.4. The NACA 64A-010 shows attached flow for Ma=0.8 (see Figure 4.3), but separated flow for Ma=0.85. For $Ma = 0.5$ no separation should be expected for both profiles.

The 2D DLM aerodynamics have been computed with an extremely stretched 3D (quasi 2D) wing. NASTRAN has been used for this purpose.

The plots in Figure 4.5 show clearly the increasing difference of DLM and CFD with increasing Mach number. For the subsonic Mach number Ma=0.5 DLM and the 2 CFD solutions agree best, although thickness effects covered in CFD are increasing with rising reduced frequency k. For the largest Mach number the strong influence of the separation on the NACA 64A-010 can be recognized in the CFD results. Amplitude and phase show a qualitatively different behaviour which cannot be reproduced by DLM. Even for the NACA 0003 with attached flow almost 20 degree difference in phase and up to approximately 30 percent difference in magnitude can be seen.

4.4. Influence of Mach Number

This section should show the origin of the transonic dip as seen in Chapter 1, Figure 1.2. Therefore computations with the two profiles have been performed for a range of Mach numbers at C_{lift}=constant. Figure 4.6 shows the results for the NACA 0003 at C_{lift}=0.4 and for the NACA 64A-010 for C_{lift}=0.2. While the NACA 0003 does not separate within the complete Mach-range, the NACA 64A-010 shows separation for $Mach \geq 0.81$.

For the NACA 64A-010 it can clearly be seen that the unsteady lift $\widehat{C_{\text{lift}}}$ magnitude increases up to the separation point and afterwards it reduces strongly for larger Mach numbers. Assuming the change in phase of $\widehat{C_{\text{lift}}}$ is not strongly affecting the dynamic system, this behaviour explains why the flutter speed increases at this point as seen in the transonic dip sketch in Figure 1.2.

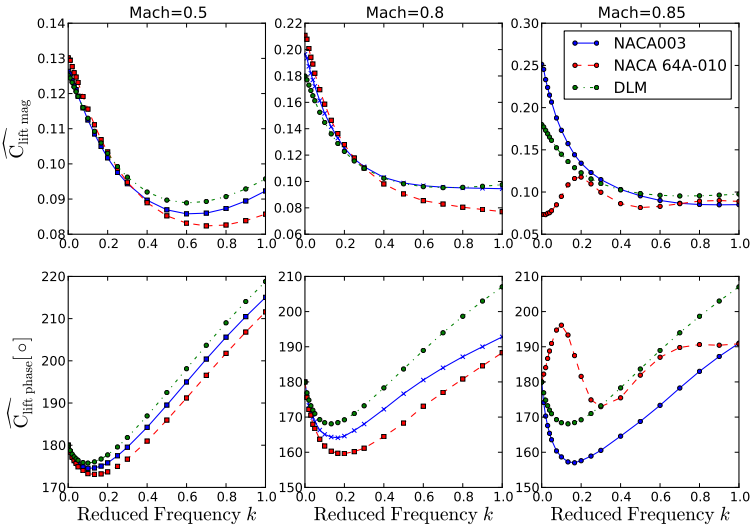

Figure 4.5.: Comparison CFD to DLM, C_{lift}=0.2 for NACA profiles, standard atmosphere altitude 0 feet

But also the unseparated NACA 0003 shows a peak in the magnitude of $\widehat{C_{\text{lift}}}$. However, this peak seems to be very diverse for the 3 reduced frequencies k. It can, therefore, be stated that the transonic dip is not necessarily related to flow separation. In this case the arrival of the shock at the trailing edge leads to a limitation of the unsteady shock movement.

An often used method to find the critical transonic dip Mach number is to find the maximum of $\delta C_{\text{lift}}/\delta\alpha$. This measure is equal to a zero-frequency unsteady result as seen in this chapter. Usually, it works for more complex 3D configurations as well since the criterion shows the Mach number where the transonic shocks have the strongest influence on the unsteady aerodynamics. However, criterion works only for a viscous transonic dip, as the two profiles show: The NACA 64A-010 shows the amplitude peak at a similar Mach numbers for all 3 frequencies due to the flow separation. In contrast to that the maximal amplitude is located at different Mach numbers for the NACA 0003. Hence, the $\delta C_{\text{lift}}/\delta\alpha$ criterion is not working.

(a) NACA0003, $C_{\text{lift}} = 0.4$ (b) NACA 64A-010, $C_{\text{lift}} = 0.2$

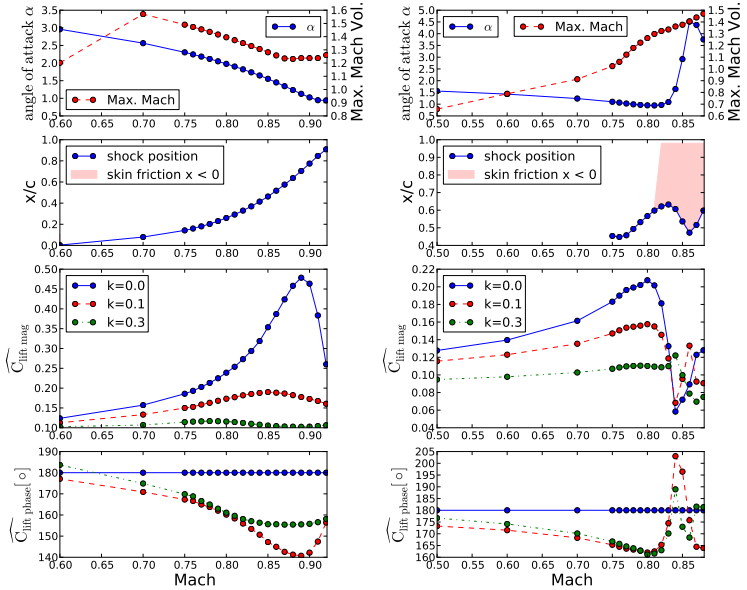

Figure 4.6.: Influence of Mach number: standard atmosphere altitude = 0 feet

4.5. Influence of Motion Amplitude

Nonlinearities are of special importance for the limit-cycle oscillations which are investigated in this document. Figure 4.7 shows the influence of the motion (pitch) amplitude on the unsteady lift $\widehat{C_{\text{lift}}}$ for three Mach numbers. Since the Linearized Frequency Domain (LFD) solver cannot resolve nonlinear aerodynamic effects, the computations for this section have been performed by harmonic time-domain computations with varying amplitude.

The tests with both profiles show a constant unsteady lift for a range of very small amplitudes. But at a certain amplitude $\delta\alpha_{\text{NL}}$ this transfer function $\widehat{C_{\text{lift}}}$ starts to change significantly. The range of constant $\widehat{C_{\text{lift}}}$ is referred to as linear unsteady aerodynamics.

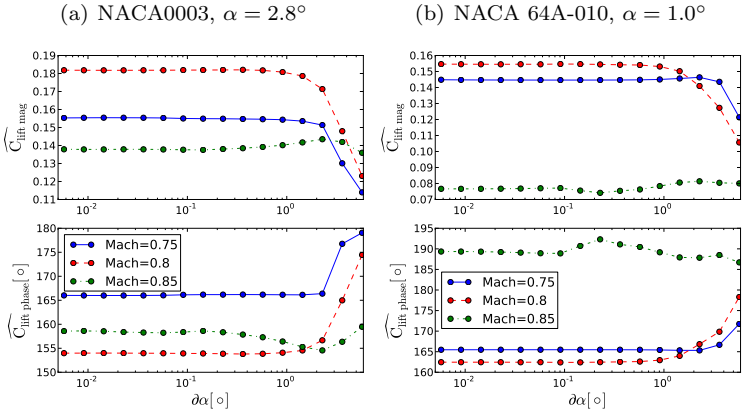

Figure 4.7.: Influence of motion amplitude, reduced freq. k=0.1, standard atmosphere altitude=0 feet

When the amplitude has increased to $\delta\alpha_{\text{NL}}$ and further, nonlinear unsteady aerodynamics can be observed.

Both profiles show that this nonlinear onset amplitude level $\delta\alpha_{\text{NL}}$ decreases with increasing Mach number. This can be explained with the increasing sensitivity of the flow against growing transonic flow effects. If the amplitude increases or decreases with growing motion amplitude, bifurcation effects can occur for aeroelastic system, as seen in Figure 1.3. With increasing amplitude unsteady forces can result in the subcritical branch, while decreasing unsteady forces lead to a supercritical behaviour.

4.6. Turbulence Modelling

Finally this section considers the sensitivity of unsteady aerodynamics to the selected turbulence model for the NACA 64A-010. Therefore the Menter SST turbulence model is used in addition, see Section 3.1.1. Figure 4.8 shows for a constant Mach number the steady lift, shock position and flow separation area for different angles of attack α. Additionally, the unsteady lift $\widehat{C_{\text{lift}}}$ is plotted. It can be observed that the steady lift and the shock position agree very well

comparing the two turbulence models. Differences in the steady flow characteristics can only be observed for the flow-separation area: Although the Menter SST model shows the first separation bubble for the same angle of attack as the Spalart-Allmaras model, the separation area grows more slowly with increasing angle of attack.

The unsteady lift $\widehat{C_{\text{lift}}}$ shows a very good agreement for the two turbulence models as long as the flow is attached. With increasing flow separation area the differences between the two models increase.

Hence it should be noted, that the selection of an adequate turbulence model is essential for the prediction of unsteady aerodynamics. But the challenge is that usually proper validation data is missing to make the best choice.

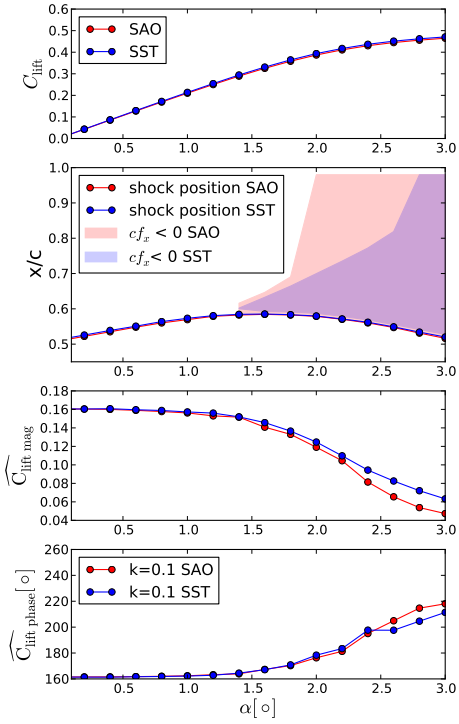

Figure 4.8.: Influence of turbulence modelling, Mach=0.8, standard atmosphere altitude=0 feet, NACA 64A-010

5. Description of AEROSTABIL Experiment

5.1. Limit-Cycle Oscillation Experiment

Figure 5.1.: AEROSTABIL model in DNW-TWG

The AEROSTABIL experiment, which is the basis for the following investigations, has been performed in the Transonic Windtunnel Göttingen (DNW-TWG) in 2002/2003. The paper of Dietz et al. (2003) describes the structural properties of the windtunnel model, but also shows results of the static aeroelastic measurements and preliminary results of observed transonic dynamic phenomena. The non-catastrophic flutter effects, namely the measured limit-cycle oscillations, are the motivation for this thesis.

The main aim of the experiments was to study the static aeroelastic effects and in particular the flutter behaviour of an generic transport aircraft elastic swept wing. The wing planform and the instrumentation, which has been used for the following studies, are

sketched in Figure 5.2. The model has a supercritical airfoil and is equipped with 93 pressure transducers in three wing sections. The measuring system can measure the pressure with relatively high sampling rates, allowing a proper resolution of the expected unsteady flow characteristics. In addition, accelerometers were installed to obtain information about the oscillating wing deflections. Pressure and acceleration measurements were performed for (seemingly) static as well as for oscillating conditions. The experiments were performed in the adaptive test section with solid walls (cross-sectional area: $1 \times 1\ m^2$) of the DNW-TWG.

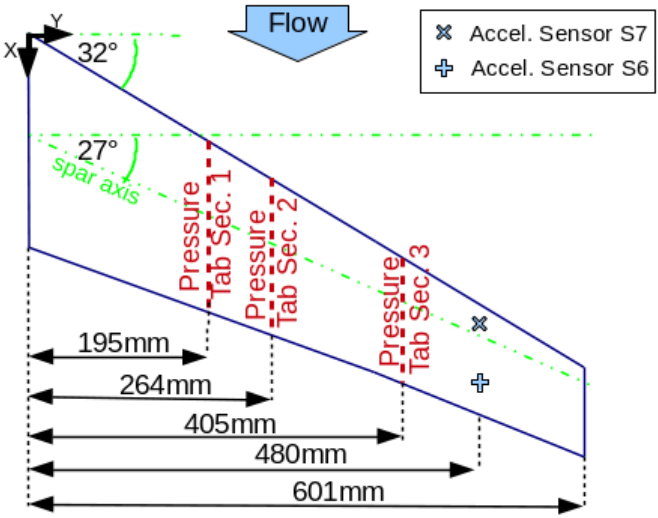

Figure 5.2.: AEROSTABIL wing sketch and used instrumentation

The span of the wing model, without wing tip, amounts to $s = 600.9$ mm and the reference chord length is $c_{ref} = 183$ mm. The sweep angle of the spar axis is 27 degrees and of the leading edge 32 degrees. The wing thickness with respect to the local chord length is nearly constant along the span and amounts to approximately 10 percent. The aspect ratio of the wing is $AR = \frac{s^2}{A_{ref}} = 3.68$. The wing model was mounted on a turntable device. This device was used to rotate the model perpendicular to the windtunnel side wall to adjust the angle of attack α. The rotation centre was located

x_{rot}=0.192m downstream of the leading edge. To force the laminar/turbulent transition, a transition strip was applied on the upper and the lower side at 7.5 percent of the local chord length. The first bending mode of the wing has an eigenfrequency of 37.2 Hz; further characteristic frequencies can be found in Table 6.1 of Section 6.2. Two accelerometers considered in this study were located at $y/s = 0.795$. The exact positions in the coordinate system of Figure 5.2 are $S_{6,xy} = (381\ mm, 480\ mm)$, $S_{7,xy} = (311\ mm, 479\ mm)$. To obtain displacement information, the signals were integrated twice.

The flutter experiment was conducted in the following way: at constant Mach number, the pressure in the windtunnel and angle of attack α was adjusted to a value slightly below the assumed critical point for the onset of the flutter oscillations. Then the angle of incidence was increased in small steps of $\Delta\alpha = 0.1°$ by the hydraulic actuator. The boundary of stability was reached, when the onset of self-excited oscillations of the wing occurred. Figure 5.3 shows an example for such a flutter onset depending on the angle of attack.

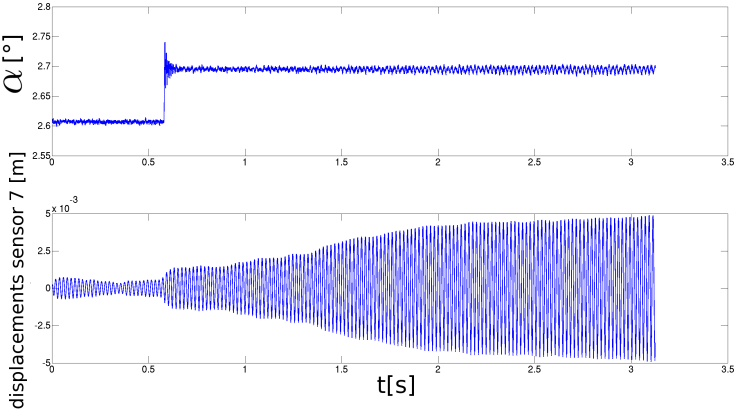

Figure 5.3.: Example for stability boundary searching via angle of attack adjustment (A.1, M_c)

After the initial oscillation built-up, there was a smooth transition into the limit-cycle amplitude recorded. Figure 5.4 shows pictures from videos which have been shot during the experiments. For two different Mach numbers the pictures show the final LCO amplitude.

It can be observed that the amplitude depends strongly on the flow parameters. For the lower Mach number Ma=0.8646 the amplitude at the wing tip is approximately 1 cm, while for the larger Mach number Ma=0.8793 the amplitude is roughly 0.4 cm. The LCO frequency is more or less constant at approximately 50Hz.

(a) Ma=0.8646 (b) Ma=0.8793

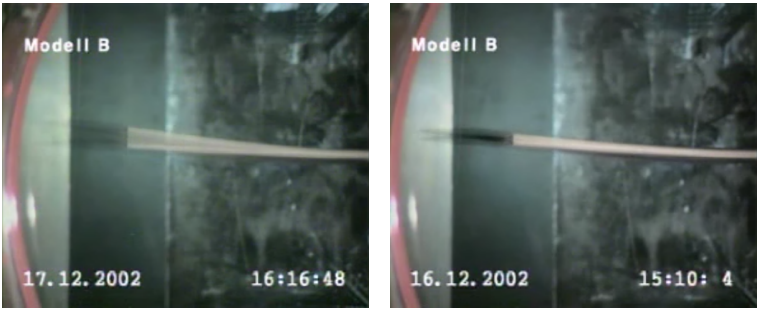

Figure 5.4.: Shots from experimental video material, Re = $1.69 \cdot 10^6$, angle of attack $\alpha = 2.69°$ (Appendix A.1, M_c, M_f)

The geometry used for the computational aerodynamic models has been generated from measurements with an optical 3D method.

5.1.1. Analysis and Comparison to Simulation

To compare LCO amplitudes the acceleration sensor signals are integrated with trapeze integration. Hence the noisy acceleration signals are smoothed within the two integration steps to get the displacement signals.

The main goal of the experiment was the measurement of pressures, steady but also unsteady. In the following chapters the comparison of unsteady pressures is done with the pressure transfer function

$$\widehat{cp} = \frac{\mathcal{F}(cp(t))}{\mathcal{F}\left(dz_{\text{sensor\_6}}(t)\right)} \ . \tag{5.1}$$

$\mathcal{F}(\cdot)$ represents again the Fourier transformation. The output value of the transfer function is the pressure coefficient cp and the input value is the displacement of the integrated acceleration sensor 6

signal. Concerning experimental values, several measured periods are used to compute the transfer function. $\widehat{cp}$ is here presented as the zero-harmonic, mean value cp_{mean}, and the complex valued first harmonic, illustrated in the upcoming plots in magnitude cp_{mag} and phase cp_{phase}.

5.1.2. Measurement Accuracy

The pressure sensors have been calibrated before every measurement campaign. The sensor data itself has shown a very low standard deviation of about $\sigma = 0.07$ %. But the overall accuracy of the measurement depends mainly on the accurate measurement of all boundary conditions like Mach number and angle of attack. Mai (2012) has analysed the overall measurement error in more detail for a similarly equipped model in the same windtunnel. The analysis showed a precision / repeat accuracy of $0.8 - 1.9\%$.

The acceleration sensors could not be recalibrated before every measurement campaign. Hence, for the following comparisons the data of the pressure sensors is used to calibrate the displacement data of the integrated acceleration signal. For this purpose the lower side pressures of subsonic flow are used. The unsteady pressures at these subsonic and attached flow conditions can be predicted with large confidence with the applied methods. Accordingly, the unsteady pressure transfer functions can be used to calibrate the acceleration sensor data. This has led to a correction factor of $15.0\%-20.0\%$ for the displacement data.

5.2. FLIB Experiment

In 2011 the AEROSTABIL wing has been used in the DLR project 'iGreen' for another experiment in the DNW-TWG, see Mai et al. (2011). In this experiment called FLIB ("Flügel Interferenz mit Böen und Buffet") the influence of a gust on the passive AEROSTABIL wing, which is created by an upstream pitching NACA-0010 profiled rectangular wing, was measured. To determine the deflections of the AEROSTABIL wing as a result of aerodynamic loads, a marker-based deformation measurement system was used. The markers were distributed on the upper side of the wing as sketched

in Figure 5.5.

Since first numerical studies by Stickan et al. (2010) revealed cross-section deformations of the AEROSTABIL wing, two chordwise marker rows were applied to verify and quantify these deformations in the scope of the FLIB experiment.

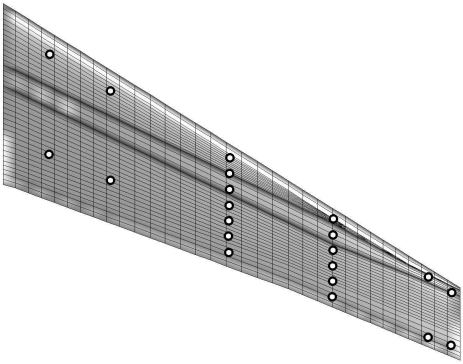

Figure 5.5.: Gust response experiment: positions of marker for optical measurement system

The generalized damping values in table 6.1, which are used for the following studies, have also been measured during this experimental campaign in a ground vibration test (GVT). Furthermore, the MAC (Modal Assurance Criterion) value comparisons in this table were derived from this GVT. The MAC value compares eigenmodes by computing the angle between the eigenvectors

$$\mathrm{MAC}(\boldsymbol{\phi}_1, \boldsymbol{\phi}_2) = \frac{|\boldsymbol{\phi}_1^T \boldsymbol{\phi}_2|^2}{\left(\phi_1^T \phi_1\right)\left(\phi_2^T \phi_2\right)} \quad . \tag{5.2}$$

Hence a value of 1 shows, except for a linear scaling factor, perfect agreement between the eigenmodes. The criterion is similar to the coherence function of time signals, which is also 1 for two linearly dependent signals.

6. Computational Modeling

The computational models for the aeroelastic simulations in the following chapters are described in this chapter. The modelling quality of the aerodynamic and structural model strongly influences the agreement of simulation and experiment.

6.1. Aerodynamics

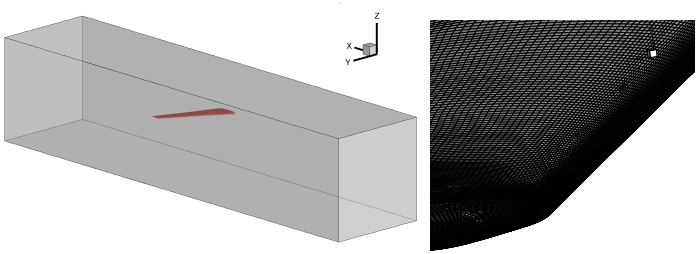

Figure 6.1.: Insight into the CFD-grid used for CFD-computations in Chapters 7.3, 8, 9.: left: overview of grid with adapted windtunnel walls, right - surface grid in tip region

The aerodynamic model for the RANS computations is mainly defined by the CFD-mesh and the selected turbulence model. If not stated differently, the Menter SST turbulence model as introduced in Section 3.1.1 is used. Further CFD solver parameter can be found in Appendix A.7.

The mainly employed CFD mesh for the AEROSTABIL investigation, e.g. also for the publication Stickan et al. (2014), is created by the Solar mesh generator. The mesh includes windtunnel walls as visible in Figure 6.1. It has 11.5 million nodes, 5.2 million hexahedrons, 37.4 million tetrahedrons and small numbers of prisms

and pyramids. The wing and the windtunnel walls are modelled as viscous walls. The length of the windtunnel is adjusted to fit a measured boundary layer thickness. The distance from wing root leading edge to the inlet plane is 2.5 meters and to the outflow plane 2.0 meters.

For different angles of attack the CFD mesh is not recreated. Instead the mesh is adopted via mesh deformation. In similar manner also the upper and lower windtunnel wall is adjusted to the experimental wall adoption values.

For Chapters 8 and 9 the inflow/outflow planes have been modelled with the far-field boundary condition of the CFD solver TAU. The reference case Chapter 10 uses boundary conditions that are easier to reproduce, by defining the inflow speed as well as the inflow and outflow pressure.

6.1.1. CFD Mesh Convergence Studies

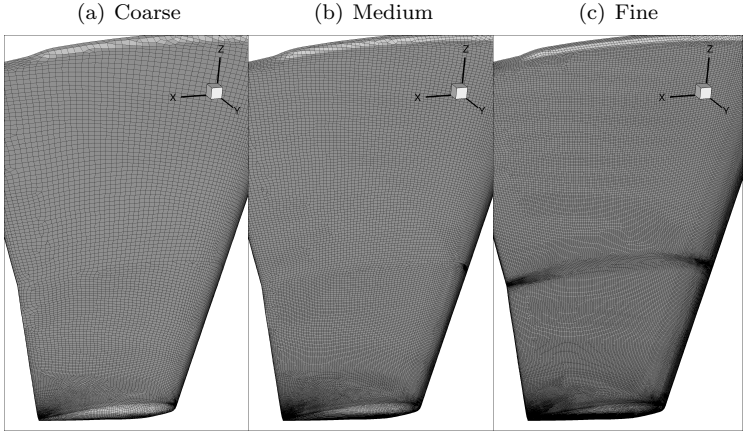

Figure 6.2.: CFD meshes for mesh convergence study: Coarse mesh with 3.8 million nodes, medium mesh with 11.5 million nodes, fine mesh with 23 million nodes

For CFD mesh convergence studies three meshes have been created with Solar, see Figure 6.2 and Figure 6.3. Starting point as

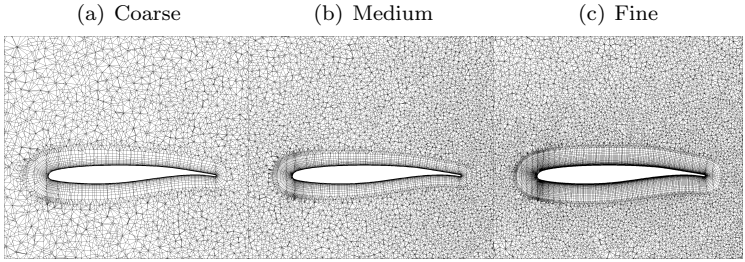

Figure 6.3.: CFD meshes for mesh convergence study: volume cuts at y=0.5m

medium mesh is the main mesh used in Stickan et al. (2014). To create the coarse mesh the source spacing has been increased by a factor 1.5, for the fine mesh the spacing has been reduced by a factor 0.66. The meshes consist of 3.8 million, 11.5 million and 23.0 million nodes, respectively. The refinement of the fine mesh has been restricted to the closer wing-surrounding area to reduce the computational effort. This step has been verified by steady computations with the original 42 million node mesh without this restriction.

6.2. Structure

Beam Model

"The reduced structural representation of an aircraft wing as a beam is typically a well-approved and frequently used method to perform static or dynamic deformation calculations. Important assumptions arising from *Bernoulli's* beam theory have to be met when applying NASTRAN beam finite elements:

- prerequisite of preservation of cross-sectional shape
- shear rigidity
- slenderness of the structure

Due to the large aspect ratio of the AEROSTABIL wing, the latter assumption is fulfilled. "(Stickan et al. (2010))

Starting point of the AEROSTABIL investigations is the finite element model shown in Figure 6.4. Is consists of 100 CBEAM and lumped masses elements. Leading and trailing edges are attached to the beam for deformation visualisation. The beam element parameters are adjusted to dynamic and static measurements.

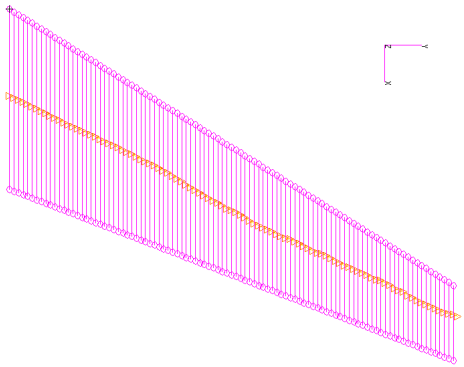

Figure 6.4.: Beam FEM including rigid body elements for mode visualisation at leading and trailing edge

Shell Model

Usually wing structures include ribs in chord-wise direction to preserve the aerodynamic profiles. But the AEROSTABIL model lacks such ribs. Therefore the assumption of rigid airfoil under aerodynamic loading has been reviewed with a shell FE-model.

The shell FE-model has been generated with the FE-model generator *ModGen*, see Klimmek (2009). This parametric model generator allows building up a structural model using the exact input geometry of structural components like skins and spars. The construction plan of the model provided the overall structural design properties.

The AEROSTABIL model is mainly build up by carbon/glass fibre reinforced plastics. Stickan et al. (2010): "A laminate stacking in NASTRAN is modelled with `MAT8` cards, defining single layer orthotropic material data, and `PCOMP` cards, providing the stacking sequence, along with fibre angle and layer thickness. The AEROSTA-

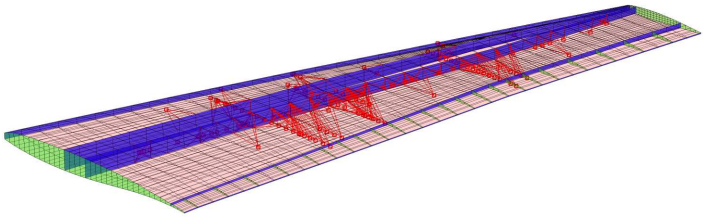

Figure 6.5.: Parameterised geometry model

BIL layer scheme consists of unidirectional layers and woven fabrics. Degradation of the E-modulus in a woven fabric (modelled as two separate layers) was accounted for by a reduction of the theoretical value of 15%, and 5% reduction in case of unidirectional layers.

Fig. 6.5 shows the geometry model of the AEROSTABIL wing with the top skin removed, as resulting from *ModGen*. In order to simulate a gluing area at the acute trailing edge, dummy ribs were introduced to connect upper and lower skin in the rear area."..." Mass is incorporated as material density for the structural parts and as concentrated masses (`CONM2`) connected to the structure with `RBE3` interface elements, representing the measuring equipment (pressure sensors, accelerometers, wiring).

The AEROSTABIL model is clamped at the root via a plane bracket, extending approximately from $x = 2.0$ to 18.5 cm, measured from the nose. The clamping was simulated by means of a `RBE2` element and torsional springs in the centre point of this rigid body element, representing non-rigid clamping conditions. The springs were aligned with a local coordinate system, pointing in the direction of the spar, and adjusted in their stiffness values in order to approximate as close as possible the first bending, in-plane, and torsion frequency Dietz et al. (2003)."

Fig. 6.6 shows the FE-model modes 1 (1. bending, 40.04 Hz), 4 (1. torsion, 247.2 Hz), 7 (437.0 Hz), and 11 (579.2 Hz). These modes show already for relatively low frequencies local chord-wise deformations between the main spar and the trailing edge. This underlines the need for a shell FE-model instead of a simplified beam model.

Comparison to ground vibration test data can be found in Table

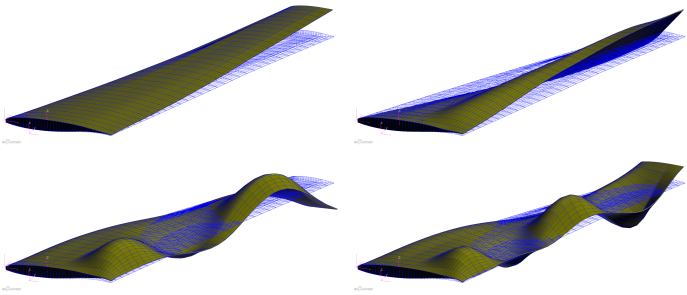

Figure 6.6.: Mode 1, 4, 7, 11 (left to right, top to bottom)

6.1. Eigenfrequencies and MAC values for the first bending, torsion and in-plane mode show only a reasonable agreement to the measured data. Differences in the eigenfrequencies are up to 8.9 percent, MAC value for in-plane mode is only 78.4 percent. But without deviating significantly from the underlying layup scheme, a better agreement could not be reached. Since the agreement to static experimental values is relatively good, the model is seen as sufficiently accurate for the following investigations.

	f_{exp} [Hz]	f_{FEM} [Hz]	$\frac{f_{exp}-f_{FEM}}{f_{exp}}$ [%]	MAC[%]	ζ[%]
1^{st} bending	37.22	40.43	8.6	96.6	0.70
1^{st} in-plane	118.83	123.49	3.9	78.4	0.84
1^{st} torsion	271.24	247.16	-8.9	81.7	0.99

Table 6.1.: Comparison structural shell model (FEM) and measurements (exp): $f_.$ - eigenfrequency, ζ - Lehr's damping ratio, modal damping $d_i = \zeta \cdot 2\pi f_{exp}$

7. Steady Fluid-Structure Interaction Analysis

The starting point for the AEROSTABIL flutter and LCO investigations is the analysis at static conditions. The 2D investigations in Chapter 4, especially Section 4.2, have shown the strong influence of the steady flow field on the unsteady air forces. Thus a good agreement of steady experiments and simulations must be shown before starting the unsteady investigations. From the very first rigid computations without aero-structure interaction are excluded from the investigations due to the high flexibility of the model. The used methods for the static CFD-CSM computations have been described in Section 3.6.1.

At the beginning Section 7.1 reveals the very significant influence of the structural shell model presented in Section 6.2. These results are validated in Section 7.2 with wing deformation measurements. In Section 7.3 the focus shifts to limit cycle flow conditions. Section 7.3.1 deals with the selection of an appropriate turbulence model for the limit-cycle flow conditions. Afterwards another influencing factor of steady aeroelasticity is shown in Section 7.3.2 by applying a nonlinear structural model. Finally in Section 7.3.3 the influence of the employed CFD meshes is discussed.

In this chapter the flow conditions are defined by the Mach number Ma and the Reynolds number Re, which is defined with the reference length $c_{ref} = 0.183m$. A complete definition for each case is given in Appendix A.1.

For all cases, the experimental static pressure is the mean pressure during a valid time history. This means that shocks might get blurred out slightly for limit-cycle cases with larger amplitudes. All computational data is computed in steady mode.

A modal structural model is used for most of the investigations. The number of used eigenmodes (n_{modes}=200) has been increased until the steady pressure were converged to the linear solution of a

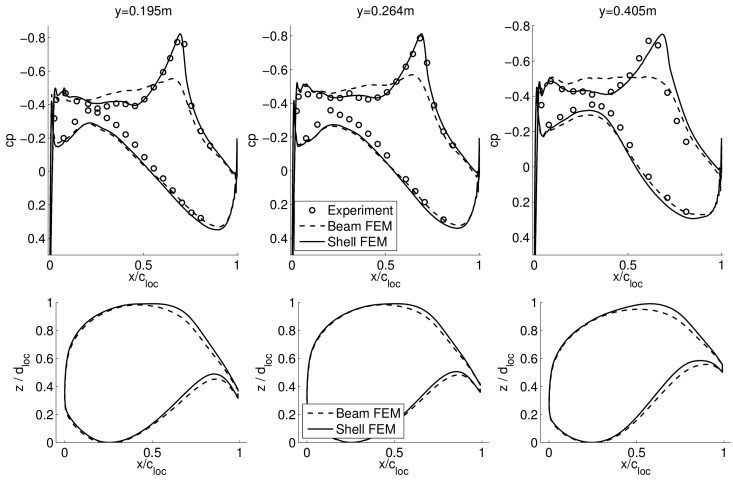

Figure 7.1.: Comparison beam FE-model and shell FE-model results for Ma = 0.819, Re = $1.33 \cdot 10^6$ and $\alpha = 0.0°$ (A.1, S_a): Upper plots - pressure coefficient for the 3 measurement sections, lower plots - airfoils of these sections normalized by profile thickness (shifted onto each other for comparison), (Already published in Stickan et al. (2014))

direct call of the structural solver.

The results of Section 7.1 to 7.3.1 have already been published in Stickan et al. (2014); reused passages are marked accordingly with "...".

7.1. Comparison Structural Beam vs. Shell Modelling

The beam and shell FE-model from Section 6.2 are used to compare the influence of structural modelling of different fidelity. The here discussed transonic test case is defined by the Mach number Ma = 0.819, Reynolds number Re = $1.33 \cdot 10^6$ and an angle of attack of $\alpha = 0.0°$. The computations have been executed with the Menter

SST turbulence model.

"For the simulation a CFD-mesh with 4.5 million nodes is used. The upper and lower windtunnel are not modelled and instead set to non-reflecting farfield boundary conditions, while the wall, to which the wing is attached, is set to viscous boundary condition. This is essential to achieve a correct boundary layer thickness at the wing position, which has been compared to windtunnel measurements. The opposite wall is defined as slip condition. All CFD-grids use a fixed transition at 7.5 percent chord length, corresponding to the experimental transition triggering.

The upper plots in Figure 7.1 show the pressure coefficients for the three measurement sections. While the agreement of measurement and beam model results is not satisfying, it is shown that a good agreement can be achieved by applying the shell model. The reason for this behaviour can be found in the deformation of the wing cross sections, see lower plot in Figure 7.1. It shows that the shell model predicts a bulge on the upper side of the wing, superimposed with an airfoil bending close to the trailing edge. This cambering effect generates a flow acceleration, which explains the strong pressure decrement upstream of the shock. Naturally this phenomenon can only be captured by the shell model and shows the importance of a detailed structural model for the AEROSTABIL wing."

The elastic cambering $\mathbf{dz}_{\mathrm{Camber}}$ of an airfoil can be described by removing torsional and translational parts from the aerodynamic surface displacements $\mathbf{dx_a}$ in z-direction (z pointing upwards, perpendicular to planar wing layout). Therefore, two reference points are used to define $\mathbf{dz}_{\mathrm{Camber,Ref}} = \mathbf{0}$ for each cut. In the case of Figure 7.2 the leading and trailing edge is used. The plot shows the elastic cambering for hundreds of profiles of the wing upper side. One can recognize the cambering behind the main spar over almost the complete wing span.

7.2. Comparison to Deformation Measurements

In Section 5.2 another experiment using the AEROSTABIL wing is described. The deformation measurements from the experiment are compared to computational data in this section. Therefore static

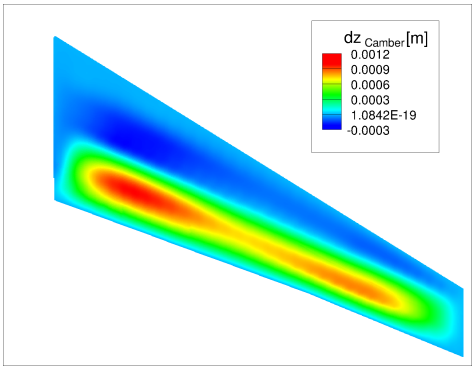

Figure 7.2.: Cambering upper surface for Ma = 0.819, Reynolds number Re = $1.33 \cdot 10^6$ (A.1, S_a)

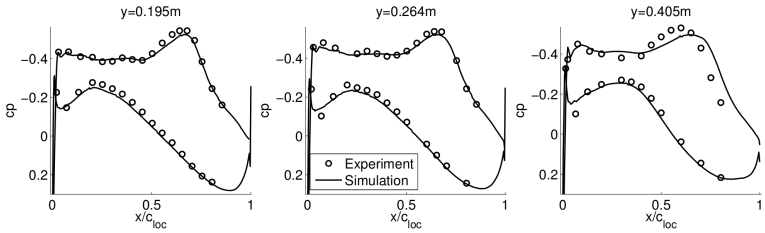

Figure 7.3.: Comparison of pressures, $Ma = 0.75$, $Re = 1.38e6$, $\alpha = 0.0°$ (A.1, F_a)

simulation results of Neumann and Mai (2013), which employ the same structural model and fluid-structure interaction methodology, are used to compare the cross-sectional deformation measurements to numerical data. The flow conditions are defined by: Ma = 0.75, Re = $1.38 \cdot 10^6$, AEROSTABIL angle of attack $\alpha_{AS} = 0.0°$. The angle of attack of the NACA gust generator is set to $\alpha_{\text{NACA}} = 0.0°$ to minimize the influence to the AEROSTABIl measurement.

Figure 7.3 compares the measured and computed pressures for the selected case. A good agreement between experiment and simulation can be found. Most importantly, Figure 7.4 compares the predicted airfoil deformation/cambering with the measured deformation. It can be observed that the predicted deformation is in good agreement

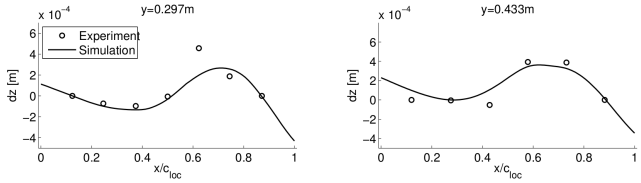

Figure 7.4.: Airfoil deformation dz for steady gust response setting, see Figure 7.3 (A.1, F_a): first and last measured point in each cut used as $dz = 0$ reference to compare experiment and simulation, theoretical noise measurement error up to $3 \cdot 10^{-4}$ m (Already published in Stickan et al. (2014))

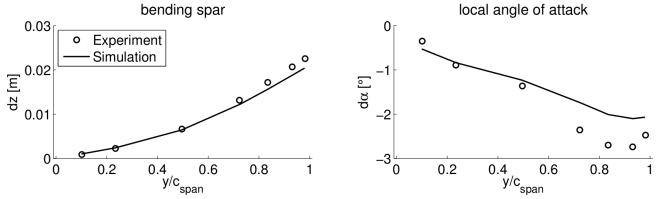

Figure 7.5.: Comparison of bending and local angle of attack , $Ma = 0.75$, $Re = 1.38e6$, $\alpha = 0.0°$ (A.1, F_a), theoretical noise measurement error in twist pprox. 0.5 degree

with the experimental data.

Finally Figure 7.5 compares the bending and the local angle of attack as torsion equivalent between experiment and simulation. In this plot a good agreement can be found in bending. However, the twist result shows less agreement which might be attributed to two reasons: The theoretical noise in the marker displacement data can be up to 0.3mm. Since the twist is computed geometrically from the displacements the noise error can be up to 0.5 degree. Secondly the profile cambering in Figure 7.4 shows the difficulty of measuring twist via surface measurements (which has been performed equivalently for the computational results). A wrong amplitude or position of the cambering bump in the simulation does also influence the twist result significantly.

Overall the airfoil deformation, which is essential for accurate sim-

ulation results in the transonic regime, could be verified with the additional experimental data. The magnitude of computed cambering agrees well with the measured data. Hence the quality of the structural model is further validated.

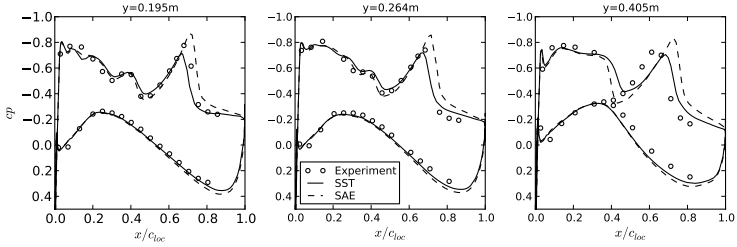

Figure 7.6.: Pressure coefficients for mean LCO state, static simulation: Ma = 0.8646, Re = $1.69 \cdot 10^6$ and $\alpha = 2.69°$ (A.1, M_c), comparison of turbulence models: Menter SST (SST) and Spalart-Allmaras with Edwards' modification (SAE) (Already published in Stickan et al. (2014))

7.3. Limit-Cycle Flow Conditions

7.3.1. Turbulence Modelling

"After validating the simulation setup for two different relatively mild experimental settings, the focus is now changed to limit-cycle flow conditions. From the parameter range in which LCOs could be identified experimentally, one point with relatively large oscillation amplitude is selected. The addressed LCO-state is Ma = 0.8646, Re = $1.69 \cdot 10^6$ and $\alpha = 2.69°$. This paragraph outlines the sensitivity to turbulence modelling at this flow state.

The applied CFD-mesh models all windtunnel walls with viscous boundary conditions. This should ensure that for the upcoming unsteady computations, for which the same grid is used, windtunnel wall interferences are not compromising the results, see findings from Voss (1998). The upper and lower walls are adapted to the experimental settings. The mesh contains 11.5 million nodes. An overview of the mesh is given in Figure 6.1.

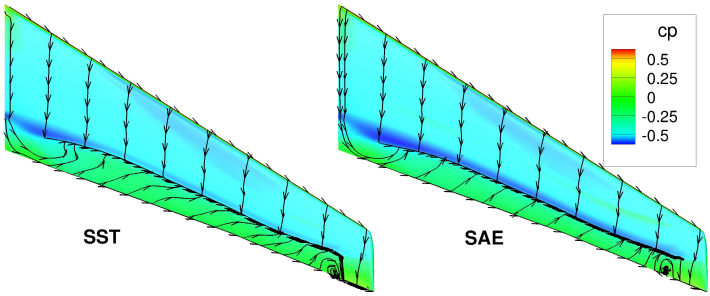

Figure 7.7.: Surface pressure and skin friction lines for LCO state, static simulation: Ma = 0.8646, Re = $1.69 \cdot 10^6$ and $\alpha = 2.69°$ (A.1, M_c), comparison of turbulence models: Menter SST (SST) and Spalart-Allmaras with Edwards' modification (SAE) (Already published in Stickan et al. (2014))

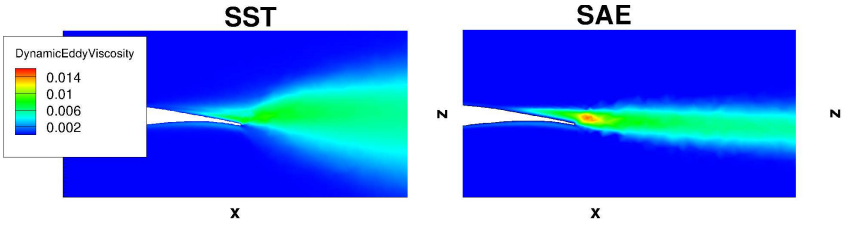

Figure 7.8.: Dynamic eddy viscosity in volumetric aerodynamic solution at y = 0.3m for LCO state, static simulation: Ma = 0.8646, Re = $1.69 \cdot 10^6$, $q_\infty = 20.7kPa$, and $\alpha = 2.69°$ (A.1, M_c), comparison of turbulence models: Menter SST (SST) and Spalart-Allmaras with Edwards' modification (SAE) (Already published in Stickan et al. (2014))

Figure 7.6 presents the steady simulation results for the Menter SST model (SST) and the Spalart-Allmaras model with Edwards' modification (SAE)." The displayed experimental data are the mean measured pressures of the oscillating experimental conditions. In contrary the simulations have been performed without time dependence. It has been validated that the aerodynamic model shows no unsteady effects for a rigid geometry. Hence, static CFD-CSM results as in the previous sections are adequate to compare to the mean measured values.

"The pressure plots reveal a complex double-shock system. It can be observed that the SST and SAE pressure coefficients results differ strongly on the upper side. SAE shows stronger pressure decay upstream of the second shock and produces too much lift downstream.

Figure 7.7 shows skin friction lines for the two turbulence models. It can be observed that both models predict a similar separation bubble downstream of the second shock. The separation is not only shock-induced, but at least partially triggered by the strong profile curvature due to the camber bending.

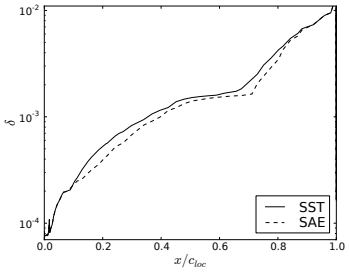

Figure 7.9.: Boundary layer thickness at $y = 0.3$m for LCO state, static simulation: Ma $= 0.8646$, Re $= 1.69 \cdot 10^6$, $q_\infty = 20.7kPa$, and $\alpha = 2.69°$ (A.1, M_c), comparison of turbulence models: Menter SST (SST) and Spalart-Allmaras with Edwards' modification (SAE) (Already published in Stickan et al. (2014))

Figure 7.8 displays a cut through the volumetric aerodynamic solution. It shows the dynamic eddy viscosity at $y = 0.3\,m$. One can

observe different solutions for the dynamic eddy viscosity for both turbulence models. The SST model shows a strong downstream expansion of an area of increased eddy viscosity. The expansion of the SAE model is not very strong, but shows a significant maximum in the centre of the separation bubble.

Figure 7.9 shows a comparison of the boundary layer thicknesses at $y = 0.3\ m$. It can be observed that the SST model shows a slightly thicker boundary layer upstream of the second shock. The plot shows also the further downstream shock position of the second shock for the SAE model.

To summarize: The main difference of the two turbulence models is the different shock position of the main shock. Due to the camber bending this shock is located in a strongly curved part of the airfoil, which leads to a flow acceleration and pressure decrease. Therefore the shock position has a strong influence on the overall lift of the wing."

7.3.2. Nonlinear Structure

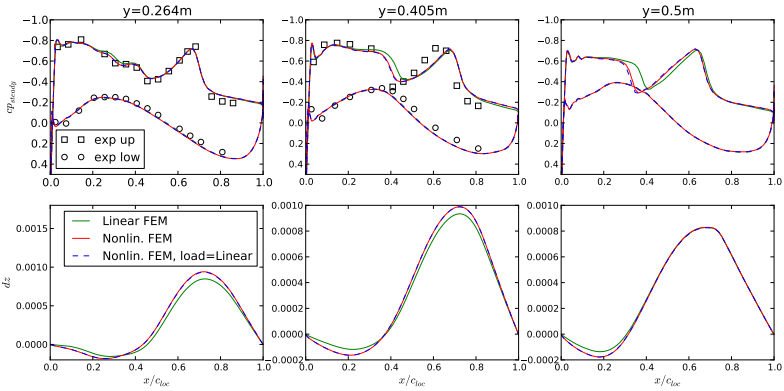

Figure 7.10.: Nonlinear FEM, static pressures and cambering (upper side), Ma = 0.8646, Re = $1.69{\cdot}10^6$, $q_\infty = 20.7kPa$, $\alpha = 2.69°$ (A.1, M_c)

In this section it is investigated if nonlinear structural modelling has significant influence on the steady pressures. Therefore the same

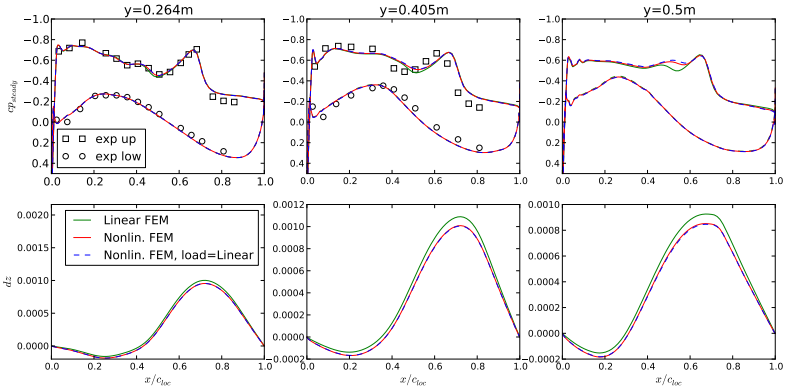

Figure 7.11.: Nonlinear FEM, static pressures and cambering(upper side), Ma $= 0.8793$, Re $= 1.69 \cdot 10^6$, $q_\infty = 20.9kPa$, $\alpha = 2.69°$ (A.1, M_c)

structural model as used above is used with NASTRANs nonlinear solution sequence 400, see Section 3.3.4. The results of the nonlinear structural solution sequence were verified in terms of solution parameters like number of iterations. Follower forces did not show a significant influence on the structural result.

Figure 7.10 and 7.11 show pressure and cambering results for two different Mach numbers, $Ma \in \{0.8646, 0.8793\}$. The solutions have been computed with a linear structural model and nonlinear structural model. Additionally the result of the nonlinear FEM with linear CFD-CSM loop loads is plotted. This result shows that the shock position is more sensitive to the linear or nonlinear deformation than to the overall CFD-CSM loop.

Both figures show that the structural nonlinear solution has small but well visible influence on the aerodynamic solution. For $Ma = 0.8646$ Figure 7.10 shows in the outer cuts an upstream shock position movement compared to the linear solution while for $Ma = 0.8793$. Figure 7.11 shows mainly in the outer cut small changes in the upper side pressures. Here the first transonic shock seems to be slightly weaker. The reason for the differences in the results can be found in the according cambering plots in the same figures below. The nonlinear solution sequence shows slightly different cambering

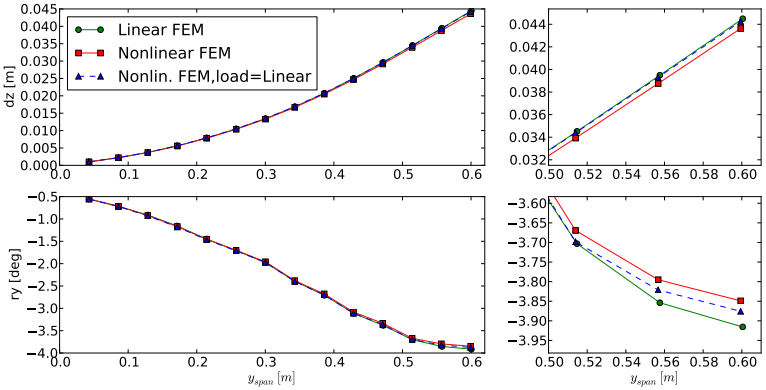

Figure 7.12.: Nonlinear FEM, bend and twist, Ma = 0.8646, $\mathrm{Re} = 1.69 \cdot 10^6$, $q_\infty = 20.7kPa$, $\alpha = 2.69°$ (A.1, M_c)

lines. The nonlinear result with linear CFD-CSM loads confirms the effect.

Figure 7.12 shows the twist and bend outcome for the lower Mach number $Ma = 0.8646$. The differences between linear and nonlinear solution are only very small. Important to note here is that the bending result and the twist up to y_{span}=0.5m of the linear and nonlinear solution with linear result loads agree very well. But since the last mentioned solution is already showing the differences in the pressure result for the section at y =0.405m in Figure 7.10, this result indicates additionally that the changed cambering of the nonlinear solution sequence is the reason for the change in pressure.

7.3.3. CFD Mesh Convergence

Mesh convergence is an important requirement for numerical studies. Therefore the three CFD meshes shown in Section 6.1.1 are used to compare steady pressures in the two outer measurement sections. Furthermore, the section at $y = 0.5m$ is included due to its importance for the following unsteady studies. Important to note here is that the CFD mesh convergence is not studied for a rigid geometry, but instead the complete static CFD-CSM loop has been considered. So the following comparisons show the combined

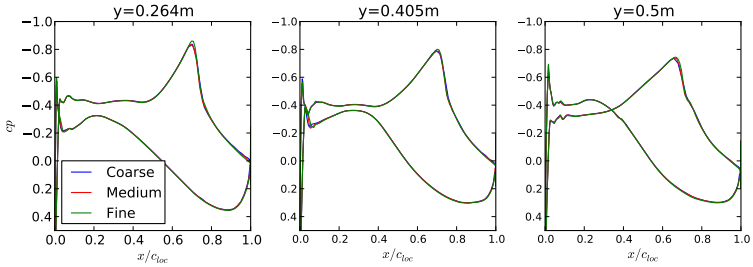

Figure 7.13.: Grid convergence Mach number Ma = 0.819, Reynolds number Re = $1.33 \cdot 10^6$, angle of attack $\alpha = 0.0°$ (A.1, S_a)

effect of aerodynamic mesh density and its impact on the structural deformation.

Figure 7.13 shows results for $Ma = 0.82$ and $\alpha = 0°$. This transonic flow case with only local and marginal separation shows very good agreement between the three meshes.

Figure 7.14 and 7.15 show results at or very close to limit cycle flow conditions ($Ma = 0.8646$ and $Ma = 0.8844$). The flow features, which have already been shown in Figure 7.7, include a very strong separation on the complete wing and two transonic shocks. For such demanding flow features also CFD mesh convergence is more difficult to reach. Especially for the outer section at $y = 0.5m$ differences are visible.

For the smaller Mach number $Ma = 0.8646$ the coarse and medium mesh agree well, while the fine mesh shows a more upstream first shock at the outer section. For the higher Mach number the shock at the outer section is further downstream. Therefore mesh convergence cannot be shown very well, but is acceptable for these specific flow conditions.

7.4. Quasi-Steady Analysis

A first step towards unsteady investigations is the analysis of the lift curve slope $\partial C_{\text{lift}}/\partial\alpha$ for a range of Mach numbers at constant angle of attack α from the experiment. The maximum of the lift curve

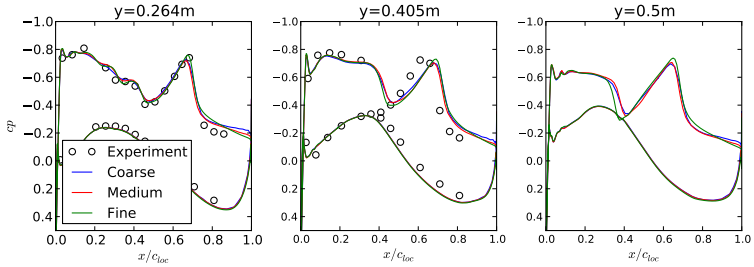

Figure 7.14.: Grid convergence Ma = 0.8646, Re = $1.69 \cdot 10^6$, $q_\infty = 20.7kPa$, $\alpha = 2.69°$ (A.1, M_c)

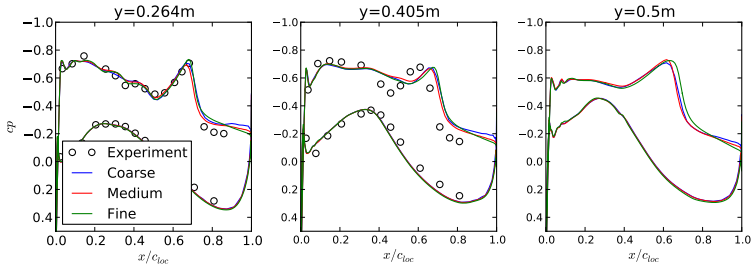

Figure 7.15.: Grid convergence Ma = 0.8844, Re = $1.69 \cdot 10^6$, $q_\infty = 20.96kPa$ $\alpha = 2.69°$ (A.1, M_g)

slope should identify the so called critical Mach number, or in other words, the location of the transonic dip as seen in Figure 1.2. In principle the aerodynamic answer of a pitch-motion for a frequency $k = 0$ is computed, showing the Mach number for which a small disturbance to the aerodynamic setting produces the largest effect on the lift coefficient. The criterion is discussed by Bendiksen (2003) in more detail, focusing on the fundamental role of the transonic shock. Another example for the application of this criterion is given in flutter investigations by Voss and Thormann (2012).

The results for $\partial C_{\text{lift}}/\partial\alpha$ are computed via finite differences of two steady CFD-CSM computations with angles of attack α_1 and α_2, where $\alpha_1 = \alpha$ and $\alpha_2 = \alpha + \delta\alpha$. The Menter SST model is used as turbulence model.

Figure 7.16 shows the resulting lift curve slope. The plot presents

as well the measured amplitude of sensor 6 for different limit-cycle experiments. Experience has shown that amplitudes smaller 1mm can be regarded as stable experimental settings, whereas larger amplitudes are considered unstable. The small amplitudes can be explained by aeroelastic response to windtunnel turbulence. Thus the experimental amplitudes show an unstable range approximately between $Ma = 0.86$ and $Ma = 0.88$. The maximum of the lift curve slope $\partial C_{\text{lift}}/\partial\alpha$ lies within this range; a first promising result for the unsteady investigations of the following chapters.

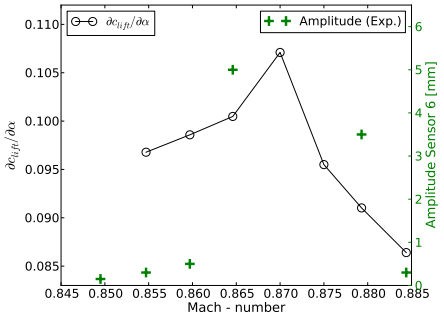

Figure 7.16.: Investigation of lift curve slope $\partial C_{\text{lift}}/\partial\alpha$ (A.1, $M_a - M_g$)

8. Dynamic Single Degree of Freedom Analysis

The dynamic investigations are started with a limitation to only a single degree of freedom (SDOF). This limitation is motivated by Dietz et al. (2003), who noticed a flutter/LCO mode dominated by the first bending mode for the AEROSTABIL experiment. The observation is made by comparing the bending mode to the LCO movie footage (see Figure 5.4) and the acceleration sensor signals. The sensor signals have shown also that the flutter mode is a real mode. This means no sensor has shown a phase lag, which increases the probability of a SDOF phenomenon.

The substitution of the first bending mode of a swept back wing by a 2D flow-parallel wing sections implies a combination of pitch and heave mode with upstream rotation point. Therefore, the LCO mechanism might be similar to the mechanism in the transonic 2D experiments by Dietz et al. (2006). These experiments with a supercritical NLR 7301 profiled 2D wing showed that the LCO mode combines heave and pitch to have a real SDOF flutter mode with a rotation point upstream of the wing section. Figure 8.1 illustrates the LCO motion for these experiments.

In Chapter 7 it is shown that the transonic flow conditions of the AEROSTABIL LCOs exhibit strong flow separation. These flow

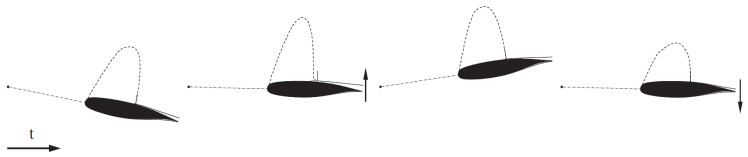

Figure 8.1.: Single degree of freedom 2D LCO mode sketch as combination of heave and pitch mode with rotation point upstream of wing section (from Dietz et al. (2006))

conditions could lead to unsteady flow effects without external excitation like shock buffet or a Kármán vortex street. But Dietz et al. (2003) excludes buffet as a possible source of wing excitation due to the low LCO frequency. Computational investigations did not show buffet either.

Accordingly, the publication Stickan et al. (2014) explains the AEROSTABIL LCOs by only using the first bending mode as dynamic single degree of freedom (SDOF) system. The highlights of this analysis and additional data are presented in this chapter.

Section 8.1 presents a flutter analysis, comparing also different turbulence models, while Section 8.2 presents LCO simulation results and their analysis.

Text passages used from Stickan et al. (2014) are again marked by "...".

8.1. Flutter Analysis

Single degree of freedom flutter is a seldom phenomenon. It requires unsteady aerodynamic forces which have a leading phase relative to the dynamic body movement; the phase difference must be between zero and 180 degree. A condition like this is unusual for an aviation configuration, but can be given consideration if the flow includes transonic aerodynamics and flow separation.

The unsteady aerodynamics for the flutter analysis are computed with the pulse-response method. Every computation produces the unsteady aerodynamic data for 11 reduced frequencies, $k = 0.05 \cdot i,\ i = 0, 1, .., 10$. An example plot for such a pulse computation can be viewed in Figure A.2.

In the computations below mainly the Menter SST turbulence model is used. Some results with the Spalart-Allmaras turbulence model with Edwards' modification are added for comparison.

It can be noticed that even for the experimentally stable Mach numbers (Ma $\in \{0.8547,\ 0.8597,\ 0.8844\}$) a low amplitude level was measured at acceleration sensors 6 and 7 in the right plot in Figure 7.16. These small amplitudes, which were caused by the background turbulence in the windtunnel, are sufficient to extract pressure transfer-functions by referring to the displacements of the acceleration sensors. "On account of this it is possible to compare

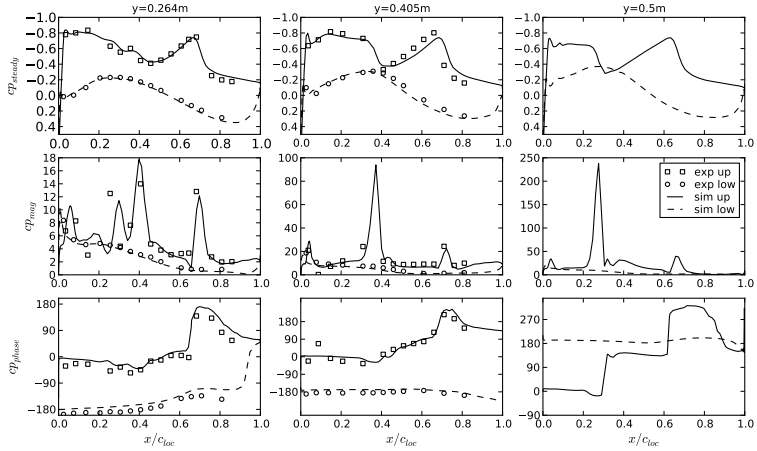

Figure 8.2.: Ma = 0.8547 (A.1, M_a): pressure coefficient transfer function with sensor 6 as input: first row - mean pressure, second row - first harmonic amplitude, third row - first harmonic phase (Published in Stickan et al. (2014))

the unsteady pressures transfer functions of experiment and simulation. For the measured points within the unstable range, measurements from an insignificantly smaller angle of attack are used. This $\Delta\alpha = -0.1°$ smaller angle has not shown an unstable behaviour in the experiment and is therefore also qualified to extract the linear unsteady pressures that necessarily can only be measured with small amplitudes (see Figure 5.3). Most important for this comparison is the agreement in the outer measurement section at $y = 0.405m$, since the aerodynamic forces acting on the outer part of the wing have a dominating impact on the generalized airloads of the first bending mode. For the same reason in this and the following chapters the first station at $y = 0.195m$ is replaced by a station at $y = 0.5m$. This allows to investigate the unsteady aerodynamics in the wing area with the largest influence on the overall excitation of the wing.

Figures 8.2 and 8.3 show the mean and first harmonic of the pressure transfer functions for the Mach numbers Ma $\in \{0.8547, 0.8646, 0.8844\}$. The plots show the similarity of the flow at all

(a) $Ma = 0.8646$

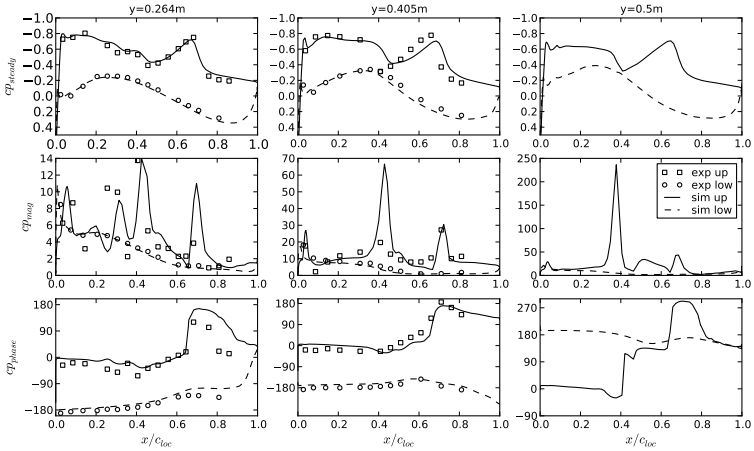

(b) $Ma = 0.8844$

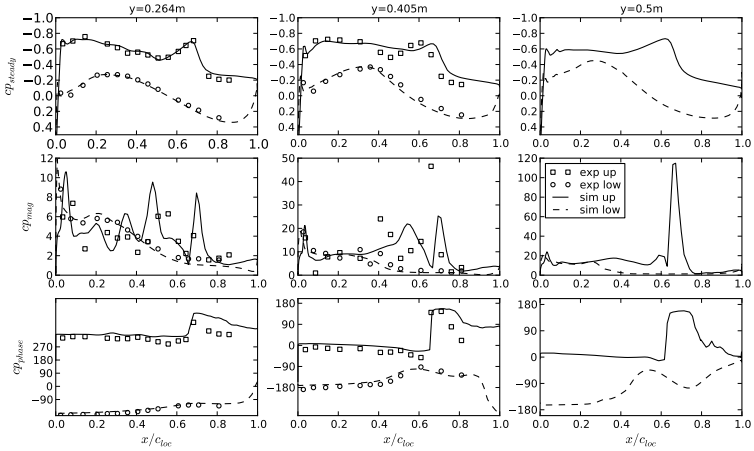

Figure 8.3.: Pressure coefficient transfer function with sensor 6 as input for two Mach numbers (A.1, M_c, M_g): first row - mean pressure, second row - first harmonic amplitude, third row - first harmonic phase (Published in Stickan et al. (2014))

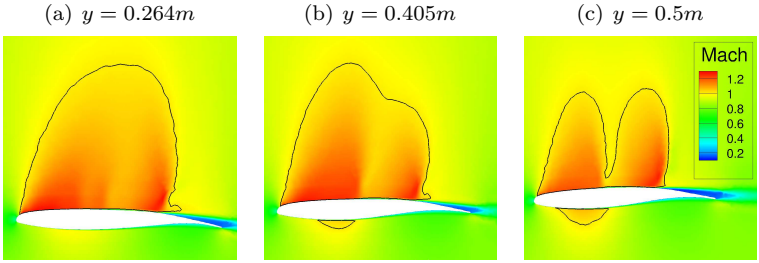

Figure 8.4.: Ma = 0.8646 (A.1, M_c): Mach number in CFD domain cut-plane at different constant y, contour line showing $\mathrm{Ma}_{loc} = 1.0$ (Already published in Stickan et al. (2014))

three Mach numbers: With exception of the outer station for the high Mach number $Ma = 0.8844$ all sections show a two shock system and a separation area behind the second shock. The first shock is getting weaker with increasing Mach number. At the outer station for $Ma = 0.8844$ it has vanished almost completely. For all sections the second shock shows the typical, approximately 180° phase shift.

The outer station at $y = 0.5m$ shows for the two lower Mach numbers $\mathrm{Ma} \in \{0.8547, 0.8646\}$ also a phase shift at the first shock position. This first shift is around 100°. The reason for the differing phase results at different positions can be observed in Figure 8.4, which shows volume cuts at the three discussed sections for the Mach number $Ma = 0.8646$. The plots show a supersonic flow above the boundary layer for the inner cuts at $y = 0.264m$ and $y = 0.405m$, while the outer cut at $y = 0.5m$ shows a subsonic area after the first shock. Although this area is not reaching down to the boundary layer, it generates the phase shift at the position of the first shock. Further analysis of the volumetric flow solution shows that the first shock is a weak, oblique shock while the second shock is strong."

For Mach number $Ma = 0.8646$ the generalized air forces (GAF) excited by the first bending mode are presented in Figure 8.5. The plot reveals a positive imaginary generalized air force for frequencies from zero up to approximately 60Hz. This means for such frequencies the aerodynamic forces lead to structural excitation. Neglecting structural damping and interaction with other eigenmodes, this plot

already reveals a possible self-excitation of the wing model for the LCO frequencies measured at approximately 50Hz.

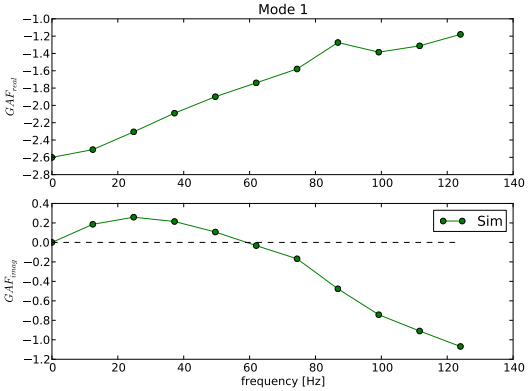

Figure 8.5.: Generalized Air Forces of first bending mode (GAF=$\widehat{A}_{1,1}$) for $Ma = 0.8646$ (A.1, M_c)

Finally, Figure 8.6 shows results of the flutter analysis by means of the p-k method (Section 3.6.4). Structural damping is defined according to Table 6.1. The damping results of the Menter SST model shows a classical transonic dip with a minimum for $Ma = 0.87$. The plot is also comparing the damping values to the experimental amplitudes. It can be observed that the unstable range visible for the SST model lies within the experimental unstable range, but the high Mach number bound of the simulation is lower than the experimental one. The minimal damping point occurs at the same Mach number as the maximum of the quasi-steady lift curve slope $\partial C_{\text{lift}}/\partial\alpha$ presented in Section 7.4.

The flutter results show also the damping results for the Spalart-Allmaras turbulence model with Edwards' modification (SAE). To allow a meaningful comparison, the SAE result has been computed for the identical angle attack and additionally (and usually more practice oriented) for the same lift as the SST computation. The same lift has been achieved by adjusting the wing angle of attack via the trimming method shown in Section 3.6.1. It can be observed that the minimum damping value for the SAE-model does not reach a negative value for any of the investigated Mach numbers. As

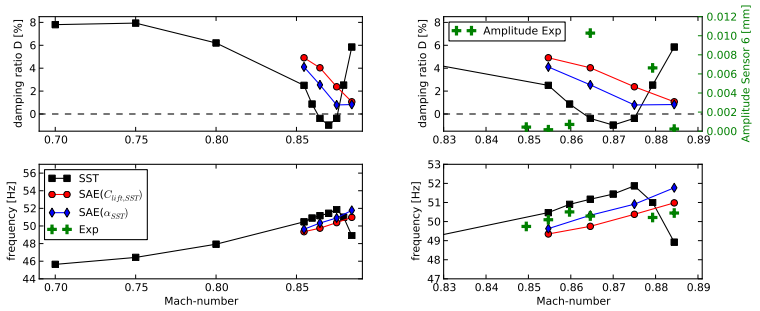

Figure 8.6.: Linear stability results (A.1, $M_a - M_g$): left - damping ratio and frequency over Mach-range for SST and SAE turbulence model, right - comparison of simulation results to experimental amplitudes and dominating frequencies, SAE results with C_{lift} or angle α being equal to SST result

already depicted in Section 7.3.1 the differences in static pressures at LCO flow conditions are relatively large. In this section it is shown that this discrepancy is significant for the stability features of the wing. Hence, as already seen for the 2D examples in Section 4.6, it is important to selected an appropriate turbulence model.

A similar conclusion has also been drawn by Iovnovich et al. (2015), who performed LCO computations on a clean-wing F16 fighter aircraft configuration. In this work the LCO phenomenon observed in the experiment can only be reproduced by the SSG/LRR Reynolds-Stress Model by Eisfeld (2004). In contrast to that, the SAE as well as the k TNT model by Kok (1999) fail in this respect. The application of the RSM model to the AEROSTABIL case is presented in Appendix A.3. The RSM shows quite similar results as the SST model. The damping is slightly increased and since the computational cost rise with the RSM model (7-equation turbulence model), SST is continued to be used.

The most important outcome of this section can be stated as follows: Since the damping plot shows a negative value for the SST model for the experimentally unstable Mach number $Ma = 0.8646$, a necessary requirement for a supercritical LCO is met. Therefore LCO investigations are performed in the following section.

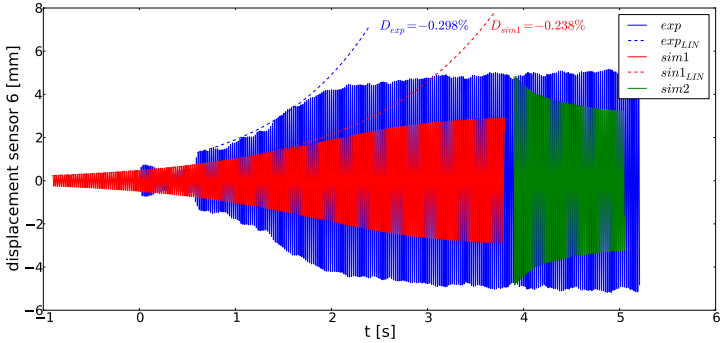

Figure 8.7.: LCO setting, $Ma = 0.8646$ (A.1, M_c), amplitudes in z-direction versus time of experiment and two different time-domain simulations: *sim1* - small start disturbance $\Delta\mathbf{q}_{1,1}$, sim2 - large start disturbance $\Delta\mathbf{q}_{1,2}$ in first generalized coordinate (Already published in Stickan et al. (2014))

8.2. Time-Domain LCO Analysis

The previous section 8.1 has revealed a negative damping for the Mach number $Ma = 0.8646$, Reynolds-number $Re = 1.69 \cdot 10^6$ and an angle of attack $\alpha = 2.69°$. For these conditions unsteady time domain computations are performed with the FSI-method presented in Section 3.6.2.

Again, the steady solution presented in Section 7.3 is used. According to the previous section only one structural dynamic degree of freedom is used, namely the first bending mode.

"The time-step size for the computations is defined in the manner that the first-bending mode is discretized with 60 time steps per period, assuming a reduced frequency of $k = 0.2$, which was the approximate flutter frequency in Section 8.1. LCO-amplitude convergence computations with 120 time steps per period proved that 60 steps per period are sufficient.

The results of two different computations are presented, one with a very small start disturbance $\Delta\mathbf{q}_{1,1}$ (*sim1*), one with a large start disturbance $\Delta\mathbf{q}_{1,2}$ (*sim2*). These start values are chosen to prove

the limitation of the LCO-amplitude. Figure 8.7 displays the amplitudes at the position of acceleration sensor 6 of the two simulations with the experimental values, see Figure 5.2. The plot also contains the theoretical amplitude curves with index LIN for a flutter case with amplitude independent (linear) aerodynamics. The curve of type

$$dz_i(t) = dz_{i,0} e^{-k_i \frac{v_\infty}{c_{ref}} \cdot D_i \cdot t}, \quad i \in \{exp, sim1\} \tag{8.1}$$

is used to estimate the damping ratio D_i via curve fitting. The reduced frequency k_i is the resulting frequency of the sensor 6 signal."

It can be observed that the limit-cycle amplitudes are in satisfying agreement with the experimental data. Furthermore, it confirms the amplitude limitation observed in the experiment. The simulated reduced frequency of the LCO is in very good agreement with the experiment, $k_{sim} = 0.204 \approx k_{exp} = 0.202$ ($f_{sim} = 50.79Hz \approx f_{exp} = 50.29Hz$). This result is surprising since the FEM-eigenmode differs 8.6 percent from the measured eigenfrequency. Simulation $sim1$ shows very well the linear aerodynamic character in the first seconds by following the theoretical amplitude curve. With increasing amplitude the behaviour fades out due to the nonlinear aerodynamics. The experimental damping ratios $D_{exp} = -0.298\%$ is smaller than the time-domain simulation result $D_{sim1} = -0.238\%$. However, it should be noted that the curve fitting procedure is not very accurate for the strongly fluctuating experimental amplitudes. Nevertheless this difference may explain the disagreement in the LCO amplitude.

"The start amplitude of the second computation is selected larger than the expected limit-cycle amplitude. During the simulation the amplitude decreases to reach almost the same state as simulation *sim1*.

Figure 8.8, left, shows the aerodynamic and structural damping work per cycle versus the square of the first bending mode amplitude $\mathbf{q}_{1,amp}\left(\widehat{t}\right)$. The aerodynamic work per cycle performed on the first bending mode, with an integration cycle starting at the moment of maximal amplitude $\widehat{t}$, is defined by

$$W_A(\widehat{t}) = \int_{\widehat{t}}^{\widehat{t}+\Delta T} \mathbf{Q}_1 \cdot \dot{\mathbf{q}}_1 \, dt \tag{8.2}$$

and the structural damping of the mode by

$$W_D(\widehat{t}) = \int_{\widehat{t}}^{\widehat{t}+\Delta T} 2d_1 \cdot \dot{\mathbf{q}}_1^2 \, dt \ . \tag{8.3}$$

$\mathbf{Q}_1$ is the generalized force, $\mathbf{Q}_1 = \mathbf{\Phi}_1^T \cdot \mathbf{f_s}$. Due to the linear damped system the structural damping work per cycle is a straight line. The aerodynamic work per cycle has a small curvature, which shows that the aerodynamic work per cycle is decreasing with increasing amplitude. As expected for the final LCO amplitude the aerodynamic work is equal to the damping work $W_A = -W_D$. Furthermore it can be observed that due to the small gradient of the difference between W_A and W_D the LCO-amplitude is very sensitive to the structural damping value.

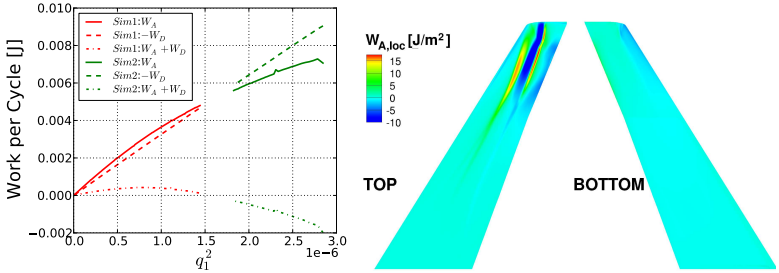

Figure 8.8.: left: global work per cycle, W_A - aerodynamic, W_D - structural damping, approximated for cycles starting at the moment of maximal amplitude, interpolated in between, right: local work per cycle at LCO state (Already published in Stickan et al. (2014)) (A.1, M_c)

The local aerodynamic work per cycle is plotted in Figure 8.8, right. The local work per cycle on CFD surface mesh cell location x_i is defined by

$$W_{A,loc}(x_i) = \int_{\widehat{t}}^{\widehat{t}+\Delta T} \frac{\mathbf{f_a}\,(x_i) \cdot \mathbf{\Phi}_a\,(x_i)}{A_{cell}(x_i)} \cdot \dot{\mathbf{q}}_1 \, dt \ . \tag{8.4}$$

$A_{cell}\,(x_i)$ is the surface-cell area of the cell at x_i, causing the local generalized force $f_a\,(x_i) \cdot \mathbf{\Phi}_a\,(x_i)$. The plot demonstrates that

mainly the shock movement in the outer wing segment is transporting energy into the wing structure.

The unsteady pressures on the upper model side of the linear aerodynamic simulation result of Figure 8.3 in Section 8.1 are compared to the nonlinear LCO simulation results, see Figure 8.9. Additionally in the third row $W_{A,loc}/q^2_{1,amp}$ is plotted, which is the local work per cycle normalized by the square of generalized coordinate amplitude. For the case of linear aerodynamics $W_{A,loc}/q^2_{1,amp}$ is computed by deriving

$$W_{A,loc}/q^2_{1,amp} = \pi \ \mathbf{f}_{a,mag} \cdot \mathbf{\Phi}_a \ \sin\left(\mathbf{f}_{a,phase}\right) \tag{8.5}$$

from Equation (8.4). Here the unsteady aerodynamic force transfer function $\widehat{\mathbf{f_a}}$, which is used in in magnitude $\mathbf{f}_{a,mag}$ and phase $\mathbf{f}_{a,phase}$, is defined by

$$\widehat{\mathbf{f_a}} = q_\infty \mathbf{\Phi}_{\text{z,sensor\_6}} \ \widehat{cp} \cdot \mathbf{n} \ , \tag{8.6}$$

whereas $\mathbf{n}$ is the surface normal and $\mathbf{\Phi}_{\text{z,,sensor\_6}}$ the value of the first bending mode at the position of sensor 6, which has been used to normalize the unsteady pressure transfer function $\widehat{cp}$ to allow comparison to experimentally measured pressures (See Equation (5.1)).

This plot shows locally the difference between linear and nonlinear aerodynamics and gives a reason for the global descent of the aerodynamic work per cycle. It can be observed that due to the small local mode amplitude the inner section at $y = 0.264m$ shows for the LCO-simulation the same unsteady aerodynamics as the linear simulation. The section at $y = 0.405m$ shows first signs of nonlinear aerodynamics by a less sharp first shock. This behaviour is more distinct for the station at $y = 0.5m$. It presents a flattened first shock amplitude and also differences in the phase result. All cuts show that the unsteady aerodynamics of the strong second shock are almost not influenced by the increased amplitude. The last row of Figure 8.9 shows directly the influence of the strong shock movements on the local work per cycle. As one can see the integral area resulting from the strong shock movement is smaller than the area belonging to the sharp, small amplitude shock motion."

Looking for the LCO trigger in the experimental pressures in Figure 8.9, one can compare the pre-LCO and LCO aerodynamics at the cut at y=0.405m. Also here the widening of the shocks can be seen slightly. In contrast to the simulations in this case the second

shock shows a more noticeable movement. However, the relatively coarse resolution of the measurements does not allow a conclusive interpretation.

At last Figure 8.10 shows cut planes through the volumetric flow solution and the corresponding surface pressure at $y = 0.5m$ at four different phase angles of the LCO cycle. The plots show a strong movement of the first shock over approximately 20 percent chord length. The strength of the shock is highest near the reversal point upstream and almost vanishes at the reversal point downstream. The plots show also that the second shock is relatively stable.

Investigations by Prananta et al. (2003), who performed LCO computations on an F16 fighter configuration, show strong shock movement combined with flow separation. Unfortunately, the investigation is focussed on verification of the aeroelastic simulation software and the aerodynamic LCO mechanism is not identified explicitly. However, the strong shock movement might be the LCO limiter as well.

In the context of the AEROSTABIL studies the SDOF analysis has shown that the LCO amplitude is limited due to the amplitude dependent, increasingly nonlinear shock motion.

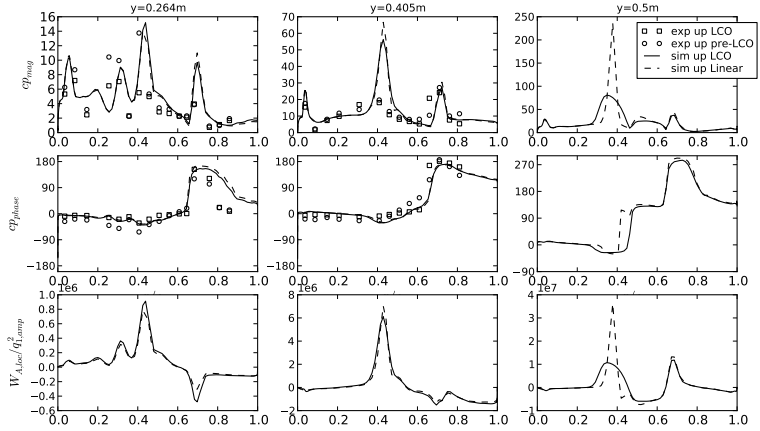

Figure 8.9.: Ma = 0.8646 (A.1, M_c), LCO-state and linear pre-LCO-state, upper side only: pressure coefficient transfer function with sensor 6 as input: first row - first harmonic amplitude, second row - first harmonic phase, third row - local work per cycle normalised with the square of the modal amplitude (Already published in Stickan et al. (2014))

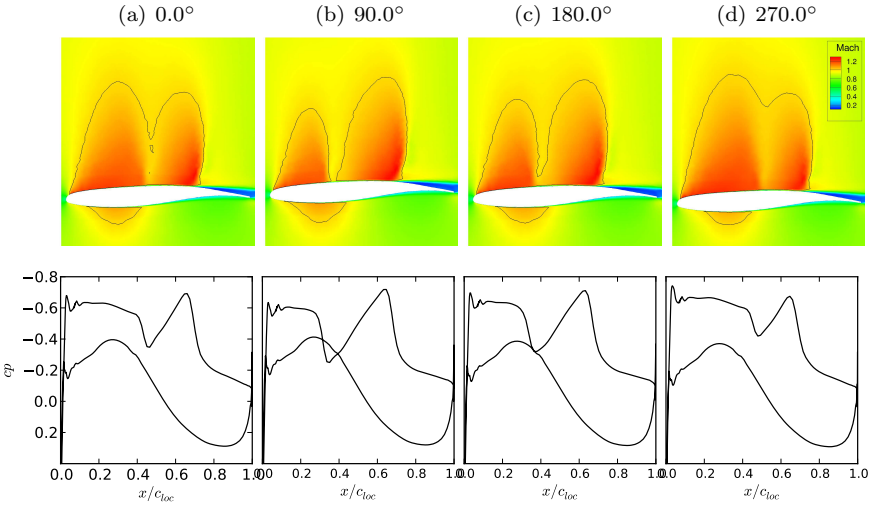

Figure 8.10.: Ma = 0.8646, LCO-state (A.1, M_c): Mach number field and surface pressure in cut-plane (y=0.5m) for different phase angles of the LCO cycle, contour line showing $\mathrm{Ma}_{loc} = 1.0$

9. Dynamic Multi Degree of Freedom Analysis

In the previous Chapter 8 the AEROSTABIL LCOs have been explained with only a single dynamic degree of freedom. However, the frequency-domain computations in Section 8.1 can reproduce negative damping only for one of the two unstable points observed in the experiment (within the parameter range covered). Hence, in this chapter the number of dynamic degrees of freedom is increased to overcome this discrepancy.

Similar to chapter 8 the frequency-domain analysis in Section 9.1 is followed by time domain LCO analysis in Section 9.2. Finally, some studies are presented in Section 9.3, showing the influence of unsteady cambering and the angle of attack.

9.1. Flutter Analysis

The frequency-domain flutter analysis in Sections 9.1.1 to 9.1.3 is again mainly performed for the Mach number range investigated in Section 8.1. A differing dynamic pressure is investigated in Section 9.1.4. The investigations start with a convergence study of additional dynamic degrees of freedom in Section 9.1.1. Afterwards a CFD mesh convergence study is performed in Section 9.1.2. Section 9.1.3 presents flutter results employing a nonlinear structural model.

9.1.1. Degree of Freedom Convergence

Since the experimentally unstable Mach number range does not fit to the simulations with only a single degree of freedom, the number of dynamic degrees of freedom is increased in this section. For this

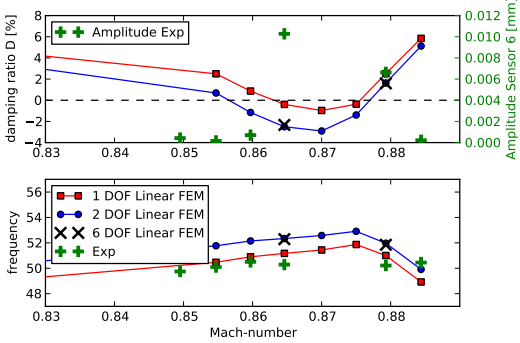

Figure 9.1.: Linear stability results (A.1, $M_a - M_g$): Comparision of 1 DOF (1^{st} bending), 2 DOF (1^{st} bending and torsion) and 6 DOF (eigenmodes 1-6)

purpose the unsteady aeroelastic model is expanded by the first six eigenmodes according to the eigenfrequencies.

In Figure 9.1 the flutter results are presented for one, two and six dynamic degrees of freedom. The two-degree-of-freedom case includes the first bending and first torsion m (mode 4). To reduce computation cost, the study for six DOF is limited to the two Mach numbers at which LCOs were observed in the experiment. It is shown that the first bending and torsion mode are sufficient to reach a converged aeroelastic model for the present flutter mechanism. The remaining eigenmodes do not significantly influence the flutter result. Hence, to reduce computational costs, all computations from this point onwards include only these two dynamic degrees of freedom.

Furthermore, it can be observed that the extension to the first torsion mode changes the flutter results considerably, compared to the SDOF studies. The unstable range with damping below zero is increased at both ends. But the unstable range does still not fit completely to the measured unstable points. The flutter frequency has increased by approximately 1-2 Hertz with the additional degree of freedom. The agreement of simulation and experiment in terms of frequency is therefore degraded compared to the SDOF analysis. However, one should keep in mind that the modelled structural

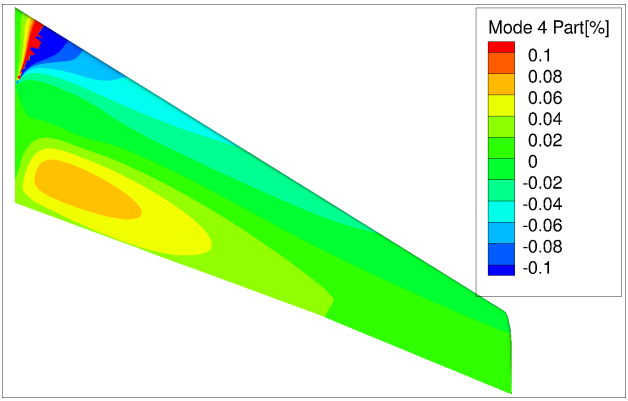

Figure 9.2.: 1^{st} torsion mode participation in flutter mode (z-direction): Mode 4 Part $= |\mathbf{q_4 \Phi_4}/(\mathbf{q_1 \Phi_1} + \mathbf{q_4 \Phi_4})|$, $\mathbf{q}$ - complex flutter eigenvector

eigenfrequency for the first bending mode is approximately 3Hz too high.

Figure 9.2 shows the participation of the first torsion mode in the overall flutter mode. It can be observed that the overall local flutter mode is only influenced by up to 0.1 percent, which means that the flutter mode is strongly dominated by the first bending mode. Thus, the experimental observations which lead to the single degree of freedom assumption in Chapter 8, could not notice such a small participation of the first torsion mode.

According to Figure 8.5 for the SDOF analysis, Figure 9.3 shows the generalized air forces entries of the matrix $\widehat{\mathbf{A}}$ for the first bending and torsion mode. It shows a peak between 80Hz and 90Hz for the excitation of mode 4. This peak can be explained by wind-tunnel interference. A general formula for a quadratic test section by (Voss, 1998, (9.2.3)) computes the lowest resonance frequency at approximately 83Hz. However, the aeroelastic behaviour of the overall system cannot be understood based on the GAFs alone, in contrast to the 1 DOF case. Instead, a more general criterion has to be applied, e.g. the Routh-Hurwitz Theorem. Its application to a 2 DOF system is shown by Weissenburger and Zimmerman (1964).

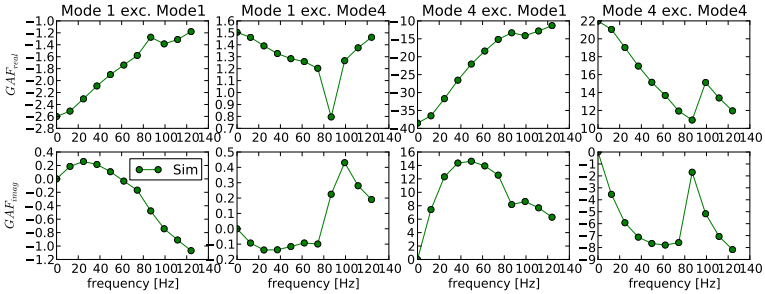

Figure 9.3.: Generalized Air Forces (GAF) $\widehat{A}_{i,j}$ matrix entries for $Ma = 0.8646$ (A.1, M_c), Mode 1=first bending mode, Mode 4=first torsion mode (Mode i excites Mode j)

9.1.2. CFD Mesh Convergence

In Section 6.1.1 the static CFD mesh convergence has been investigated for the complete static CFD-CSM process. In this section the influence of the grid resolution on the complete flutter process is investigated. The complete process includes the static CFD-CSM result, followed by the unsteady forced motion computations and subsequent flutter analysis. Therefore, deviations might accumulate. The meshes used are the same as for steady analysis, see Figure 6.2.

The flutter results of the analysis for two dynamic degrees are presented in Figure 9.4. It can be observed that the CFD mesh has a major influence on the results for higher Mach numbers. While the resulting flutter frequencies are in relatively good agreement, the damping values differ more distinct. Since the negative damping for the LCO cases is relatively small (only up to 2 percent), the influence of mesh resolution is clearly visible. It should be noted that for the flow case at the lower Mach number $Ma = 0.82$, which is almost not separated, all three meshes are in very good agreement. However, the differences of the strongly separated cases close or at LCO conditions are between one and two percent for the damping value.

Figure 9.5 and 9.6 show the steady and unsteady pressures for the Mach numbers $Ma = 0.82$ and $Ma = 0.8646$. Since the largest

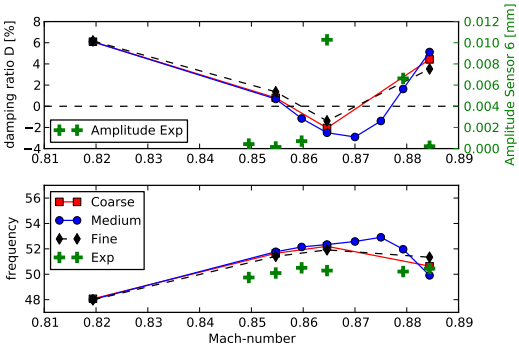

Figure 9.4.: Unsteady CFD mesh convergence: linear stability computations (A.1, S_a,$M_a - M_g$)

differences can be expected for the transonic upper side of the wing, the comparison of the unsteady pressures is limited to this part. For the lower Mach number the agreement between the different meshes is relatively good.For the higher Mach number, however, the small deviations in static pressures (Figure 7.14) lead to increased differences in the unsteady results. Especially the differing shock position in the outer section has a strong influence on the generalized air forces.

Reaching mesh convergence will be even more demanding for geometrically more complex industrial cases. This means that for such separated flow settings, which are already very demanding for the turbulence models (as seen Section 4.6, 7.3.1 and 8.1), the CFD mesh will introduce difficult to predict uncertainties of the flutter results.

In the following studies the CFD mesh of the previous Chapter 8 and the publication Stickan et al. (2014) is continued to be used (medium mesh). The challenge of mesh convergence is tackled again in the reference case chapter 10.

9.1.3. Nonlinear Structural Model

The static analysis employing a nonlinear structural model of Section 7.3.2 is extended to dynamic results in this section. Motivation

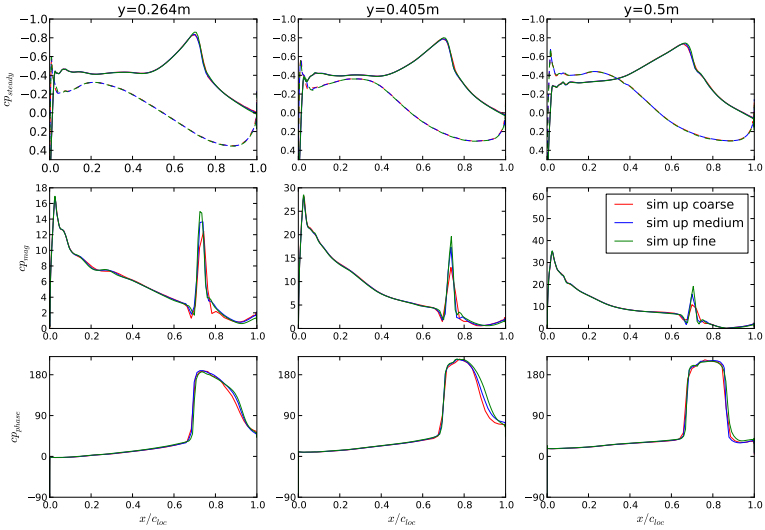

Figure 9.5.: Unsteady CFD mesh convergence: Ma $= 0.8194, \alpha = 0.0°$, steady pressures and pressure coefficient transfer function mode 1 (A.1, S_a)

is the inaccurate unstable range of the flutter results in Section 9.1. The static results have already shown a slightly different first shock position due to different airfoil cambering. This means the unsteady aerodynamics will also show differences.

The results based on the nonlinear FEM, including unsteady forced motion computations and frequency-domain p-k-method result, are using the structural modal analysis result from the structurally deformed and preloaded state. Roughly speaking, a new structural linearization at statically deformed conditions is performed.

Figure 9.7 shows the damping results in frequency-domain. It can be observed that the unstable range shifts slightly to higher Mach numbers. For the nonlinear FEM the range fits very well to the experiment. The steady and unsteady pressures for the linear and nonlinear FEM for $Ma = 0.8793$ are shown in Figure 9.8. The plot shows that the unsteady aerodynamics based on the nonlinear FEM fit better to the experimental values, although they do not reach the good agreement of lower Mach numbers. Particularly for the outer

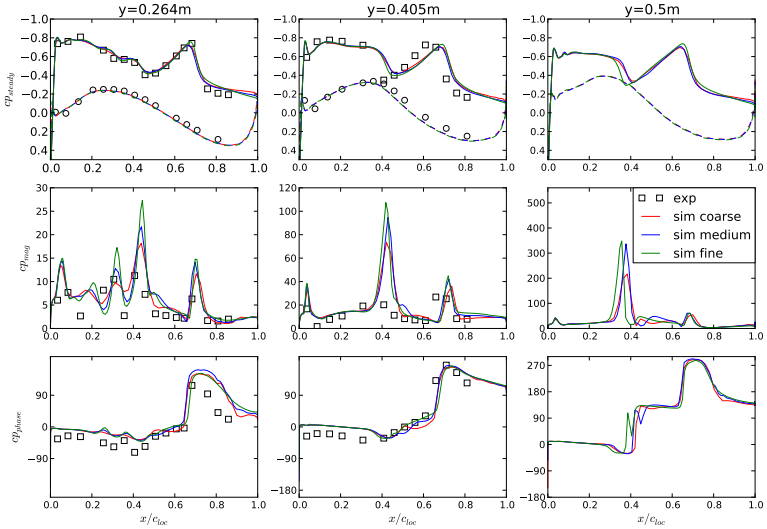

Figure 9.6.: Unsteady CFD mesh convergence: Ma $= 0.8646, \alpha = 2.69°$, steady pressures and pressure coefficient transfer function, mode 1 (A.1, M_c)

cut at $y = 0.5m$ large differences in the unsteady pressure transfer function occur, explaining the different flutter results.

To separate the effects of different steady aerodynamics and different structural eigenmodes Figure 9.9 includes additionally the flutter result for unsteady aerodynamics, where the steady solution has been computed with the nonlinear FEM, but the subsequently executed unsteady forced motion computations are performed with the linear FEM modes (no preloading etc.). The plot shows that the influence of the different eigenmodes is relatively small. Therefore, the main source of differences in the unsteady aerodynamics is the static CFD-CSM solution.

9.1.4. Dynamic Pressure Range

The experimental AEROSTABIL campaign was conducted to investigate the stability boundaries of the wing systematically. Therefore the numerical simulations can be verified with respect to another

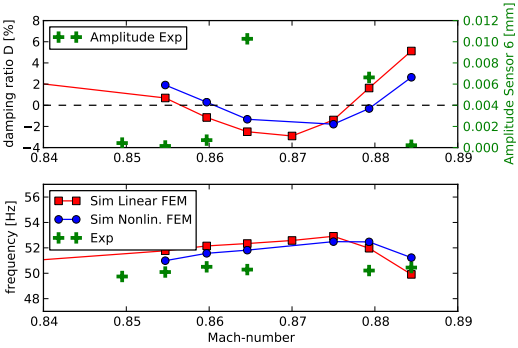

Figure 9.7.: Nonlinear FEM, flutter analysis result for Mach number range (A.1, $M_a - M_g$)

parameter axis, in this case the dynamic pressure q_∞. Although unsteady aerodynamics do not depend on the dynamic pressure except in terms of amplitude, for a flexible structure this assumption does not hold. The static equilibrium, which is computed as starting point for unsteady investigations, does strongly depend on the dynamic pressure. Increasing the dynamic pressure will increase the aerodynamic loads for these computations as well, and since the importance of the static aerodynamic solution was observed (especially in Section 9.1.3), the following studies are performed.

The Mach number is constant at $Ma = 0.8646$ while the dynamic pressure ranges from approximately 16kPa to 20.7kPa. The angle of attack is set to $\alpha = 2.69°$ according to the previous range of Mach numbers. As structural model the nonlinear model is utilized.

Figure 9.10 shows additionally to the results of frequency-domain simulation the motion amplitudes of the windtunnel experiments. Three clearly unstable measurement points can be identified for high dynamic pressures. The point with $q_\infty = 20.7kPa$ can also be found in the Mach number range. The damping results fit very well while the simulation frequencies are again 1-2Hz too high.

The steady and unsteady pressure results are compared to the experiment in Figure 9.11 for the third highest dynamic pressure of this range, $q_\infty = 17.7kPa$. A very good agreement to the experiment can be observed.

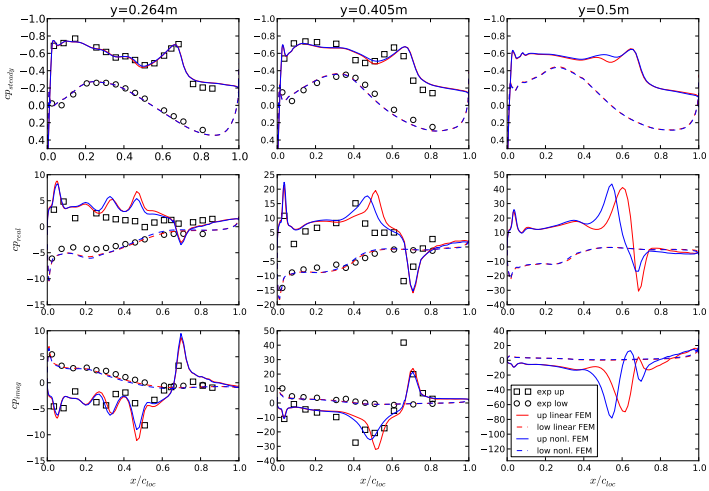

Figure 9.8.: Nonlinear/linear FEM, mean steady and unsteady first harmonic pressures for Ma = 0.8793, $\alpha = 2.69°$ (A.1, M_f)

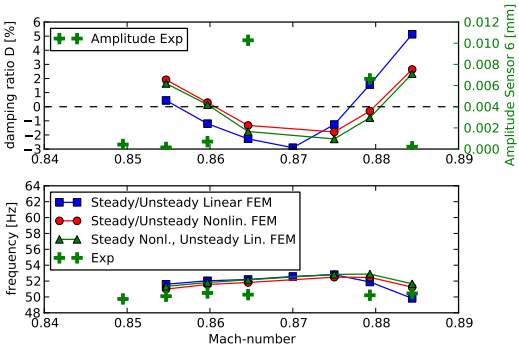

Figure 9.9.: Nonlinear FEM, flutter analysis result for Mach number Range, effect breakup steady/unsteady (A.1, $M_a - M_g$)

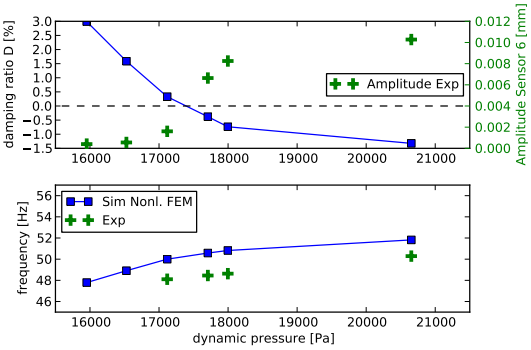

Figure 9.10.: Nonlinear FEM, flutter analysis result for dynamic-pressure range (A.1, $Q_a - Q_e, M_c$)

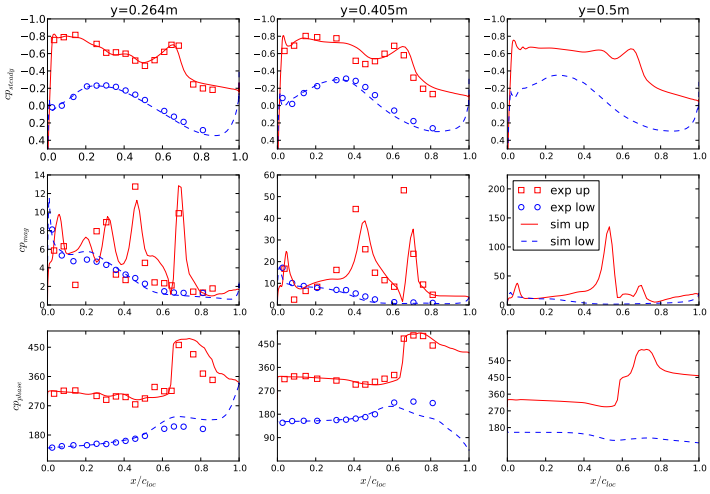

Figure 9.11.: Nonlinear FEM, mean steady and unsteady first harmonic pressures for Ma = 0.8646, $\alpha = 2.69°$, $q_\infty = 17.7kPa$ (A.1, Q_d)

Together with the results of Mach number range of Section 9.1.3 the nonlinear structural model allows to predict all four experimentally unstable points in the investigated parameter space. Hence these four points are used in the following section for time-domain LCO simulations.

9.2. Time-Domain LCO Analysis

After the basic frequency-domain analysis in this section time domain simulation results are presented. For this purpose the CFD-CSM method described in Section 3.6.2 and already applied in Section 8.2 is used.

According to the frequency-domain analysis two dynamic degrees of freedom are used in the generalized structural model. The dynamically linear structural model used in Section 9.1.3 serves as a basis. It is a generalized model extracted from a deformed and preloaded steady state of the nonlinear structural model.

9.2.1. Comparison to Experiments

In Section 9.1 four unstable points fitting to the experiment have been found, see Figures 9.7 and 9.10. These cases 1-4 are listed in Table 9.1. In this section time domain simulation result are compared to experimental measurements.

Case	Ma	$q_\infty[kPa]$	Reference	Remark
1	0.8646	20.653	A.1: M_c	Mach number
2	0.8793	20.884	A.1: M_f	range Sec. 9.1.3
3	0.8646	17.711	A.1: Q_d	Dynamc pressure
4	0.8646	18.001	A.1: Q_e	range Sec. 9.1.4

Table 9.1.: LCO case list for Section 9.2

Figure 9.12 shows the acceleration sensor 6 amplitude for two LCOs of the Mach number range investigated in Section 9.1.3 and Figure 9.13 shows the two additional LCOs of the dynamic-pressure range of Section 9.1.4. The simulations are started via a disturbance of the generalized coordinate of the first bending mode. The start amplitude has been chosen below the measured amplitude for cases 1+2. For cases 3+4 approximately the measured amplitude has been used. The corresponding plots for acceleration sensor 7 can be found in Appendix A.5.

The LCO cases 1+2 in Figure 9.12 show a too large amplitude for the lower Mach number $Ma = 0.8646$ and a too small amplitude for $Ma = 0.8793$. Case 1, which is the case with the largest measured

(a) $Ma = 0.8646$, $q_\infty = 20.7kPa$

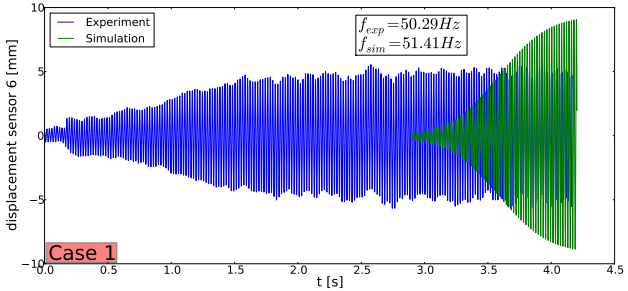

(b) $Ma = 0.8793$, $q_\infty = 20.9kPa$

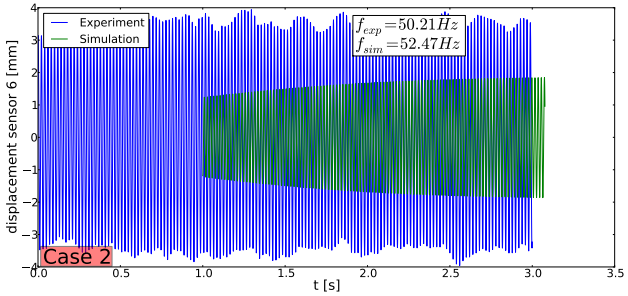

Figure 9.12.: Cases 1+2: amplitudes in z-direction versus time of experiment and simulation (2 DOF) for two different Mach numbers

amplitude, can be compared to the SDOF result in Figure 8.7. The amplitude of the nonlinear 2 DOF simulation is increased by a factor of three. The frequency-domain analysis in Section 9.1.1 shows a damping value of $D_{\text{1DOF}} = -0.39\%$ for 1 DOF, while the analysis based on two modes from a statically nonlinear analysis result in a damping value $D_{\text{2DOF,NL}} = -1.5\%$. Due to the nonlinear aerodynamics of the time-domain simulations the resulting amplitude levels can, however, not be predicted directly from the damping results. Further details about this point can be found in Section 10.3. Nevertheless, the higher Mach number $Ma = 0.8793$ with a linear frequency-domain damping value of $D_{\text{2DOF,NL}} = -0.31\%$ shows only an amplitude of approximately 2mm at sensor 6, compared to

(a) Case 3: $q_\infty = 17.7kPa$

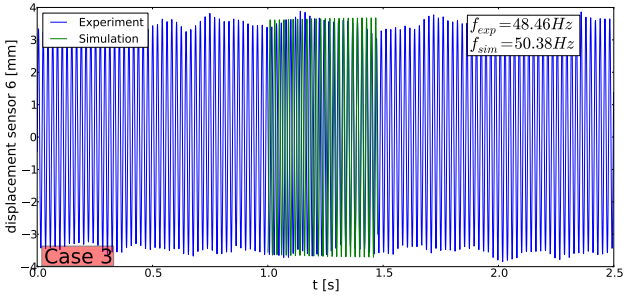

(b) Case 4: $q_\infty = 18.0kPa$

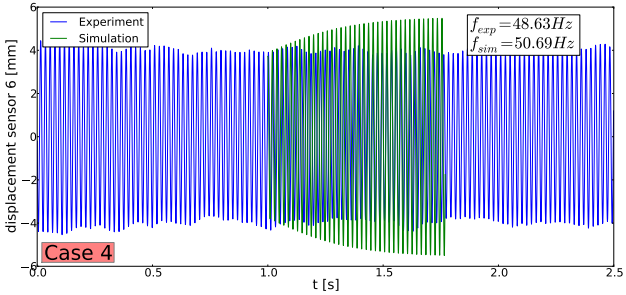

Figure 9.13.: Cases 3+4: amplitudes in z-direction versus time of experiment and simulation (2 DOF) for two different dynamic pressures, $Ma = 0.8646$

the 3.5mm measured in the experiment.

The LCO cases in Figure 9.13 of the dynamic pressure range show a better agreement in amplitude, especially the case 3 at $q_\infty = 17.7kPa$ reveals an excellent agreement in amplitude.

All in all, it should be kept in mind: The frequency-domain studies, and also the SDOF studies in Chapter 8, have shown the sensitivity of the result to many parameters: Structural damping, turbulence model, CFD-mesh and structural modelling. In addition, the flow boundary conditions will have a large influence and further influence parameter can be found easily. Therefore the agreement in amplitude should not be the most important measure for the quality of results.

The comparison of simulation and experimental LCO frequencies is additionally contained in the LCO Figures 9.12 and 9.13. As seen for die flutter analysis, the frequencies of the simulation are too high, approximately 2Hz for most cases. But it should be recalled that the FEM eigenfrequency of the first bending mode is approx. 3 Hz too high compared to GVT data (see Table 6.1).

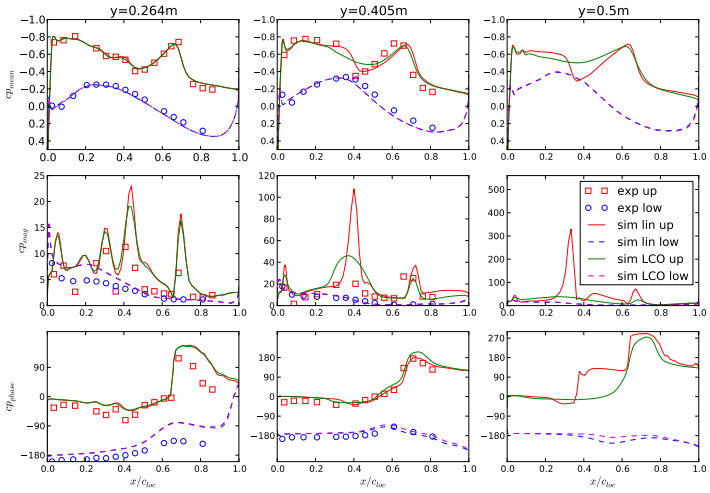

Figure 9.14.: Case 1: Mean steady and unsteady first harmonic pressures for Ma = 0.8646, $q_\infty = 20.7kPa$ (A.1, M_c), lin: unsteady linear (small amplitude) aerodynamics from Section 9.1, LCO: time-domain simulation

Figure 9.14 shows for case 1 the linear frequency-domain aerodynamics from Section 9.1.3 at LCO frequency and the unsteady nonlinear aerodynamics from the LCO computations. The steady pressures from the static CFD-CSM computation are compared to the mean pressures from the LCO simulations. The unsteady pressures are compared by means of the first harmonic pressure transfer function. It can be observed that the excessive motion amplitude of case 1 is also reflected in the comparison of pressures to the experiment. The section at $y = 0.405m$ shows for the mean pressures of the simulations no clear upstream shock for the LCO case. Due

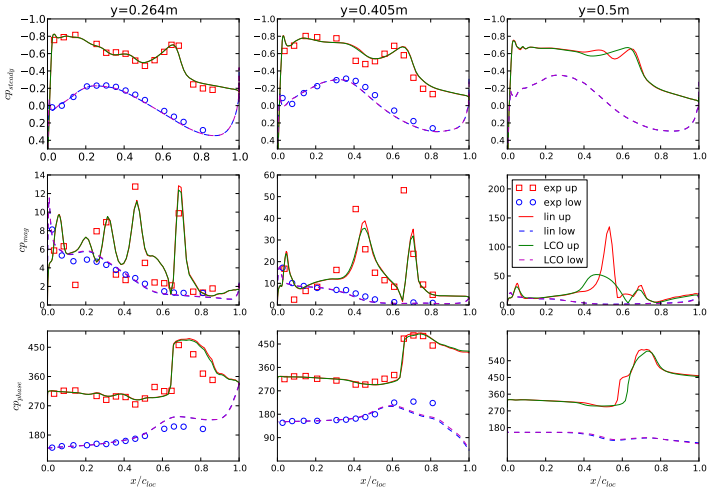

Figure 9.15.: Case 3: Mean steady and unsteady first harmonic pressures for Ma = 0.8646 , $q_\infty = 17.7kPa$ (A.1, Q_d), lin: unsteady linear (small amplitude) aerodynamics from Section 9.1, LCO: time-domain simulation

to strong shock movement the shock is blurred. This behaviour cannot be found in the experimental values, where the shock position remains distinct. Also the unsteady pressure amplitude for the same section shows a too wide shock peak, not fitting to the experiment. Therefore, the too large amplitude (Figure 9.12, top) is well reflected in the pressure results. It should also be noted that the effects of section $y = 0.405m$ are more pronounced for section $y = 0.5m$. Here a shock bump is almost not visible and additionally the unsteady pressure phase changes strongly.

In contrast Figure 9.15 shows the pressure for case 3, which has the same Mach number but lower dynamic pressure $q_\infty = 17.7kPa$. This case has shown a very good agreement in motion amplitude to the experiment. This good agreement is as well reflected in the pressures. The differences for the section at $y = 0.405m$ between linear and LCO aerodynamics are very small, hence the clear shock position visible in the steady pressures and the sharp shock of the

Case 1: $Ma = 0.8646$, $q_\infty = 20.7kPa$

(a) 0.0° (b) 90.0° (c) 180.0° (d) 270.0°

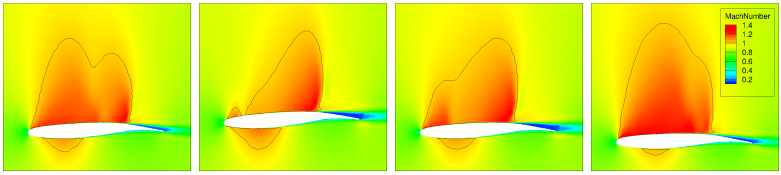

Case 3: $Ma = 0.8646$, $q_\infty = 17.7kPa$

(e) 0.0° (f) 90.0° (g) 180.0° (h) 270.0°

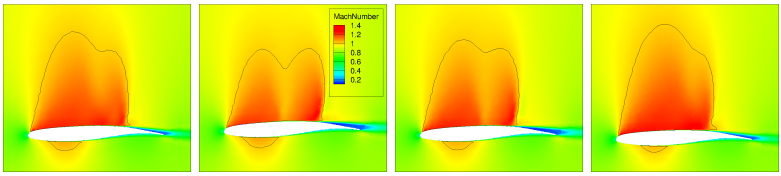

Figure 9.16.: Cases 1+3: Ma = 0.8646, LCO-state (A.1, M_c, Q_d): Mach number in CFD domain cut-plane at y=0.5m at different phase angles of the LCO cycle

unsteady measured pressures coincide well. Strong nonlinear aerodynamic effects are only visible for the outer section with the usual features like a wide shock peak for the unsteady pressure amplitude.

The shock motion is also visualized in the volume solution for case 1 and 3 in Figure 9.16. This plot shows clearly the strong first shock motion of the case 1; the shock is almost moving up to the leading edge. For case 3 with lower dynamic pressure the shock motion is much smaller.

9.2.2. LCO Mechanism

The pressure plots in the previous Section 9.2.1 have shown large differences in the unsteady pressures on the upper wing side due to strong shock motion. Therefore, the upper side of the wing is analyzed in terms of work per cycle, as in Section 8.2.

Figures 9.17 and 9.18 show the work per cycle results for the Mach numbers $Ma = 0.8646$ and $Ma = 0.8793$ (Case 1+2) of the

LCOs visible in Figure 9.12. It can be noted that the energy transfer from the aerodynamics to the structure changes strongly for the large-amplitude case 1 comparing linear and nonlinear aerodynamics. On the other hand, the changes for the small-amplitude case 2 are difficult to identify, but can be spotted at the outer wing area.

Figures 9.19 and 9.20 allow to compare the normalised work per cycle of linear (frequency-domain) and nonlinear (time-domain) aerodynamics at the measurement sections. Since the unsteady pressure transfer functions are plotted as well, the direct connection between change in unsteady aerodynamics and energy transfer can be observed. For the large amplitude case 1 this connection is rather difficult to be identified, since the extreme shock motion changes the unsteady pressures and, therefore, also the work per cycle completely. For the small amplitude case it can be noted clearer that the increased shock motion leads to a reduced energy transfer into the wing surface. Theplots corresponding to cases 3+4 can be found in Appendix A.6.

Altogether, the same amplitude limiter, which has been found in Chapter 8 for a single dynamic degree of freedom, is confirmed for all four investigated LCOs: Increased shock motion leads to a reduced energy transfer into the wing structure.

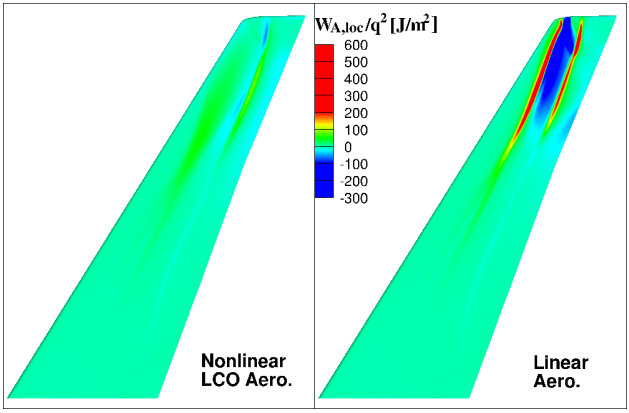

Figure 9.17.: Case 1: Work per cycle, local, surface plot: Ma = 0.8646 (A.1, M_c)

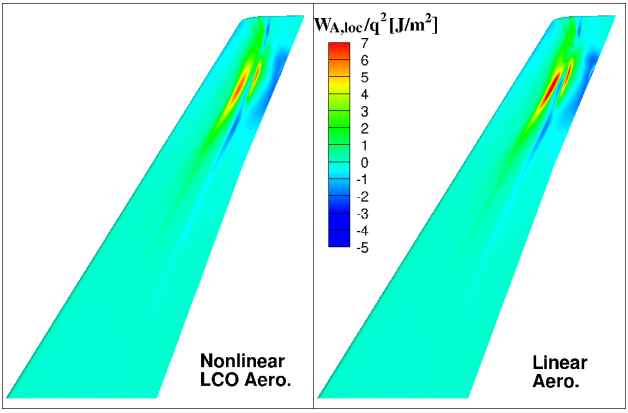

Figure 9.18.: Case 2: Work per cycle, local, surface plot: Ma = 0.8793 (A.1, M_f)

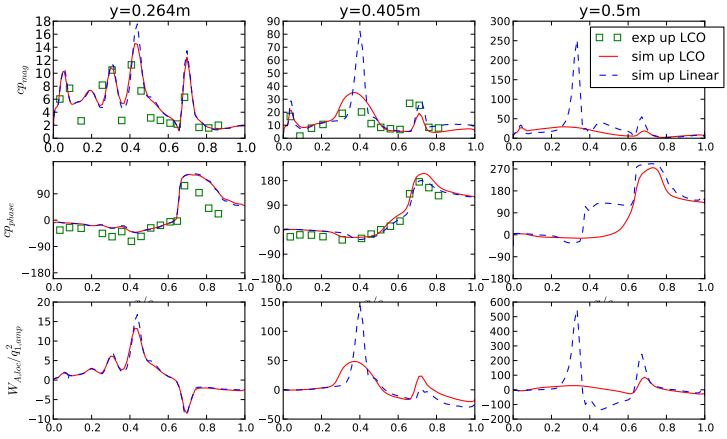

Figure 9.19.: Case 1: Work per cycle, local: Ma = 0.8646, LCO amplitude at sensor 6 ca. 8mm (A.1, M_c)

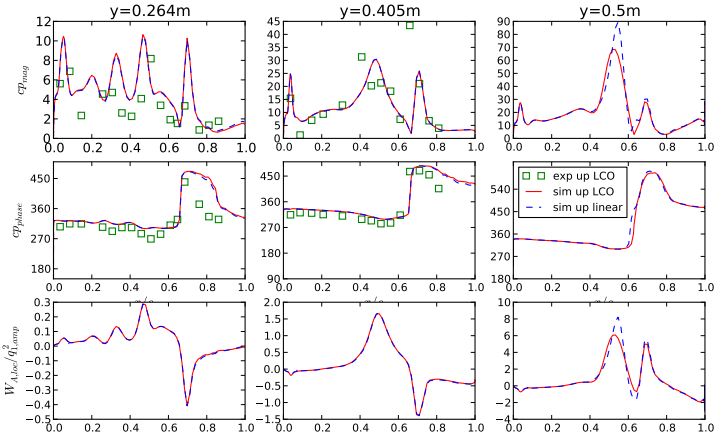

Figure 9.20.: Case 2: Work per cycle, local: Ma = 0.8793 , LCO amplitude at sensor 6 ca. 2mm (A.1, M_f)

9.3. Studies

9.3.1. Unsteady Influence of Camber Bending

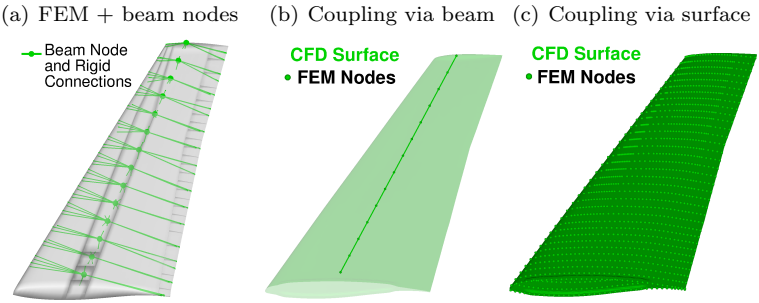

Figure 9.21.: FEM model with beam-nodes connected via rigid body elements (left), CFD-CSM coupling using these new points (middle), CFD-CSM coupling using surface nodes (right)

In flutter analysis of aircraft the unsteady cambering is dominated by control surface motion, but also studies with intended cambering of the main structure have been performed. Kang et al. (2014) have investigated the effect of unsteady local flexibility on performance. The study has shown, if the unsteady shedding frequency is close the structural eigenfrequency, an increase in lift can be produced. Walker and Patil (2010) present an analytic aerodynamic model similar to the derivations by Theodorsen (1935), which can cover unsteady cambering of airfoils. However, both studies are limited to subsonic flows.

In Stickan et al. (2014) it is shown for the SDOF system of Chapter 8 that without the camber bending, even if only the marginally cambering first bending mode is investigated, the aerodynamic excitation is reduced and no unstable behaviour can be found. This investigation is continued here by considering two dynamic degrees of freedom, the first bending and torsion mode.

To perform the analysis a line of nodes has been added to the structural model. These points are connected via rigid body ele-

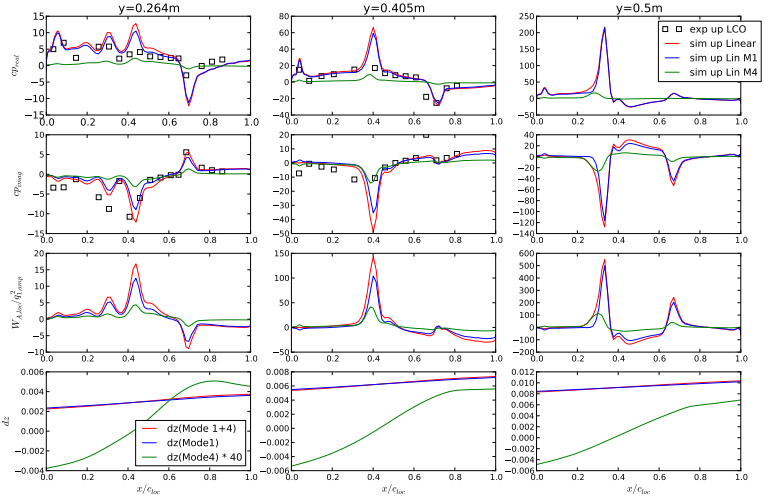

Figure 9.22.: Unsteady pressures, excitation and mode shapes: $\mathrm{Ma} = 0.8646, \alpha = 2.69°$ (A.1, M_c), pressures split via flutter analysis eigenvector

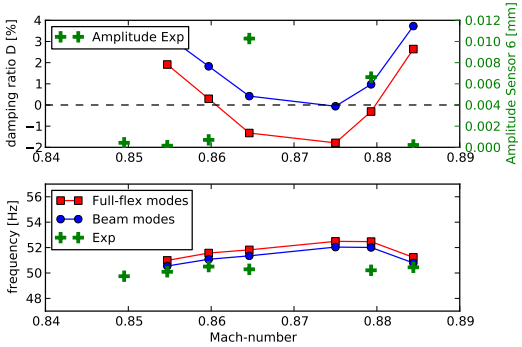

Figure 9.23.: Flutter result with modes of statically nonlinear FEM run, 2DOF: influence of camber bending (A.1, $M_a - M_g$)

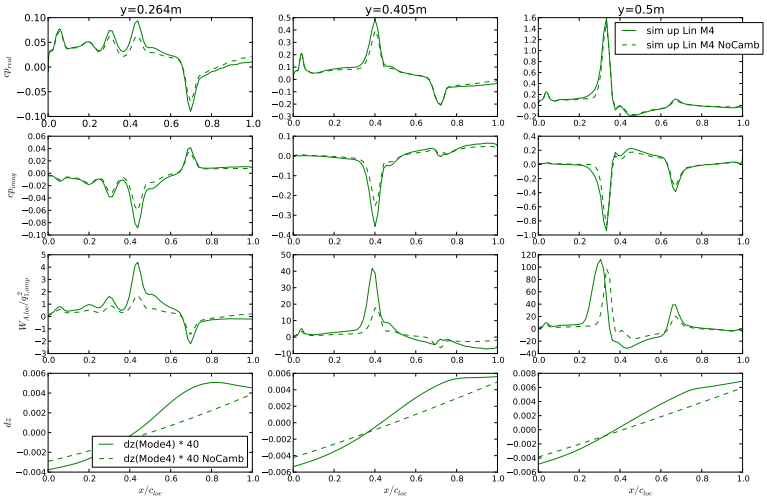

Figure 9.24.: Unsteady pressures, excitation and mode shape of 1^{st} torsion mode only: $\mathrm{Ma} = 0.8646, \alpha = 2.69°$ (A.1, M_c), pressures split via flutter analysis eigenvector

ments (RBE3) to the shell elements of the structural model. This line of nodes is then used for a mode interpolation method which preserves the profiles normal to the beam axis. The FEM-update and coupling setup can be inspected in Figure 9.21. The figure shows additionally the coupling using all surface nodes of the structural model which was used up to this point of the work.

To make it clear: The steady solution is the same for all cases, only the mode shapes on the aerodynamic surface used for the unsteady computation are changing.

Starting point is the evaluation of the unsteady aerodynamics for the case with the smallest damping, already seen in Figure 8.3: $Ma = 0.8646$, $q_\infty = 20.7kPa$. The flutter mode from the entries in the generalized coordinate vector $\mathbf{q}$, see Equation (3.57), is used to split the unsteady pressures into a part stemming from the bending mode and a part stemming from the torsion mode. Figure 9.22 shows the unsteady pressures (in real and imaginary part for better comparison), the local work per cycle and the flutter mode itself. It can be observed that the unsteady pressures and work per cycle

are dominated by the pressures of the bending mode, Mode1. But considering the individual mode participation, the highest level of cambering of the flutter mode is found in the torsion mode, Mode4.

The results of the flutter analysis with beam coupling can be compared to the surface coupling in Figure 9.23. It shows that without unsteady cambering the wing damping is increased by around two percent for the critical coupling.

Figure 9.24 explains this by using a plot similar to Figure 9.22, but only considering the mode with the most cambering: the torsion mode. The lowest row in the plot shows clearly that the beam coupling does not include cambering any more. The influence on the pressures and work per cycle is obvious: The pressure magnitudes are decreased. Accordingly, the work per cycle is reduced.

This analysis shows the importance of capturing unsteady cambering for aeroelastic investigations. Regarding complex aircraft investigations, it shows especially the importance of unsteady aerodynamic modelling of control surfaces, since these secondary structures have the most influence on cambering for a typical wing.

9.3.2. Influence of Angle of Attack

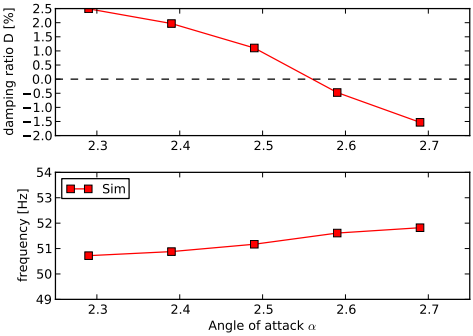

Figure 9.25.: $Ma = 0.8646$ (A.1, M_c): Linear stability computations with nonlinear FEM, influence of angle of attack α

In Section 4.2 the influence of the angle of attack on the unsteady

aerodynamics is presented. The importance of the angle of attack is already shown in the experimental investigations presented in Chapter 5: In Figure 5.3 it is shown that the unstable LCO points are approached by increasing the angle of attack until the oscillations start.

The investigation of this section shall verify the behaviour of the aeroelastic model by performing stability analysis for several different angles of attack below the angle $\alpha = 2.69°$ used for the investigations up to this point.

The results of this study are illustrated in Figure 9.25. The plot shows a significant decrease of damping of the aeroelastic system with increasing angle of attack. An angle of attack decrease of $\Delta\alpha = 0.4°$ results in four percent increase in damping.

Additionally, it can be observed that the system is undamped for an angle alpha $\alpha \gtrsim 2.56°$. Assuming $\delta\alpha = 0.1$ steps as applied in the experiment, this means the numerically consistent LCO would appear between $\alpha = 2.56°$ and $\alpha = 2.66°$. Therefore, the angle of attack $\alpha = 2.69°$ used for the computations has been selected too large. This explains the too large LCO amplitudes seen in Section 9.2.1. If desired the angle of attack could be adjusted to find a LCO amplitude which agrees to the experiment. However, this task is not performed here as no additional insight into the physics is expected.

10. Reference Case

This chapter provides a reference case which can be recomputed by other parties. For this purpose it uses aerodynamic boundary conditions that are easy to reproduce. Additionally, a mesh convergence study is repeated and further deepened.

The reference case data can be requested at the German Aerospace Center, Institute of Aeroelasticity; Contact: Holger Hennings, Head of Aeroelastic Simulation department, Holger.Hennings@dlr.de.

10.1. Simulation Setup

This section describes the boundary conditions as well as the methods and the model used.

Starting point for the creation of reference case was an attempt to use a simplified geometry to ease recomputations. A valuable simplification would have been the removal of the windtunnel walls. But studies have shown that the walls are indispensable. Hence, the same CFD geometry as in the previous chapters is used. The windtunnel walls are modelled as viscous walls again.

In the studies of the previous chapters farfield boundary conditions have been used in TAU for inflow and outflow boundaries. Due to possibly different farfield implementations in other CFD codes, this definition cannot be used. Instead, a Dirichlet boundary condition with flow direction in x-axis direction is used at the inflow boundary (Figure 5.2). Additionally, the pressure p_{in}, the Mach number Ma_{in} and the velocity v_{in} are defined on the inlet surface. At the outflow boundary only the outflow pressure p_{out} is defined. The outlet pressure has been adjusted to match the measured static pressures. The importance of the first shock was shown in previous studies, and thus, to fit this shock was the main target. The flow parameter of the reference cases can be found in Table 10.1. The flow reference state is defined by reference Mach number, Reynolds-

Ma_{ref}	Re_{ref}	$p_{\text{ref}}[Pa]$	$\alpha[^\circ]$	$v_{in}[\frac{m}{s}]$	Ma_{in}	$p_{in}[Pa]$	$p_{out}[Pa]$
0.8547	$1.6905{\cdot}10^6$	40079	2.69	276.86	0.8380	40080	39500
0.8597	$1.6905{\cdot}10^6$	39770	2.69	278.25	0.8429	39770	39200
0.8646	$1.6905{\cdot}10^6$	39470	2.69	280.0	0.8488	39470	39000

Constant CFD parameter for all cases
Heat capacity ratio $\gamma = 1.4$
Ideal gas constant $R = 287$
Sutherland constant C_0 =110.4K
Sutherland reference viscosity $\mu_{\text{ref}} = 1.716 \cdot 10^5 kg/(m \cdot s)$
Sutherland reference Temperature $S_{\text{ref}} = 304.1322K$

Table 10.1.: Flow parameter, remark: the wing angle of attack α for CFD is corrected due to CAD geometry inaccuracy, CFD wing angle $\alpha_{\text{CFD}} = \alpha + 0.41^\circ$

number and pressure (Ma_{ref}, Re_{ref} and p_{ref}).

As already applied in Chapter 7, the structural model is used in the generalized form. No structural nonlinearities or preloading for the eigenmode analysis are taken into account in this chapter. 200 modes have been used for the static computations, while for the dynamic analysis again only the first bending and first torsion mode with equal modal damping as defined in Table 6.1 are considered.

The coupling of all FEM and CFD wing surface nodes with radial basis functions is equal to the coupling seen in Figure 9.20(c). As core function the 'thin-plate spline' has been applied.

Since the mesh convergence studies in Section 9.1.2 revealed problems, new CFD meshes have been created. For these new CFD meshes the return of experience from the previous studies has been incorporated. This includes a slightly refined boundary layer and a concentrated volume refinement above the upper wing side. The surfaces and volume cuts through the different meshes are plotted in Figures 10.1 and 10.2. The medium mesh contains 4.7 million nodes; the coarse one has a factor 1.5 increased spacing, resulting in 1.8 million nodes. For the fine mesh the spacing is reduced by factor 1.5 accordingly, resulting in a 14.4 million node mesh.

The Menter SST turbulence model is used again. Further CFD parameter can be found in appendix A.7.

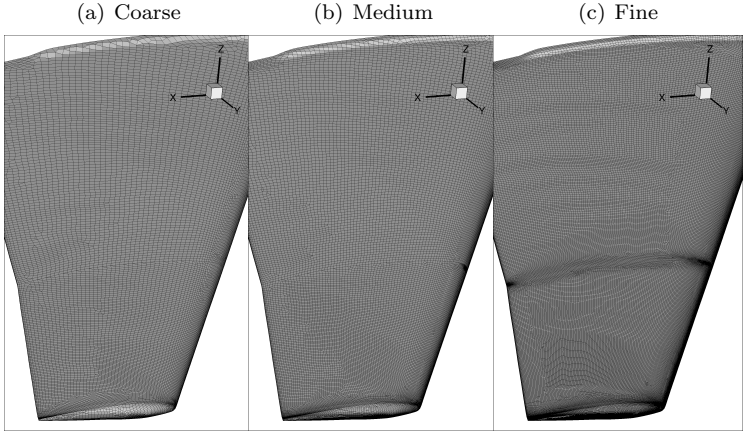

Figure 10.1.: CFD meshes for mesh convergence study: Coarse mesh with 1.8 million nodes, medium mesh with 4.7 million nodes, fine mesh with 14.4 million nodes

10.2. Steady Solution and Flutter Analysis

As already seen in Chapters 8 and 9 starting point of the investigations are the static CFD-CSM results. The steady simulations are followed by forced motion computations of the first bending and torsion mode. In this case harmonic computations with 60 steps per period have been performed for all reduced frequencies $k = 0.05 \cdot i, i = 1, .., 10$.

The steady pressures and unsteady pressure transfer functions can be examined for the highest investigated Mach number $Ma = 0.8646$ in Figure 10.3. The steady pressures of the three meshes are in very good agreement. For the unsteady pressures the different cell density leads to less sharp shock peaks in the magnitude plot. But also here the agreement is acceptable. The very good agreement to the experiment is the result of the outflow pressure tuning.

Inspecting the p-k-method result in Figure 10.4 shows a clear convergence trend from the coarse to the fine mesh. For all 3 meshes negative damping is reached at $Ma = 0.8646$, but for increasing mesh density the absolute damping value is decreasing. The coarse

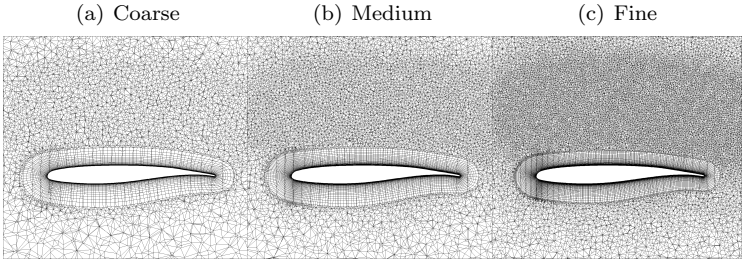

Figure 10.2.: CFD meshes for reference case study: volume cuts at y=0.5m

mesh lead to a damping ratio of $D = -0.3\%$ while the fine mesh shows only $D = -0.033\%$. But all three meshes are expected to show limit-cycle oscillations.

10.3. Limit-Cycle Oscillations

Finally the LCO amplitudes should be compared for the three meshes. The simulations for all three meshes have been started at the level of the measured amplitudes. It can be observed that, according to the damping values, the coarse mesh shows the largest amplitude and the finest the smallest.

This behaviou can be explained in more detail based on Figure 10.6. It shows the diagonal entries of the GAF-matrix for the first bending mode at reduced frequency $k = 0.2$ (approx. LCO frequency) for different amplitudes. The data has been generated by harmonic forced motion computations for various amplitudes. As already seen in the 2D examples in Section 4.5 the values seem to converge for very small amplitudes. But the different CFD meshes show clear differences. These differences are in line with the differences in the damping result as shown in Figure 10.4. A larger GAF amplitude $GAF_{1,1,mag}$ results in a lower damping value. Hence, it can be observed that the magnitude of small-amplitude aerodynamics and the resulting flutter results have the largest influence on the LCO amplitude differences, while the magnitude degradation $\Delta\mathrm{GAF}_{1,1,mag}$, the nonlinear part of the unsteady aerodynamics, is

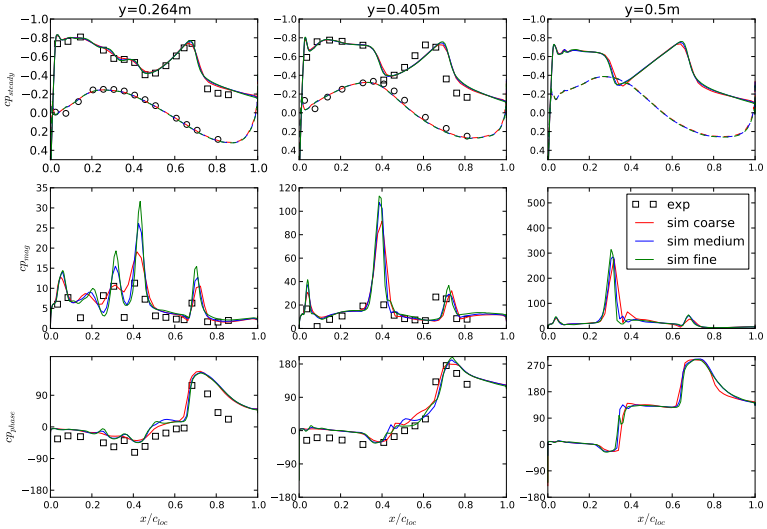

Figure 10.3.: Reference case study: Ma $= 0.8646, \alpha = 2.69°$, steady pressures and pressure coefficient transfer function mode 1

very similar for all meshes.

Overall, as already seen in all previous chapters, the flutter damping values and LCO amplitudes are very sensitive, which is reflected in this chapter in the mesh density. But due to the optimized mesh refinement, a mesh convergence trend could be shown.

10.4. Hints for Case-Recomputation

All previous studies have shown that a good fit in static pressures is essential for the simulation of accurate damping values and, thus, for an adequate representation of LCOs. Only minor parameter changes might be necessary to tune the static pressures. The main parameters to tune are the flow speed/ outflow pressure and the angle of attack. Furthermore, it is recommended to perform frequency domain studies before starting costly time-domain simulations.

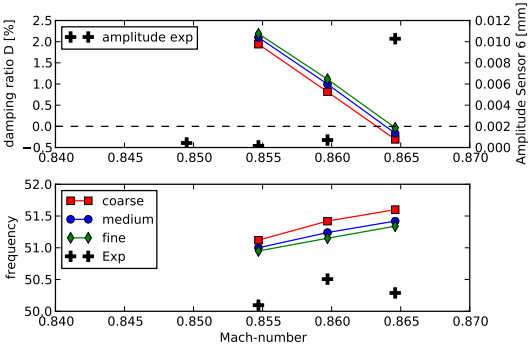

Figure 10.4.: Reference case study: linear stability computations

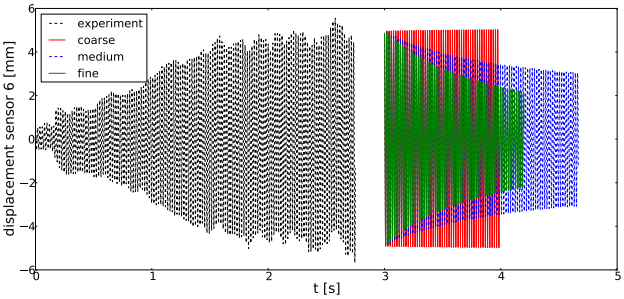

Figure 10.5.: Reference cases $Ma = 0.8646$: amplitudes in z-direction versus time of experiment and simulation

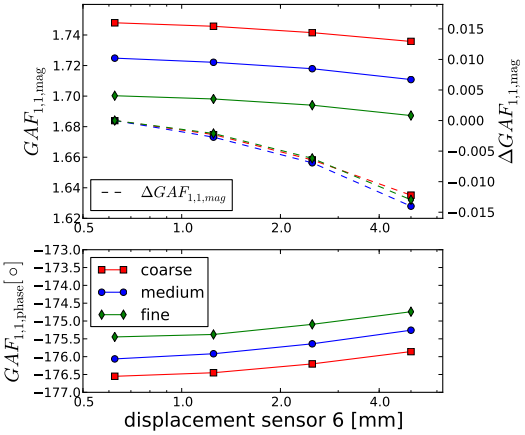

Figure 10.6.: Reference cases $Ma = 0.8646$: Generalized air forces $\mathrm{GAF}_{1,1}$ of first bending mode in magnitude and phase versus amplitude of sensor 6 in harmonic forced motion computation; additionally difference of GAF relative to smallest amplitude GAF.

11. Conclusion

-

11.1. Summary of Results

The main objective of this thesis has been the explanation of the AEROSTABIL limit-cycle oscillations by means of computational aeroelastic simulations. To this end, the experiment allowed further valuable discoveries, especially the strong deformations of the wing profiles.

To enable the aeroelastic investigation an aeroelastic toolbox with focus on CFD-CSM interaction has been developed. It includes modules for CFD mesh deformation, CFD-CSM coupling, steady and unsteady CFD-CSM interaction and the computation of unsteady aerodynamics by forced excitation. The modules are tailored for highest possible accuracy at smallest possible computational costs. The modules for CFD-mesh deformation and CFD-CSM coupling are of primary importance. The combination of both allows using structural and aerodynamic models of arbitrary detail level for aeroelastic purposes. In addition, it has been indicated that the modules are applicable to ambitious industrial configurations. This has been demonstrated successfully based on a flight test validation case of the A340-300.

To allow a deep understanding of the challenging three-dimensional flow effects of the AEROSTABIL wing, two-dimensional numerical experiments have been conducted. The results give an introduction to the possible effects in unsteady transonic aerodynamics.

The static investigations of the AEROSTABIL experiment have already allowed to show the importance of the high-fidelity simulation approach: The profile deformations could only be found in the detailed structural model. The subsequent experimental validation of this effect confirmed the accuracy achieved. In terms of

the LCO conditions the additional challenges have become visible: The transonic flow setting contains not only a double-shock system, but also strong flow separation. Particularly the flow separation is challenging the employed Reynolds-averaged Navier Stokes code. It has been shown that the aerodynamic simulation results strongly depend on the turbulence model applied. The best agreement could be achieved with the Menter SST model.

The seldom occurrence of an unstable LCO involving one structural DOF was revealed by transient analysis. First, the aeroelastic system has been reduced to only a single dynamic degree of freedom, the first bending eigenmode. This seldom occurrence of an unstable SDOF system already allowed the complete explanation of the observed LCOs: The aerodynamic excitation is reduced with increasing motion amplitude due to a strong shock movement.

Furthermore, it was demonstrated that additional computational dynamic DOFs can improve the agreement with stability boundaries. Here it was observed that the critical coupling can be described more accurately with two DOF: the first bending and first torsion mode. But the flutter mode is very similar to the SDOF flutter mode. Hence the physical LCO trigger is the same. But the additional DOF has enabled to reach an excellent agreement with the measured stability ranges. The 2-DOF system has also been used successfully to validate the LCO limiter at different experimental measurement points. It has been shown that the LCO amplitudes are very sensitive to the different aerodynamic parameters. Nevertheless, for some cases an excellent agreement with the measured amplitude has been presented.

An important finding for the unsteady investigations is that without accurate static pressures also the measured LCOs cannot be simulated. Here only the Menter SST turbulence model has reached an adequate accuracy for the static pressures to predict the unstable behaviour of this wing. Therefore, the turbulence model should be chosen very carefully for flutter investigations including CFD of any kind. Furthermore, the investigations showed that unsteady camber effects, e.g. induced by control surfaces, cannot be neglected in unsteady investigations.

To sum up: The AEROSTABIL experiment provides a very challenging test case for the developed aeroelastic simulation tools. Vice versa these computational means have facilitated to explain the

AEROSTABIL LCOs in a very convincing manner and showed the high accuracy that can be attained by today's aeroelastic simulation capabilities.

11.2. Future Work

With respect to the employed aeroelastic methods, the CFD-mesh deformation is the most critical brick in the aeroelastic simulation chains. The method presented in this work has shown suitable robustness. However, a major challenge to deal with defective results, e.g. due to negative cells, remains.

Regarding the aerodynamic modelling, the sensitivity to turbulence modelling and mesh point density for flutter investigations must be further analysed and classified. Usage of further experimental data of other windtunnel models and settings might improve the physical understanding to select a sufficiently accurate turbulence model. However, the aerodynamic codes commonly applied in industry do not yet permit to use an arbitrary turbulence model with acceptable computation time. Here the introduction of different turbulence models in time-linearized CFD codes is essential.

The AEROSTABIL experiment and its large database can serve as validation case for newly developed methods and models in the future. Its unique features offer an excellent foundation for this purpose. But it should always be kept in mind that, besides the aerodynamic model, the structural model contains still uncertainties in the modelling quality.

A. Appendix

A.1. Flow Parameter

ID	Ma	Re $[\cdot 10^6]$	$\alpha[^\circ]$	$q_\infty[kPa]$	$p_{\text{ref}}[kPa]$	Remark
S_a	0.8194	1.3278	0.0	16.227	34.528	
M_a	0.8547	1.6905	2.69	20.495	40.079	
M_b	0.8597	1.6905	2.69	20.575	39.770	
M_c	0.8646	1.6905	2.69	20.653	39.947	
M_d	0.8700	1.6905	2.69	20..738	39.142	No exp.
M_e	0.8750	1.6905	2.69	20.817	38.842	No exp.
M_f	0.8793	1.6905	2.69	20.884	38.587	
M_g	0.8844	1.6905	2.69	20.963	38.288	
Q_a	0.8646	1.2991	2.69	15.944	30.479	
Q_b	0.8646	1.3444	2.69	16.531	31.592	
Q_c	0.8646	1.3908	2.69	17.121	32.721	
Q_d	0.8646	1.4381	2.69	17.711	33.847	
Q_e	0.8646	1.4622	2.69	18.001	34.401	
F_a	0.75	1.3849	0.0	14.404	36.582	FLIB exp.

Table A.1.: Flow parameter

The parameter in Table A.1 have been used as far-field boundary conditions for the inflow and outflow plane of the windtunnel meshes shown in 3.1. Therefore a direct comparison to a regular far-field CFD mesh without walls is not possible. Figure A.1 shows the Mach number and pressure along the center of the windtunnel up to the wing-model position. This plot gives an impression how these values evolve along the windtunnel. It shows that the far-field boundary conditions lead to slightly reduced Mach number upstream of the wing-model. The defined Mach number is approximately reached at the outflow boundary, but not at the inflow boundary. The reason

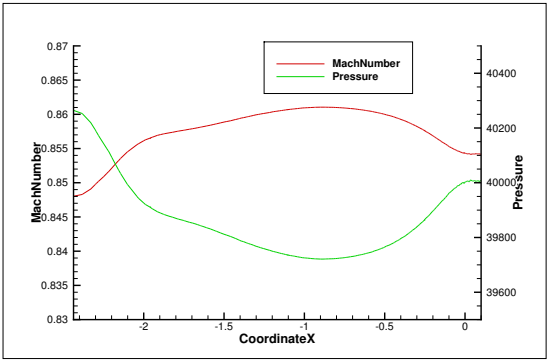

Figure A.1.: Mach number and pressure along center line of windtunnel CFD mesh for $Ma = 0.8646$ (M_c in table A.1, model wing-root leading edge at $x = 0.0$)

for the Mach number growth up to x=-1m is the development of a boundary layer at the windtunnel walls.

A.2. Pulse Example

Example for pulse computation with FSForcedMotion, introduced in Section 3.6.3.

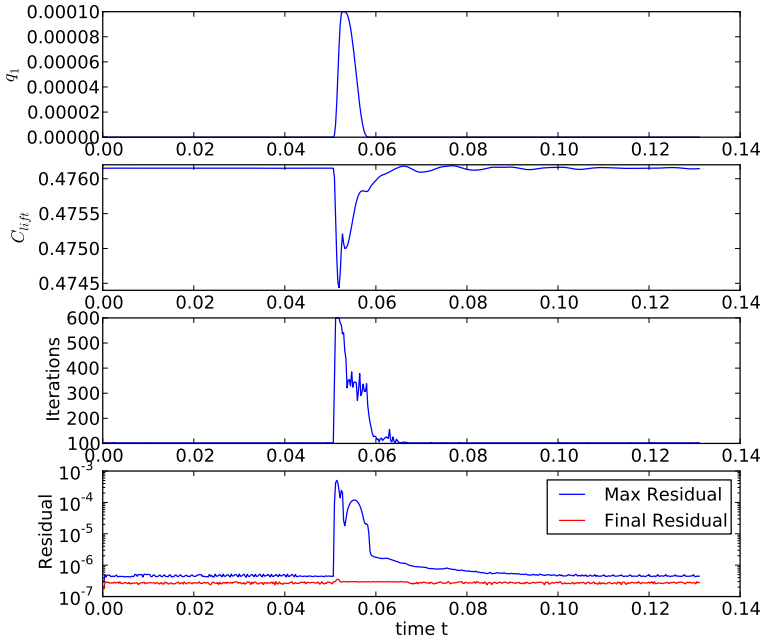

Figure A.2.: Pulse example time history showing generalised coordinate of mode 1 q_1, lift coefficient C_{lift}, CFD iteration per time step and CFD density residual (Max Residual: maximal residual during iterations, Final Residual: residual at the end of inner time-step iterations)

A.3. Reynolds Stress Model

This section contains additional AEROSTABIL flutter result for Section 8.1 with RSM turbulence model.

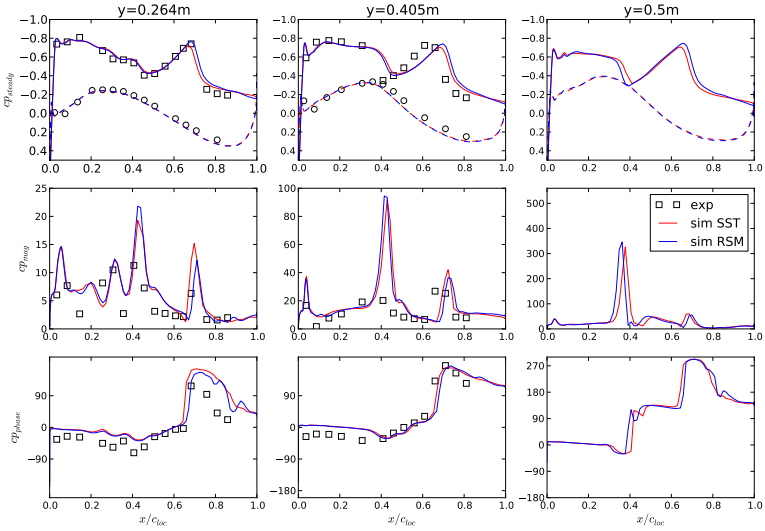

Figure A.3.: Steady and unsteady pressures for SST and RSM turbulence models, Ma $= 0.8646, \alpha = 2.69°$ (A.1, M_c)

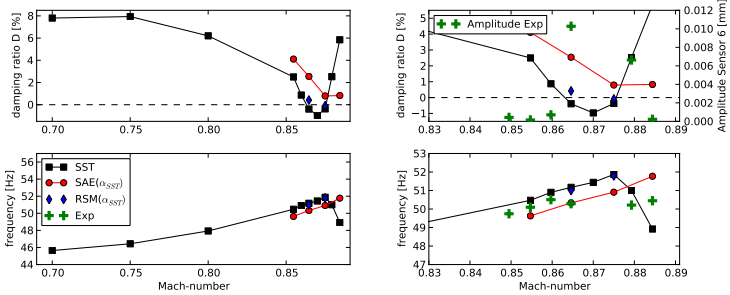

Figure A.4.: Flutter results for SST, SAE and RSM turbulence model, 1 dynamic DOF (A.1, $M_a - M_g$)

A.4. Mode Shapes on Aerodynamic Surface

Modes 1-6 used for degree-of-freedom convergence in Section 9.1.1.

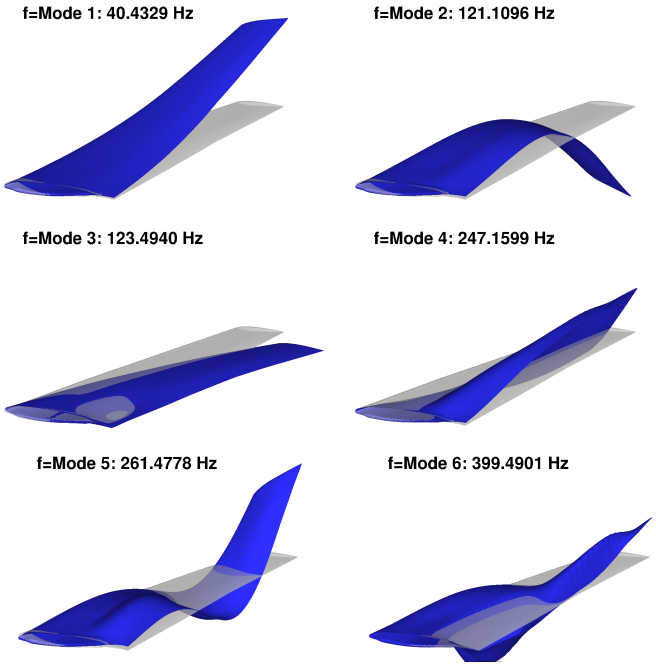

Figure A.5.: CFD surface mesh deformed by structural eigenmodes

A.5. 2-DOF LCO Amplitudes of Sensor 7

Additional time vs. amplitude plots for Section 9.2.1.

(a) $Ma = 0.8646$, $q_\infty = 20.7kPa$

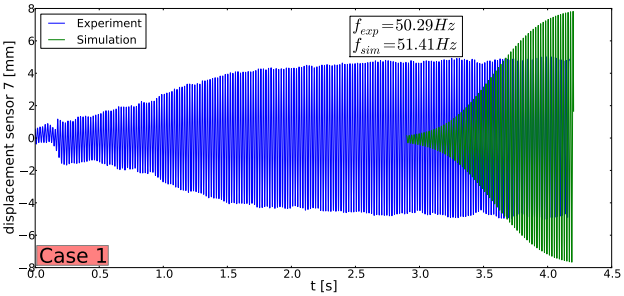

(b) $Ma = 0.8793$, $q_\infty = 20.9kPa$

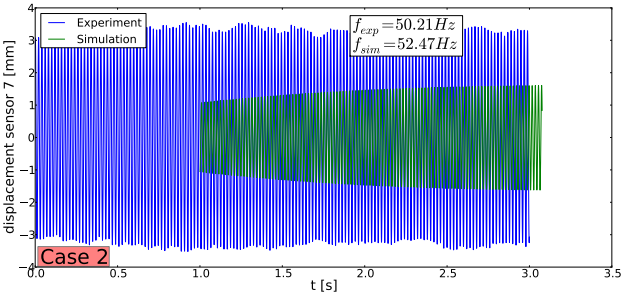

Figure A.6.: Cases 1+2: Sensor 7 amplitudes in z-direction versus time of experiment and simulation (2 DOF) for two different Mach numbers

(a) Case 3: $q_\infty = 17.7kPa$

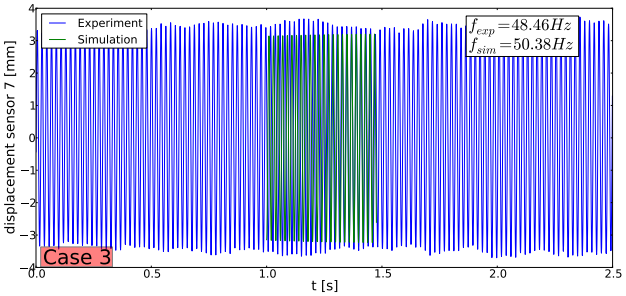

(b) Case 4: $q_\infty = 18.0kPa$

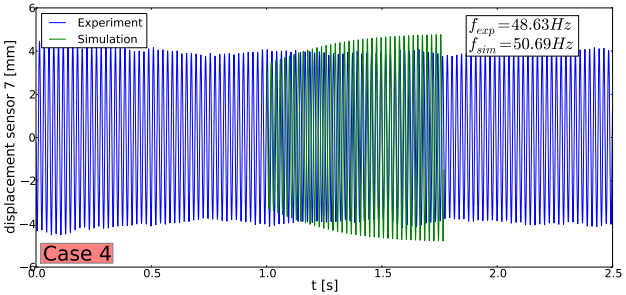

Figure A.7.: Cases 3+4: Sensor 7 amplitudes in z-direction versus time of experiment and simulation (2 DOF) for two different dynamic pressures, $Ma = 0.8646$

A.6. Unsteady Aerodynamics and Work-Per-Cycle Supplement

LCO case 3+4 plots for Section 9.2.2: Validation of same LCO mechanism as case 1+2 via work-per-cycle analysis.

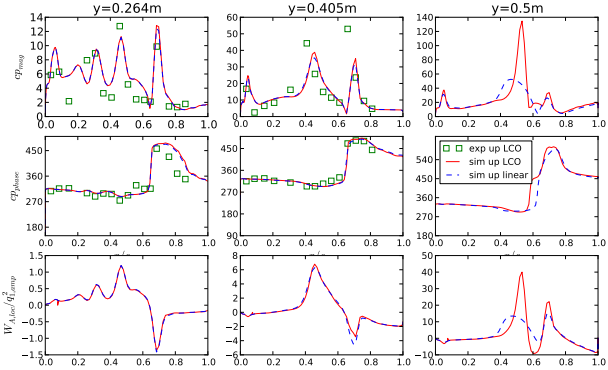

Figure A.8.: Unsteady pressures and work per cycle, local: Ma = 0.8646, $q_\infty = 17.7kPa$ (LCO case 3, A.1, Q_d)

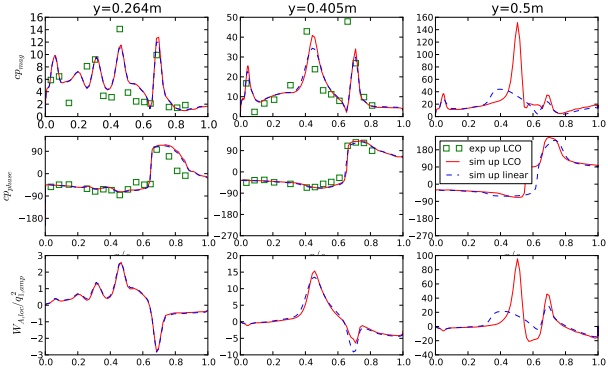

Figure A.9.: Unsteady pressures and work per cycle, local: Ma = 0.8646, $q_\infty = 18.0kPa$ (LCO case 4, A.1, Q_e)

A.7. CFD Parameter for Reference Case

Below some CFD parameter settings are listed for the reference case of Chapter 10. But the same parameters have also been used for the other chapters. The turbulence model is the Menter SST model.

- Inviscid flux discretization: Central scheme, 2nd order
- Central dissipation scheme: Scalar
- Convective meanflow flux: Average of flux
- Convective turbuence flux: Roe
- Dissipation coefficients (2nd/4th order): $0.5/\frac{1}{64}$
- Reconstruction of gradients: Green-Gauss
- Turbulent Prandtl number: 0.9
- Turbulent intensity inflow: 0.001
- SST limitation: vorticity (according to Menter (1994))

A.8. Author Contributions to Publications

In this section the publications by the author (in the following the 'writer') of this dissertation are listed and his contribution to each publication is set into context to the contributions of the other authors.

- Stickan (2009): Stickan, B. (2009). Implementation and extension of a mesh deformation module for the parallel flowsimulator software environment

  Barnewitz and Stickan (2013) Barnewitz, H. and Stickan, B. (2013): Improved mesh deformation

  The first paper is the diploma thesis of the writer. The first author of the second paper was the supervisor of this thesis. The second paper summarizes mainly the method for CFD mesh deformation from the writer's diploma thesis. Subsequently, the first author describes the application of the method to

shape optimization. The basis of the deformation method has already been introduced by Heinrich et al. (2008). Hence, the second paper is named 'Improved mesh deformation'.

- Stickan et al. (2013): B., Bleecke, H., and Schulze, S. (2013). Nastran based static cfd-csm coupling in FlowSimulator

  Bleecke and Stickan (2013): Bleecke, H. and Stickan, B. (2013). Industrial comflite applications.

  Both publications are part of the 'Comflite' (Computational Flight Testing) project book. The first publication describes the static CFD-CSM coupling/interaction methods developed by the writer. The co-authors of this publication have contributed with their large experience in the field of CFD-CSM coupling. In the second publication these methods are applied to industrial examples. This task was performed by both authors.

- Brüderlin et al. (2016): Brüderlin, M., Stickan, B., Schulze, B., and Behr, M. (2016). Numerical aero-structural dynamic simulations of the asdmad wing

  This paper summarizes the diploma thesis by the first author, which deals with the static and dynamic simulations of a wind-tunnel model. The thesis was supervised by the writer and the other co-authors. The applied methods are partly equal to and partly based on the methods described in this document.

- Helm et al. (2015): Helm, S., Haupt, M., B.Stickan, and Bleecke, H. (2015). Advancements of cfd-csm coupling by means of multibody simulation

  For this paper the static CFD-CSM methods described in this document are upgraded for the usage with the multi-body software ADAMS. The extension work for ADAMS was equally partitioned between the first author and the writer. The first author applied the method to a very complex industrial test case. The other authors have supervised the work.

- Stickan et al. (2010):Stickan, B., Dillinger, J., and Schewe, G. (2010). Coupled CFD-CSM simulations of aerostabil wind-tunnel experiments, considering structural shell modelling

Stickan et al. (2014) Stickan, B., Dillinger, J., and Schewe, G. (2014). Computational aeroelastic investigation of a transonic limit-cycle-oscillation experiment at a transport aircraft wing model

These are the reviewed papers of the AEROSTABIL investigations in which the writer uses the developed aeroelastic tools to analyse the experiment by high-fidelity simulations. The second author of both papers contributed with the essential structural modelling of the AEROSTABIL windtunnel model while the third author chipped-in his knowledge of the AEROSTABIL experiments.

Bibliography

Abbott, I. and Von Doenhoff, A. (1959). *Theory of Wing Sections: Including a Summary of Airfoil Data*. Dover Books on physics, engineering. Dover.

Albano, E. and Rodden, W. P. (1969). A doublet-lattice method for calculating lift distributions on oscillating surfaces in subsonic flows. *AIAA Journal*, 7:279–285.

Allen, C. and Rendall, T. (2008). Efficient mesh motion using radial basis functions with data reduction algorithms. In *AIAA Paper 2008-305*. Department of Aerospace Engineering, University of Bristol, Bristol, Great Britain.

Baker, M. L. (1997). Cfd based corrections for linear aerodynamic methods. In *Workshop, Numerical unsteady aerodynamic and aeroelastic simulation; Aalborg; Denmark*.

Banavara, N. and Newsom, J. (2010). Aeroservoelastic analysis of a typical business jet configuration involving nonlinear actuators. AIAA Conference Paper 2010-8114, AIAA. Presented at the AIAA Atmospheric Flight Mechanics Conference, Toronto, Ontario, Aug. 2-5, 2010.

Barnewitz, H. and Stickan, B. (2013). Improved mesh deformation. In Eisfeld, B., Barnewitz, H., Fritz, W., and Thiele, F., editors, *Management and Minimisation of Uncertainties and Errors in Numerical Aerodynamics*, volume 122 of *Notes on Numerical Fluid Mechanics and Multidisciplinary Design*, pages 219–243. Springer Berlin Heidelberg.

Bathe, K.-J. and Wilson, E. L. (1976). *Numerical Methods in Finite Element Analysis*. Englewood Cliffs, N. J., Prentice-Hall.

Baxter, B. J. C. (1992). *THE INTERPOLATION THEORY*. PhD thesis, Trinity College, University of Cambridge.

Beckert, A. and Wendland, H. (2001). Multivariate interpolation for fluid-structure-interaction problems using radial basis functions. *Aerospace Science and Technology*, 5:125–134.

Bendiksen, O. (2004). Transonic limit cycle flutter/lco. AIAA Paper 1998-1727, AIAA. Proc. 45th AIAA/ASME/ ASCE/AHS/ASC Structures, Structural Dynamics, and Materials Conference, Palm Springs.

Bendiksen, O. O. (2003). Transonic flutter prediction. In *International Forum on Aeroelasticity and Structural Dynamics (IFASD), Amsterdam.*

Bendiksen, O. O. (2008). Transonic limit cycle flutter of high-aspect-ratio swept wings. *Journal of Aircraft*, 45(5):1522–1533.

Bendiksen, O. O. (2009). *High-Altitude Limit Cycle Flutter of Transonic Wings*, volume 46, pages 123–136. AIAA.

Blazek, J. (2001). Computational fluid dynamics: Principles and applications. pages –.

Bleecke, H. and Stickan, B. (2013). Industrial comflite applications. In Kroll, N., Radespiel, R., Burg, J. W., and Srensen, K., editors, *Computational Flight Testing*, volume 123 of *Notes on Numerical Fluid Mechanics and Multidisciplinary Design*, pages 249–256. Springer Berlin Heidelberg.

Boussinesq, J. V. (1896). Theorie de l' écoulement tourbillonant et tumulteur des liquides dans les lits rectiligues. *Comptes Rendus de l' Acad. des Sciences*, page 1293.

Bradshaw, P., Ferriss, D. H., and Atwell, N. P. (1967). Calculation of boundary-layer development using the turbulent energy equation. *Journal of Fluid Mechanics*, 28:593–616.

Brüderlin, M., Stickan, B., Schulze, B., and Behr, M. (2016). Numerical aero-structural dynamic simulations of the asdmad wing. In Dillmann, A., Heller, G., Krmer, E., Wagner, C., and Breitsamter, C., editors, *New Results in Numerical and Experimental Fluid Mechanics X: Contributions to the 19th STAB/DGLR Symposium Munich, Germany, 2014*. Springer International Publishing.

Buhmann, M. D. (2003). *Radial Basis Functions: Theory and Implementations*. Cambridge University Press.

B.Wang and Zha, G.-C. (2011). Detached-eddy simulation of transonic limit cycle oscillations using high order schemes. *Computers and Fluids*, 52(0):58 – 68.

CentaurSoft (www). *Centaur*. URL: www.centaursoft.com.

Collar, R. (1946). The Expanding Domain of Aeroelasticity. *The Journal of Royal Aeronautical Society*, 50:613–636.

Cunningham, H. J., Batina, J. T., and Bennett, R. M. (1988). Modern wing flutter analysis by computational fluid dynamics methods. *Journal of Aircraft*, 25:962–968.

Dietz, G., Schewe, G., Kiessling, F., and Sinapius, M. (2003). Limit-cycle-oscillation experiments at a transport aircraft wing model. In *International Forum on Aeroelasticity and Structural Dynamics (IFASD), Amsterdam*.

Dietz, G., Schewe, G., and Mai, H. (2004). Experiments on heave/pitch limit-cycle oscillations of a supercritical airfoil close to the transonic dip. *Journal of Fluids and Structures*, 19(1):1 – 16.

Dietz, G., Schewe, G., and Mai, H. (2006). Amplification and amplitude limitation of heave/pitch limit-cycle oscillations close to the transonic dip. *Journal of Fluids and Structures*, 22(4):505–527.

Dwight, R. (2005). An implicit lu-sgs scheme for finite-volume discretizations of the navier-stokes equations on hybrid grids. DLR-FB-2005-05 ISSN 1434-8454, DLR.

Edwards, J. R. and Chandra, S. (1996). Comparison of eddy viscosity-transport turbulence models for three-dimensional, shock-separated flowfields. *AIAA Journal, Vol. 34*, pages 756–763.

Edwards, J. W., Schuster, D. M., Spain, C. V., Keller, D. F., and Moses, R. W. (2001). Mavric flutter model transonic limit cycle oscillation test. Technical report.

Eisfeld, B. (2004). *Implementation of Reynolds Stress Models into the DLR-FLOWer Code*. Institutsbericht, DLR-IB 124-2004/31. DLR Institute of Aerodynamics and Flow Technology, Braunschweig.

Gerhold, T. and Galle, M. (1997). Calculation of complex three-dimensional configurations employing the DLR TAU-code. *AIAA Paper 97-0167*.

Göge, D. (2003). Automatic updating of large aircraft models using experimental data from ground vibration testing. *Aerospace Science and Technology*, 7(1):33 – 45.

Gordnier, R. E. and Melville, R. B. (2001). Numerical simulation of limit-cycle oscillations of a cropped delta wing using the full navier-stokes equations. *International Journal of Computational Fluid Dynamics*, 14(3):211–224.

Govers, Y., Khodaparast, H. H., Link, M., and Mottershead, J. (2015). A comparison of two stochastic model updating methods using the dlr airmod test structure. *Mechanical Systems and Signal Processing*, 52-53:105 – 114.

Hassig, H. J. (1971). An approximate true damping solution of the flutter equation by determinant iteration. *Journal of Aircraft*, 8(11):885–889.

Heinrich, R., Kroll, N., Neumann, J., and Nagel, B. (2008). Fluid-Structure Coupling for Aerodynamic Analysis and Design - A DLR Perspective. *46th AIAA Aerospace Sciences Meeting and Exhibit 2008, Reno*.

Helm, S., Haupt, M., B.Stickan, and Bleecke, H. (2015). Advancements of cfd-csm coupling by means of multibody simulation. In *Deutscher Luft- und Raumfahrtkongress Rostock, 22-24.9.2015*.

Hughes, T. J. (2000). *The finite element method: linear static and dynamic finite element analysis*. Courier Corporation.

Iovnovich, C. M., Raveh, D. E., Michaels, C. D., and Adar, M. M. (2015). Reynolds-averaged navier-stokes study of the transonic limit cycle oscillation phenomenon on the f-16 fighter aircraft.

In *International Forum on Aeroelasticity and Structural Dynamics (IFASD), St. Petersburg*. Flight Sciences Branch - Israel Air Force, Faculty of Aerospace Engineering, Technion - IIT.

Jameson, A. (1983). Solution of the euler equations for two dimensional transonic flow by a multigrid method. *Applied Mathematics and Computation*, pages 327 – 355.

Jameson, A. (1991). Time dependent calculations using multigrid, with applications to unsteady flows past airfoils and wings. In *Proc. 10th Comp. Fluid Dyn. Conf., Honolulu, HI, USA, June 24-26, 1991, AIAA-Paper 91-1596*.

Jones, W. and Launder, B. (1973). The calculation of low-reynolds-number phenomena with a two-equation model of turbulence. *International Journal of Heat and Mass Transfer*, 16(6):1119 – 1130.

Kaiser, C., Thormann, R., Dimitrov, D., and Nitzsche, J. (2015). Time-linearized analysis of motion0induced and gust-induced airloads with the dlr tau code. In *Deutscher Luft- und Raumfahrtkongress*.

Kang, W., zhong Zhang, J., fei Lei, P., and Xu, M. (2014). Computation of unsteady viscous flow around a locally flexible airfoil at low reynolds number. *Journal of Fluids and Structures*, 46:42 – 58.

Keye, S. (2011). Fluid-Structure Coupled Analysis of a Transport Aircraft and Flight-Test Validation. *Journal of Aircraft*, 48(2):381–390.

Klimmek, T. (2009). Parameterization of topology and geometry for the multidisciplinary optimization of wing structures. Proceedings, European Air and Space Conference 2009, Manchester.

Kok, J. (1999). *Resolving the Dependence on Free-stream Values for the K-omega Turbulence Model*. NLR TP: Nationaal Lucht- en Ruimtevaartlaboratorium. National Aerospace Laboratory NLR.

Kroll, N., K, F., and Fassbender, J. (2005). *Megaflow - Numerical Flow Simulation for Aircraft Design: Results of the Second*

Phase of the German Cfd Initiative Megaflow, Presented During Its Closing Symposium at Dlr, Braunschweig, Germany, December 10 and 11, 2002. Notes on numerical fluid mechanics. Springer.

Lanczos, C. (1950). An iteration method for the solution of the eigenvalue problem of linear differential and integral operators. *J. Res. Nat. Bureau Standards*, 45(4):255–282.

Leatham, M., Stokes, S., Shaw, J., Cooper, J., Appa, J., and Blaylock, T. (2000). Automatic mesh generation for rapid-response navier-stokes calculations. In *Conference: Fluids 2000 Conference and Exhibit, June 2000, Denver, CO*.

Lee, E. M. and Batina, J. T. (1993). Calculation of agard wing 445.6 flutter using navier-stokes aerodynamics. Technical report.

Lee, I. and Kim, S.-H. (1995). Aeroelastic analysis of a flexible control surface with structural nonlinearity. *Journal of Aircraft, Vol. 32, No. 4*.

Mai, H. (2012). Untersuchung der druckverteilungen eines schwingenden ringflügels in transsonischer strömung. Technical report.

Mai, H., Neumann, J., and Hennings, H. (2011). Gust response: A validation experiment and preliminary numerical simulations. In *International Forum on Aeroelasticity and Structural Dynamics (IFASD), Paris*.

Meinel, M. and Einarsson, G. (2010). The flowsimulator framework for massively parallel cfd applications. PARA 2010: State of the Art in Scientific and Parallel Computing, Reykjavik.

Menter, F. (1994). Menter, f.: Two-equation eddy-viscosity transport turbulence model for engineering applications. aiaa journal 32(8), 1598-1605. 32.

Menter, F., Kuntz, M., and Langtry, R. (2003). Ten years of industrial experience with the sst turbulence model. Technical report, Turbulence, Heat and Mass Transfer 4.

Menter, F. R. (1993). Zonal two-equation k-omega turbulence models for aerodynamic flows. *AIAA Journal*, page 2906.

Michler, A. (2013). *Robust and Efficient Methods for Aircraft Trim Simulations*. German Aerospace Center - Center of Computer Applications in Aerospace Science and Engineering.

MSC-Nastran (www). *MSC-Nastran*. URL: www.mscsoftware.com.

MSC-Nastran-Nonlinear (2013). *Implicit Nonlinear (SOL 400/600) Users Guide*. URL: www.mscsoftware.com.

Neumann, J. and Mai, H. (2013). Gust response: Simulation of an aeroelastic experiment by a fluid-structure interaction method. *Journal of Fluids and Structures*, 38(0):290 – 302.

Ohtake, Y., Belyaev, A., and Seidel, H. (2003). Multi-scale and adaptive cs-rbfs for shape reconstruction from cloud of points.

Palacios, R., Climent, H., Karlsson, A., and Winzell, B. (2001). Assessment of strategies for correcting linear unsteady aerodynamics using cfd or experimental results.

Peng, C. and Han, J. (2011). Numerical investigation of the effects of structural geometric and matieral nonlinearities on limit cycle oscillation of a cropped delta wing. *Journal of Fluids and Structures, Vol 27*, pages 611–622.

Poirel, D., Mtivier, V., and Dumas, G. (2011). Computational aeroelastic simulations of self-sustained pitch oscillations of a naca0012 at transitional reynolds numbers. *Journal of Fluids and Structures*, 27(8):1262 – 1277.

Prananta, B. B., Kok, J. C., Spekreijse, S. P., Hounjet, M. H. L., , and Meijer, J. J. (2003). Simulation of limit cycle oscillation of fighter aircraft at moderate angle of attack. Tech. Rep. NRL-TP-2003-526, National Aerospace Laboratory NRL.

Raveh, D. and Dowell, E. (2011). Frequency lock-in phenomenon for oscillating airfoils in buffeting flows. *Journal of Fluids and Structures*, 27(1):89 – 104.

Ritter, M., Neumann, J., and Krüger, W. R. (2015). Nonlinear static and unsteady aeroelastic simulations of the hirenasd wind tunnel model. *AIAA-Journal (In review process)*.

Rotta, J. (1972). *Turbulente Strömungen: Eine Einführung in die Theorie und ihre Anwendung*. Leitfäden der angewandten Mathematik und Mechanik - Teubner Studienbücher. Vieweg+Teubner Verlag.

Schewe, G. (2013). Flow-induced vibrations and the landau equation. *Journal of Fluids and Structures*, 43(0):256 – 270.

Schewe, G., Mai, H., and Dietz, G. (2003). Nonlinear effects in transonic flutter with emphasis on manifestations of limit cycle oscillations. *Journal of Fluids and Structures*, 18(1):3 – 22.

Silva, W. and Raveh, D. E. (2001). Development of unsteady aerodynamic state-space models from cfd-based pulse responses. *AIAA/ASME/ASCE/AHS/ASC Structures, Structural Dynamics and Materials Conference and Exhibit*, 42:51–117.

Spalart, P. and Allmaras, S. R. (1992). A one-equation turbulence model for aerodynamic flows. AIAA Paper 92-0439.

Stanford, B. and Beran, P. (2013). Direct flutter and limit cycle computations of highly flexible wings for efficient analysis and optimization. *Journal of Fluids and Structures*, 36(0):111 – 123.

Stickan, B. (2009). Implementation and extension of a mesh deformation module for the parallel flowsimulator software environment. Diploma Thesis at Airbus Deutschland GmbH, Bremen and Chair for Computational Analysis of Technical Systems, RWTH Aachen.

Stickan, B., Bleecke, H., and Schulze, S. (2013). Nastran based static cfd-csm coupling in flowsimulator. In Kroll, N., Radespiel, R., Burg, J. W., and Srensen, K., editors, *Computational Flight Testing*, volume 123 of *Notes on Numerical Fluid Mechanics and Multidisciplinary Design*, pages 223–234. Springer Berlin Heidelberg.

Stickan, B., Dillinger, J., and Schewe, G. (2010). Coupled cfd-csm simulations of aerostabil windtunnel experiments, considering structural shell modelling. In Dillmann, A., Heller, G.,

Kreplin, H.-P., Nitsche, W., and Peltzer, I., editors, *STAB Symposium 2010, Berlin, In: New Results in Numerical and Experimental Fluid Mechanics VIII (2013)*, volume 121 of *Notes on Numerical Fluid Mechanics and Multidisciplinary Design*, pages 367–375. Springer Berlin Heidelberg.

Stickan, B., Dillinger, J., and Schewe, G. (2014). Computational aeroelastic investigation of a transonic limit-cycle-oscillation experiment at a transport aircraft wing model. *Journal of Fluids and Structures*, 49(0):223 – 241.

Tang, D. and Dowell, E. (2004). Effects of geometric structural nonlinearity on flutter and limit cycle oscillations of high-aspect-ratio wings. *Journal of Fluids and Structures, Vol. 19*, pages 291–306.

Theodorsen, T. (1935). *General Theory of Aerodynamic Instability and the Mechanism of Flutter*. National Advisory Committee for Aeronautics: Report number 496. National Advisory Committee for Aeronautics.

Thormann, R. and Widhalm, M. (2013). Linear-frequency-domain predictions of dynamic-response data for viscous transonic flows. *AIAA-Journal*.

Tijdeman, H. (1977). *Investigations of the transonic flow around oscillating airfoils*. PhD thesis, TU Delft.

Voss, R. (1998). Wall correction methods for dynamic tests. *AGARD-AG-336: Wind Tunnel Wall Corrections, 1998*.

Voss, R. and Thormann, R. (2012). Flutter computations for a generic reference aircraft adopting cfd and reduced order models. In *53rd AIAA Structures, Structural Dynamics, and Materials Conference, Honolulu*.

Walker, W. P. and Patil, M. J. (2010). Unsteady aerodynamics of deformable thin airfoils. In *48th AIAA Aerospace Sciences Meeting, Orlando, Florida*.

Wang, G., Mian, H. H., Ye, Z.-Y., and Lee, J.-D. (2015). Improved Point Selection Method for Hybrid-Unstructured Mesh Deformation Using Radial Basis Functions. *AIAA Journal*, 53(4):1016–1025.

Weaver, W., Timoshenko, S. P., and Young, D. H. (1990). *Vibration problems in engineering*, volume 5. Wiley.

Weissenburger, J. T. and Zimmerman, N. H. (1964). Prediction of flutter onset speed based on flight testing at subcritical speeds. *Journal of Aircraft*, 1:190–202.

Wendland, H. (2002). Fast evaluation of radial basis functions: Methods based on partition of unity. In *Approximation Theory X: Wavelets, Splines, and Applications*, pages 473–483. Vanderbilt University Press.

Wilcox, D. C. (1988). Reassessment of the scale-determining equation for advanced turbulence models. *Aiaa Journal*, 26:1299–1310.

Wilcox, D. C. (1993). *Turbulence modelling for CFD*. DCW Industries, La Cañada.